UCLA

UCLA Electronic Theses and Dissertations

Title

Elastic Waves from Localized Sources with Applications to Nondestructive Evaluation (NDE) of Composite Aerospace Structures

Permalink

https://escholarship.org/uc/item/7006w1s5

Author

Araque, Leonardo

Publication Date

2022

Peer reviewed|Thesis/dissertation

UNIVERSITY OF CALIFORNIA

Los Angeles

Elastic Waves from Localized Sources with Applications to Nondestructive Evaluation

(NDE) of Composite Aerospace Structures

A dissertation submitted in partial satisfaction

of the requirements for the degree

Doctor of Philosophy in Mechanical Engineering

by

Leonardo Araque

2022

ABSTRACT OF THE DISSERTATION

Elastic Waves from Localized Sources with Applications to Nondestructive Evaluation
(NDE) of Composite Aerospace Structures

by

Leonardo Araque

Doctor of Philosophy in Mechanical Engineering

University of California, Los Angeles, 2022

Professor Ajit K. Mal, Chair

In the aerospace industry, the non-destructive evaluation (NDE) of reusable composite structural components in launch vehicles requires the development and implementation of efficient and reliable techniques. Most conventional damage detection methods do not meet these requirements. Recently develop methods using guided ultrasonic waves have the potential to improve the efficiency and reliability of damage detection in aerospace structures. However, they rely on previously collected baseline data that can be different in similar parts in composite structures due to their manufacturing tolerances. To overcome this difficulty, databases from analytical and numerical models may be employed to be correlated with data collected during the NDE of the structures. Nonetheless, the lack of knowledge of the exact material properties – together with manufacturing tolerances – could lead to erroneous conclusions. Evaluation of these uncertainties can be difficult and occasionally infeasible. Rapid and reliable guided ultrasonic wave-based techniques, which include uncertainty in models and material parameters and can localize and characterize flaws in large composite structures, could gain acceptance for the NDE of reusable structures.

In this work, the first objective is to study guided waves formed by the initiation of microcracks in composites, aiming to improve the current passive NDE techniques. Based on an approach developed by seismologists to study earthquake sources, an efficient model

has been developed based on a new form of the Green's function to identify the ultrasonic waves produced during the crack formation. The second objective in this work is to develop a methodology to implement the ultrasonic guided wave based technique as one of the qualifications criteria in composite manufacturing. A baseline-free technique to localize delamination in fiber-reinforced composites is proposed. The technique compares data from waves propagating in the healthy regions of the structure against data from waves crossing defective areas. Therefore, the percentage of the damaged region in the inspection area needs to be small. A damage index approach based on the cross-correlation and energy carried by the signals is used for path identification, with imaging techniques to visualize the damage. The baseline-free guided ultrasonic wave-based technique has been used to identify an artificial delamination in a quasi-isotropic fiber-reinforced composite plate. The technique has shown acceptable results when wave reflectors are not present in the vicinity of the delamination. A technique based on guided ultrasonic waves, coupled with an uncertainty analysis, is developed to quantify the deviations from the assumed nominal values of the material constants of quasi-isotropic fiber-reinforced composites. It is shown using a fuzzy arithmetical assessment that the measured group velocities vary depending on the location within the laminate, opening the possibility of questioning if the assumed nominal values of the material properties could accurately represent the entire material system in any region. Furthermore, after the identified material parameters are defuzzyfied, a new set of nominal values for the material properties is determined.

The dissertation of Leonardo Araque is approved.

Nasr M. Ghoniem

Lihua Jin

Jiann-Wen Ju

Vinay Kumar Goyal

Christoph Schaal

Ajit K. Mal, Committee Chair

University of California, Los Angeles

2022

To my wife and my daughter.

Table of Contents

LIST OF FIGURES

List of Tables

Acknowledgements

This work would have not been possible without the contributions of many people to whom I am extremely grateful.

First and foremost, I am extremely grateful to my advisor, Professor Mal, for his invaluable advice, continuous support, and kindness. His immense knowledge and plentiful experience have encouraged me throughout my academic research and daily life. It has been a privilege to study guided waves with one of the leading experts in the field. I will never forget that Professor Mal believed in me and facilitated the pathway to an amazing, beautiful and thriving experience at UCLA.

I would like to thank the members of my committee, Professors Ghoniem, Ju, Jin, Goyal, and Schaal, for reading and commenting on my dissertation. I am grateful for Professor Schaal's mentorship; working with him was an exceptional experience. I do not have enough words to acknowledge Professor Goyal's influence on me. I have not only grown in knowledge, but also as a person. Professor Goyal has become a role model in many aspects of my life as an engineer and an individual.

Through this process, I have been fortunate to have the support of my dear friends Steffen Tai and Lifu Wang. Their contributions were crucial to the completion of this work. I do not have enough ways to thank them. I would also like to thank to Dr. Jacob Rome, Dr. Dulip Samaratunga, Christopher Sagrillo, and the Aerospace Corporation for their continuous support.

I am forever in debt to my family. My daughter, Paula, was always there when I needed her to cheer me up or to review my writing. Lastly, but most importantly, my wife, Sandra, stood by me through the entire process; her care and love kept me going. This accomplishment is as much hers as it is mine.

Curriculum Vitae

1996 – 2002	B.S. in Mechanical Engineering, Universidad Nacional de Colombia, Bogota, Colombia.
2003 – 2004	Project Engineer, Serviparamo, Colombia.
2004 – 2006	Manufacturing Engineer, Procables, Colombia.
2007 – 2008	Project Engineer 3, H.L. Engineers, Colombia.
2008 – 2014	General Manager, Diamond Promotions, Los Angeles, California
2015 – 2016	M.S. in Mechanical Engineering, University of California, Los Angeles (UCLA).
2016 – Present	Ph.D. student in Mechanical Engineering, University of California, Los Angeles (UCLA).

Publications

[1] Tai S., Wang L., Araque L., Mal A., and Schaal C., "Effects of homogenization and quasi-isotropy assumptions on guided wave-based nondestructive testing methods," International Workshop on Structural Health Monitoring , (2019) .

[2] Wang L., Gao F., Zhang Y., Araque L., Patel B., Tai S., and Mal A., "An improved damage index for non-destructive evaluation of a disbond in honeycomb sandwich structure using guided waves," Journal of Nondestructive Evaluation, Diagnostics and Prognostics of Engineering Systems **3**, 1-14 (2020) .

[3] Araque L., Wang L., Mal A., and Schaal C., "Uncertainty characterization of guided ultrasonic wave properties in composite materials," SPIE Smart Structures/NDE conference **21**, (2020) .

[4] Araque L., Wang L., Samaratunga D., Sagrillo C., Rome J., and Mal A., "Guided ultrasonic wave-based technique for assessment of composite structures with prior damage," AIAA SciTech Forum and Exposition (2021) .

[5] Araque L., Wang L., Mal A., and Schaal C., "Inverse fuzzy arithmetic for material characterization of composites using guided ultrasonic waves," SPIE Smart Structures/NDE conference **26**, (2021) .

[6] Araque L., Wang L., Mal A., and Schaal C., "Advanced fuzzy arithmetic for material characterization of composites using guided ultrasonic waves," Mechanical Systems and Signal Processing **171**, 108856 (2022) .

CHAPTER 1

Introduction

1.1 Motivation

Structures across marine, wind energy, and aerospace industries are commonly manufactured from composite materials due to their associated advantages of reduced weight and fuel consumption, as well as high strength and corrosion resistance. A composite material is typically comprised of strong, stiff fibers in a tough resin matrix. These commonly include carbon fiber reinforced polymers (CFRP), glass fiber reinforced polymers (GRFP), honeycomb cores, and carbon laminates. Composite defects may form during the manufacturing process and include, but are not limited to: bonding defects, delamination, fiber defects, fiber misalignment, foreign bodies, ply cracking, and porosity or voids in the material. In addition to manufacturing defects, in-service composite material defects include: bond failure, fiber breakage, cracking, delamination, failure between the fiber and matrix interface, and moisture ingress. Non-destructive testing (NDT) is used for testing both manufacturing and in-service defects. In the United States, aerospace composites are subjected to ASTM NDT standards E2533, E2662, E2580, E2581 and E2582. These standards recommend the following tests for qualification of fiber- and fabric-reinforced polymatric matrix composites: Acoustic Emission (AE), Computed Tomography (CT), Leak Testing (LT),Radiography Testing (RT), Computed Radiography (CR), Digital Radiography (DR), Radioscopy (RTR), Sheareography, Strain Measurement, Thermography, Ultrasonic Testing (UT) and Visual Testing (VT). However, ultrasonic guided waves (UGW) do not form part of the listed NDE methods. As of today, ASTM only endorses the application of UGW for NDE of steel pipes with the standards E2275-16 and E2929-18. Although NDE with UGW has the

potential to benefit the inspection of large composite structures with subsurface damage, using less and more practical instrumentation compared to the recommended NDE techniques [78, 12, 70, 75], UGW needs to overcome its drawbacks. One of the main problems with the acceptance of UGW for the qualification of aerospace composites is that most of the current approaches used reference data to perform structural assessments [77, 61, 66]. Therefore, the development of a method, which can discern defective zones from healthy regions, could lead to the implementation of guided-wave-based techniques as part of the acceptance process for composite structures in the ongoing reusable launch system development program.

1.2 Outline

The objective of this thesis is to develop a guided wave-based NDE concept to identify AE features of waves originated by the formation of microcracks in composite structures, which can be used to localize and identify the source of the damage. To complement the passive NDE method, a damage detection algorithm based on transmitted waves is used to differentiate between healthy and defective paths in a sensing network created by the excitation of ultrasonic waves (active NDE method). In addition, a NDE technique for material characterization of composites without water immersion is proposed. The technique is based on the uncertainty of the material properties.

In order to present to the readers the contributions from other research in the subjects treated in this thesis, an extensive literature review has been conducted, and it can be found as part of the introductions of Chapters 3 to 5.

This thesis starts with an examination of the basic concepts and equations in elastic wave propagation oriented to the study of wave scattering in anisotropic plates in Chapter 2. Chapter 3 proposes an analytical form of the Green's function for multilayered plates to make a current passive NDE technique more efficient. The new form of the function requires only the modal functions of the media for its calculation, showing the potential to solve boundary value problems of guided waves efficiently. First, the new Green's function

is derived through a Representation Theorem of elastodynamics. The function is then used to calculate the plate response to surface load in single-layered and multilayered plates. The results are compared to those obtained from a standard method. Using an AE model based on the Green's function of the media in absence of discontinuities, the waveforms from microcrack formations are studied. The results of the study identify features in the waveforms, which are characteristic of each crack-type.

Considering epistemic uncertainty in the material properties, Chapter 4 presents a NDE technique for material characterization based on advanced fuzzy arithmetic analysis. First, the Transformation Method (forward analysis) is applied to investigate the influence of the material properties in the calculation of the group velocities in an anisotropic media. Using experimental data, an inverse procedure is then carried out to identify the uncertainty in the material properties. The investigation concludes with the definition of new nominal values of the material properties in a quasi-isotropic laminate, thus proposing a new method for material characterization. A new active damage localization NDE technique is proposed to detect delaminations in large composite structures with prior damage in Chapter 5. Two damage indices are defined based on the comparison of signal features. Signals from waves traveling in parallel paths in an anisotropic medium are collected in groups to compare their features. The standard deviation of the damage indices on each group is then compared to other groups to set a criteria to decide on the presence of damage in the structure. To localize the damage, interpolation functions of the damage indices provide an approximate location of the defect. To study the effect of the configuration of the sensing network in the approximation, a topological analysis is performed. The results of the applied technique show a fairly decent prediction of the location of the delamination.

The thesis concludes with a review of the main findings in this research including the future challenges that the developed techniques may encounter in their application to the NDE of composite aerospace structures.

CHAPTER 2

Fundamentals

In this chapter, a brief description of the fundamentals of guided waves (Lamb waves) to contextualize the study of the waves generated by internal sources in plates is presented. A more detailed discussion can be found on [40, 1, 52, 84]. In Section. 2.1, the basic equations of the propagation of mechanical waves in unbounded media are derived with the objective of providing the basics for the derivation of the dispersion equations and mode shapes of guided waves for a single-layered medium in Section. 2.2, and multilayered plates in Section. 2.3. Furthermore, the derivation of the Green's function for multilayered media using the Residue Theorem is provided in Section. 2.3 for multilayered plates.

2.1 Basic Equations in Elastic Wave Propagation

Assuming linearity, the equation of motion in elastodynamics is of the form

$$\sigma_{ij,\ j} + b_i = \rho\ u_{i,tt} \tag{2.1}$$

where the summation rule in index notation does not apply to the repeated index t. σ_{ij} is the Cauchy stress tensor, b_i is a body force per unit volume, and u_i is the displacement.

In the absence of thermal or other non-mechanical effects, the linear constitutive equations for an elastic solid may be written as

$$\sigma_{ij} = c_{ijkl}\ \epsilon_{kl} = c_{ijkl}\ u_{k,l} \tag{2.2}$$

where c_{ijkl} is the elastic tensor with symmetry properties

$$c_{ijkl} = c_{jikl} = c_{ijlk} = c_{klij} \tag{2.3}$$

4

The strain-displacement relations are

$$\epsilon_{ij} = \frac{1}{2} \left(u_{i,j} + u_{j,i} \right) \tag{2.4}$$

Substitution of Equations (2.2) and (2.4) into Equation (2.1) leads to the Navier's equation

$$c_{ijkl} \, u_{k,lj} + \rho \, b_i = \rho \, u_{i,tt} \tag{2.5}$$

The domain of the equations can be either the reference configuration or the deformed configuration. Therefore, the boundary conditions on the surface S to solve for the displacements can be applied to any of the configurations. In the general case the boundary conditions can be a mixed of natural boundary conditions ($\sigma_{ij} \, n_j = t_i$) and essential boundary conditions u_i.

The law of conservation of mechanical energy is of the form

$$\frac{d}{dt} (U + K) = \int_S \mathbf{t}.\dot{\mathbf{u}} \, dS + \int_V \rho \, \mathbf{b}.\dot{\mathbf{u}} \, dV \tag{2.6}$$

The left-hand side of Equation (2.6) represents the rate of the increase of the total (stored or potential U plus kinetic K) energy of the material within the control volume V, and the right-hand side represents the rate of work done by the applied body and traction forces.

In elastodynamics the rate of transfer of energy, or the energy flux, across a given surface S of a material particle with velocity $\dot{u}_i$ may be expressed as

$$dE_R = -\sigma_{ij} n_j \dot{u}_i dS \tag{2.7}$$

where dE_R is the rate of outflow of energy across the surface element dS with outward unit normal $\mathbf{n}$

In the special case where the solid is isotropic and homogeneous, Eq. (2.5) in absence of body forces can be decoupled in two wave equations by applying the Stokes-Helmholtz decomposition $\mathbf{u} = \mathbf{u_1} + \mathbf{u_2} = \nabla\mathbf{\Phi} + \nabla \times \mathbf{\Psi}$ as

$$\left(\nabla^2 - \frac{1}{c_1^2} \frac{\partial^2}{\partial t^2} \right) \Phi = 0, \qquad \left(\nabla^2 - \frac{1}{c_2^2} \frac{\partial^2}{\partial t^2} \right) \mathbf{\Psi} = 0 \tag{2.8}$$

where $\boldsymbol{\Phi}$ and $\boldsymbol{\Psi}$ are, respectively, scalar and vector potentials, c_1 and c_2 are wave velocities in terms of the Lame constants defined by

$$c_1 = \sqrt{\frac{\lambda + 2\mu}{\rho}}, \qquad c_2 = \sqrt{\frac{\mu}{\rho}} \tag{2.9}$$

2.2 Waves In-Plane-Strain in an Elastic Layer

2.2.1 Isotropic homogeneous

In Cartesian coordinates, if the geometrical configuration and all the physical quantities are independent of x_3, it can be shown that the in-plane-strain displacement and stress components for an isotropic homogeneous solid may be expressed in terms of two scalar potentials Φ and Ψ as

$$u_1 = \frac{\partial \Phi}{\partial x_1} - \frac{\partial \Psi}{\partial x_2} \qquad u_2 = \frac{\partial \Phi}{\partial x_2} + \frac{\partial \Psi}{\partial x_1} \tag{2.10}$$

$$\sigma_{11} = \left(\lambda \nabla^2 + 2\mu \frac{\partial^2}{\partial x_1^2} \right) \Phi - 2\mu \frac{\partial^2 \Psi}{\partial x_1 \partial x_2} \tag{2.11}$$

$$\sigma_{12} = \mu \left(2\frac{\partial^2 \Phi}{\partial x_1 \partial x_2} + \frac{\partial^2 \Psi}{\partial x_1^2} - \frac{\partial^2 \Psi}{\partial x_2^2} \right) \qquad \sigma_{22} = \left(\lambda \nabla^2 + 2\mu \frac{\partial^2}{\partial x_2^2} \right) \Phi + 2\mu \frac{\partial^2 \Psi}{\partial x_1 \partial x_2} \tag{2.12}$$

where the scalar potential Ψ is a special case of Eq. (2.8) with $\boldsymbol{\Psi} = (0, 0, -\Psi)$

Assuming that an isotropic homogeneous layer occupies the region $-H/2 < y < H/2$, $-\infty < x < \infty$, and its surfaces $y = \pm H/2$ are traction free, in the time harmonic case the potentials may be expressed in the form

$$\Phi(x, x_2) = [A \sinh(\eta_1 x_2) + B \cosh(\eta_1 x_2)] e^{i(kx_1 - \omega t)} \tag{2.13}$$

$$\Psi(x_1, x_2) = [C \sinh(\eta_2 x_2) + D \cosh(\eta_2 x_2)] e^{i(kx_1 - \omega t)} \tag{2.14}$$

where k is the wavenumber in the propagation direction to be solved from the dispersion equation, and $\eta_j = \sqrt{k^2 - \omega/c_j^2}$ is the wavenumber in the x_2 direction with Re $\eta_j \geq 0$

The dispersion equations are given by

$$\frac{\tanh(\eta_2 H)}{\tanh(\eta_1 H)} = \frac{(2k^2 - k_2^2)^2}{4k^2 \eta_1 \eta_2} \tag{2.15}$$

6
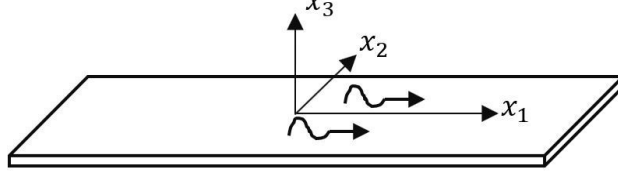
Figure 2.1: Coordinate axes of a transversely isotropic solid

for the antisymmetric case and

$$\frac{\tanh\left(\eta_1 H\right)}{\tanh\left(\eta_2 H\right)} = \frac{\left(2k^2 - k_2^2\right)^2}{4k^2 \eta_1 \eta_2} \tag{2.16}$$

for the symmetric case

2.2.2 Transversely isotropic problem

In a transversely isotropic homogeneous single-layer with thickness H and symmetry about the off-plane axis x_3 (see Fig. 2.1), the dispersion equations are given as follows [6].

$$\left\{\frac{\tanh(kA_1 H/2)}{\tanh(kA_2 H/2)}\right\}^m = \frac{A_1\left[A_2^2 - \frac{C_{11}}{C_{13}}\left(\frac{c^2}{c_{1L}^2} - 1\right)\right]\left[\frac{C_{11}}{C_{33}}\left(\frac{C_{13}}{C_{44}} + 1\right) + A_1^2 + \frac{C_{11}}{C_{44}}\left(\frac{c^2}{c_{1L}^2} - 1\right)\right]}{A_2\left[A_1^2 - \frac{C_{11}}{C_{13}}\left(\frac{c^2}{c_{1L}^2} - 1\right)\right]\left[\frac{C_{11}}{C_{33}}\left(\frac{C_{13}}{C_{44}} + 1\right) + A_2^2 + \frac{C_{11}}{C_{44}}\left(\frac{c^2}{c_{1L}^2} - 1\right)\right]}, \tag{2.17}$$

where applying $m = 1$ and $m = -1$, respectively, gives the symmetric and antisymmetric equations. The expressions for A_q and C_{ij} are given in the Appendix. A.1.1

2.2.3 Unidirectional fiber-reinforced composite

In a unidirectional fiber-reinforced composite plate with thickness H and symmetry axis along the fiber direction (x_1-axis, see Fig. 2.1), the dispersion equation for symmetric wave motion can be written in the form[46, 21],

$$\Delta_1 \cos\left(\zeta_1 H/2\right) \sin\left(\zeta_2 H/2\right) \sin\left(\zeta_3 H/2\right) + \Delta_2 \sin\left(\zeta_1 H/2\right) \cos\left(\zeta_2 H/2\right) \sin\left(\zeta_3 H/2\right)$$
$$+ \Delta_3 \sin\left(\zeta_1 H/2\right) \sin\left(\zeta_2 H/2\right) \cos\left(\zeta_3 H/2\right) = 0 \tag{2.18}$$

and for the antisymmetric wave motion as

7
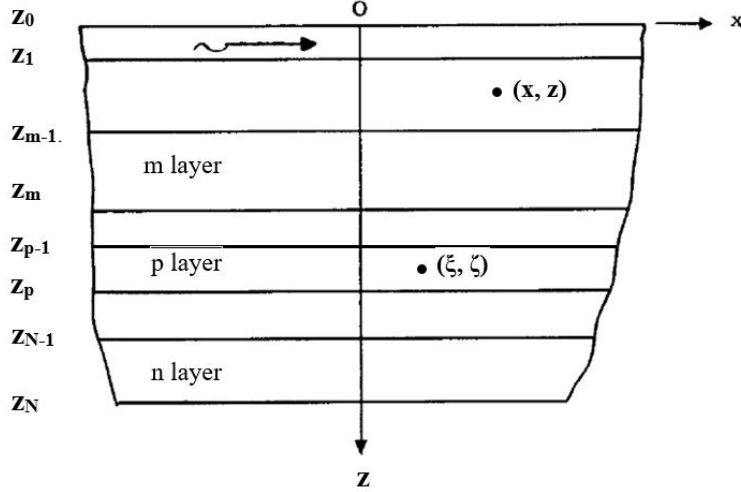
Figure 2.2: Geometry of the layered solid

$$\Delta_1 \sin\left(\zeta_1 H/2\right) \cos\left(\zeta_2 H/2\right) \cos\left(\zeta_3 H/2\right) + \Delta_2 \cos\left(\zeta_1 H/2\right) \sin\left(\zeta_2 H/2\right) \cos\left(\zeta_3 H/2\right)$$

$$+ \Delta_3 \cos\left(\zeta_1 H/2\right) \cos\left(\zeta_2 H/2\right) \sin\left(\zeta_3 H/2\right) = 0 \quad (2.19)$$

where the expressions for Δ_i and ζ_j are given in the Appendix. A.1.2.

2.3 Green's Function for a Layered Solid

In this section, a brief description of the procedure to obtain the time-harmonic Green's function for a two-dimensional transversely isotropic layered through the Residual Theorem is presented. This method is based on the work done by [43, 48]. However, a similar approach can be found on [37, 91].

Consider a uniformly multilayered structure with geometry as it is shown in Fig. 2.2. The solid occupies the region $0 < z < H$, $-\infty < x < \infty$, and its surfaces $z = 0, H$ are traction free. The equation of motion of the solid with plane strain reduction is given by,

$$\sigma_{ij,\,j} + b_i = \rho\; u_{i,tt} \quad i, j = 1, 3 \tag{2.20}$$

When the material is transversely isotropic with stress-strain law invariant under an

8

arbitrary rotation about the x_3-axis, the stress-strain law takes the form

$$\begin{Bmatrix} \sigma_{11} \\ \sigma_{33} \\ \sigma_{13} \end{Bmatrix} = \begin{bmatrix} C_{11} & C_{13} & 0 \\ C_{13} & C_{33} & 0 \\ 0 & 0 & C_{44} \end{bmatrix} \begin{Bmatrix} u_{1,1} \\ u_{3,3} \\ u_{1,3} + u_{3,1} \end{Bmatrix} \tag{2.21}$$

For the purpose of this section, let the field variables be assumed to be time harmonic, and be expressed in the forms

$$u_i(\mathbf{x}, t) = U_i(z)e^{i(kx - \omega t)} \tag{2.22}$$

$$\sigma_{ij}(\mathbf{x}, t) = S_{ij}(z)e^{i(kx - \omega t)} \tag{2.23}$$

$$b_i(\mathbf{x}, t) = B_i(z)e^{i(kx - \omega t)} \tag{2.24}$$

Let a time harmonic line force of unit magnitude act at (ξ, ζ) in the multilayered media. Let $G_{ik}(\mathbf{x}, \mathbf{z}, \xi, \zeta)$ denote the x_i component of the displacement produced at (x, z) due to a unit line force at (ξ, ζ) acting in the x_k direction. For fixed (ξ, ζ), $G_{ij}(\mathbf{x}, \mathbf{z}, \xi, \zeta)$ represents waves which propagate in the $+x$ direction if $x > \xi$ and in the $-x$ direction for $x < \xi$.

Following the Global Matrix approach, for the layers where the unit force is not acting, the wave displacement and stress components at the interface are given by [41]

$$\{u_1, \ u_3, \ \sigma_{13}, \ \sigma_{33}\}^{\mathrm{T}} = \int_{-\infty}^{+\infty} \{U(z - z_r), \ V(z - z_r), \ T(z - z_r), \ \Sigma(z - z_r)\}^{\mathrm{T}} e^{ik(x - x_r)} \ dk \tag{2.25}$$

where the time factor $e^{-i\omega t}$ has been omitted for simplicity, and (x_r, z_r) is a reference point.

Representing the displacement-stress vector $\{U, \ V, \ T, \ \Sigma\}^T$ by $\{S(z)\}$, it has been demonstrated that $\{S(z)\}$ in the mth layer may be given by the matrix product,

$$\{S(z)\} = [Q(m)] [E(z, m)] \{C(m)\}, \qquad z_{m-1} < z < z_m \tag{2.26}$$

where $E(z, m)$ is the diagonal matrix

$$\{E(z, m)\} = \mathrm{Diag} \left[e_1^+(z - z_{m-1}), \ e_2^+(z - z_{m-1}), \ e_1^-(z_m - z), \ e_2^-(z_m - z) \right] \tag{2.27}$$

where it has been used the notation $e_\alpha^\pm(z) = e^{\pm\eta_\alpha z}$, $\alpha = 1, 2$, and "+" for $z_r > z$ and "-" for $z_r < z$. η_α are the roots of the Navier's equation, which results from substituting Eq. (2.21)

9

into Eq. (2.20). Note that η_α should be real or complex with $\text{Im}(\eta_\alpha) \geq 0$ to ensure the outgoing wave condition, and the exponential decay of the nonpropagating waves.

The additional matrices in the displacement-stress vector $\{S(z)\}$ are the unknown constant vector

$$\{C(m)\} = \{C_1^+, \ C_2^+, \ C_3^-, \ C_4^-\} \tag{2.28}$$

and the matrix

$$[Q(m)] = \begin{bmatrix} [Q_{11}(m)] & [Q_{12}(m)] \\ [Q_{21}(m)] & [Q_{22}(m)] \end{bmatrix} \tag{2.29}$$

where

$$[Q_{11}(m)] = \begin{bmatrix} 1 & 1 \\ \beta_1 & \beta_2 \end{bmatrix} \qquad [Q_{12}(m)] = \begin{bmatrix} 1 & 1 \\ -\beta_1 & -\beta_2 \end{bmatrix} \tag{2.30}$$

$$[Q_{21}(m)] = \begin{bmatrix} C_{44}(-\eta_1 + ik\beta_1) & C_{44}(-\eta_2 + ik\beta_2) \\ (ikC_{13} - C_{33}\beta_1\eta_1) & (ikC_{13} - C_{33}\beta_2\eta_2) \end{bmatrix} \tag{2.31}$$

$$[Q_{22}(m)] = \begin{bmatrix} -C_{44}(-\eta_1 + ik\beta_1) & -C_{44}(-\eta_2 + ik\beta_2) \\ (ikC_{13} - C_{33}\beta_1\eta_1) & (ikC_{13} - C_{33}\beta_2\eta_2) \end{bmatrix} \tag{2.32}$$

$$\beta_\alpha = \frac{-k^2 C_{11} + \rho\omega^2 + \eta_\alpha^2 C_{44}}{ik\eta_\alpha(C_{13} + C_{44})} \qquad \alpha = 1, 2 \tag{2.33}$$

In order to account for the stress discontinuity in the source layer, across the plane $z = \zeta$, the following term is added to Eq. (2.26) [41, 43]

$$\{S(y)_-^+\} = \left[Q_-^+\right] [E_s(z - \zeta)] \{D_-^+\} \quad m = p \tag{2.34}$$

$$= 0 \qquad\qquad\qquad m \neq p$$

$$\{E_s(y)\} = \text{Diag}\left[e_1^+(|z|), \ e_2^-(|z|)\right] \tag{2.35}$$

$$\{D_-^+\} = \left[D_1^\pm \ \ D_2^\pm\right]^T \tag{2.36}$$

with "+" for $z > \zeta$ and "-" for $z < \zeta$, and where $D_1^\pm$ and $D_2^\pm$ are, respectively, the strength parameters related to stresses $T(z_p)$ and $\Sigma(z_p)$ in the layer $m = p$.

Thus,

$$\{S(z)\} = [Q(m)] [E(z, m)] \{C(m)\} + \{S(y)_-^+\} \tag{2.37}$$

10

Then, the Global Matrix method is used to assemble a system of equations 4Nx4N to solve for the unknown constants. In Section. 3.1 a different approach is used to calculate the Green's function.

CHAPTER 3

Elastodynamic Green's function for layered plates

As indicated in Section 1.1, composite defects found in aerospace structures during manufacturing and in-service include cracking and delamination. Analytical methods to study the structural response to the presence of discontinuities in the media, such as inclusions, cracks, and steps, result in a propagated and scattered field, which is represented in the linearized theory of wave propagation by models in integral form [55, 47]. Since the models require the Green's function of the media in absence of discontinuities to solve for the displacement response, deriving a form that simplifies the function's calculation could reduce significantly the computational time of the theoretical model. Some of the most representative analytical works to obtain the time-harmonic Green's function in layered media for two-dimensional problems include, but are not limited to [80, 48, 37, 42]. In these works, the procedure to determine the Green's function includes integration in the complex-plane, which is computational expensive and susceptible of errors due to the calculations with large numbers. Most recent works on layered media have been focused on becoming more efficient, and accurate [81, 57, 35]; however, their approach still requires integration in the complex-plane.

Based on the integral representation theorems of elastodynamics, [36, 15, 31] [28] proposed an alternative method to obtain the surface or guided wave terms of the Green's function for a two-dimensional multilayered half-space . Later, [44] used the surface terms of the Green's function to compute the approximate transmission and reflection coefficients of Rayleigh waves in a homogeneous half-space. These works provide the basis to the development of the new elastodynamic Green's function for layered plates.

As of today, Acoustic Emission (AE) techniques for structural assessment have not been

focused on the development of methods for the characterization of the source of AE events. Instead, the techniques are based on essential AE signal features, such as arrival time, maximum peak amplitude, signal duration, and energy. The small number of works on source characterization have their roots in seismological models to study dislocations in the elastic media by applying the Representation Theorem. The models substitute the discontinuity in the displacement produced by a seismic dislocation with body force equivalents [9, 45]. Using a different approach, [83] investigated the applicability of the force equivalent model to study infinitesimal dislocations in thick homogeneous plates by assuming a displacement discontinuity function. Later, [21, 7] used the equivalent force model to study microcrack initiation in composite laminates.

In this chapter a new form of the Green's function for multilayered plates is obtained as an extension of Herrera's work [28] to be applied in the source characterization of AE events. The derivation of the function is presented in Section 3.1. To validate the function, the plate response for a homogeneous plate is compared to the results from the Residue Theorem in Section 3.3. Finally, in Section 3.4, the waveform of the displacements produced by the formation of normal and shear microcracks in an aluminum plate are obtained by implementing the new Green's function. In addition, the transmitted field in a guided-wave with thickness change is calculated with a first order approximation.

3.1 Green's Function Derivation Through the Representation Theorem

Consider a uniformly multilayered structure in which the elastic constants are piecewise constant functions of x_2. Assume that the displacements and the stresses are independent of x_3. The displacement vector $\mathbf{u}(\mathbf{x})e^{-i\omega t}$ in each mode satisfies the equation of motion,

$$\sigma_{ij,j}(\mathbf{u}) + \rho\omega^2 u_i = 0 \qquad i,j = 1,2 \qquad (3.1)$$

at all points within the medium, except at the interfaces. Furthermore, $u_i(\mathbf{x})$ and $\sigma_{i2}(\mathbf{u})$ are continuous across each interface, and $\sigma_{i2}(\mathbf{u}) = 0$ on the top and bottom surfaces of the

13
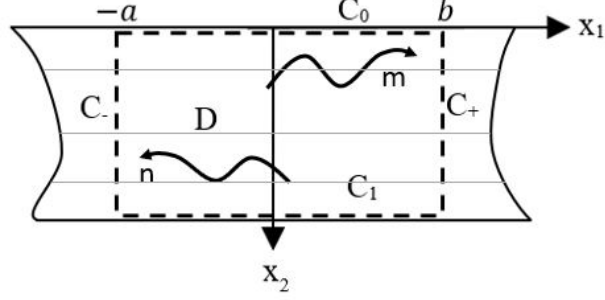
Figure 3.1: Control Region in a Layered Plate with Thickness H

multilayered media. The wave displacements and stresses components can be expressed in the forms,

$$u_i^m(\mathbf{x}) = U_i^m(x_2) e^{ik_m x_1} \qquad \sigma_{ij}^m(\mathbf{x}) = S_{ij}^m(x_2) e^{ik_m x_1} \tag{3.2}$$

where k_m, the wavenumber in the mth mode, is a root of the dispersion equation,

$$F(k, \omega) = 0 \tag{3.3}$$

We shall refer to k_m as an eigenvalue, Eq. (3.3) as the eigenvalue equation, and $u_i^m(\mathbf{x})$ as an eigenfunction for the multilayered media.

Let D denote the area enclosed by the straight lines C_0, C_1, C_-, C_+ (Figure 3.1). Since there are no body forces within D, the following identity can be easily proved.

$$\int_{C_0 + C_\mp + C_1} \left(u_i^m \left(\sigma_{ij}^n \right)^* - (u_i^n)^* \sigma_{ij}^m \right) n_j ds = 0 \tag{3.4}$$

in which n_j is an outward unit normal and (*) indicates a complex conjugate.

Because of the free traction boundary conditions on C_0 as well as C_1, the integrand in Eq. (3.4) vanishes. Noting that $n_j = -\delta_{1j}$ on C_- and $n_j = \delta_{1j}$ on C_+, the above identity becomes

$$\int_0^H \left(U_i^m (S_{i1}^n)^* - (U_i^n)^* S_{i1}^m \right) dx_2 \cdot e^{-i(k_m - k_n)a} = \int_0^H \left(U_i^m (S_{i1}^n)^* - (U_i^n)^* S_{i1}^m \right) dx_2 \cdot e^{i(k_m - k_n)b} \tag{3.5}$$

Since a and b are arbitrary, equation (5) implies that,

$$\int_0^H \left(U_i^m (S_{i1}^n)^* - (U_i^n)^* S_{i1}^m \right) dx_2 = 0, \qquad m \neq n \tag{3.6}$$

14

Thus we may write,

$$\int_0^H \left(U_i^m \left(S_{i1}^n \right)^* - \left(U_i^n \right)^* S_{i1}^m \right) dx_2 = R^m \delta_{mn} \tag{3.7}$$

where

$$R^m = 2i \int_0^H Im \left(U_i^m \left(S_{i1}^m \right)^* \right) dx_2 \tag{3.8}$$

Eq. (3.7) describes the orthogonality of the waves in a multilayered media.

Let a time harmonic line force of unit magnitude act at $x = \xi$ in a multilayered media. Let $G_{ij}(\mathbf{x}, \boldsymbol{\xi})$ denote the x_i component of the displacement produced at x due to a unit line force at ξ acting in the x_j direction. For fixed ξ, $G_{ij}(\mathbf{x}, \boldsymbol{\xi})$ represents waves which propagate in the $+x_1$ direction if $x_1 > \xi_1$ and in the $-x_1$ direction for $x_1 < \xi_1$. Consequently, $G_{ij}(\mathbf{x}, \boldsymbol{\xi})$ may be expressed as,

$$G_{ij}(\mathbf{x}, \boldsymbol{\xi}) = \sum_m A_j(\xi_2) U_i^m(x_2) e^{ik_m(x_1 - \xi_1)}, \qquad x_1 > \xi_1$$
$$G_{ij}(\mathbf{x}, \boldsymbol{\xi}) = \sum_m B_j(\xi_2) \left(U_i^m \right)^*(x_2) e^{-ik_m(x_1 - \xi_1)}, \qquad x_1 < \xi_1 \tag{3.9}$$

where $U_i^m(x_2) e^{ik_m x_1}$ is an eigenfunction of the multilayered media and A_j^m, B_j^m are, as yet, unknown functions of the source depth.

Recall the region D, which is bounded by the surfaces C_0, C_1, C_-, C_+. Let $U_i(\mathbf{x})$ denote a possible displacement field within D and on the bounding surfaces. According to the Representation Theorem of elastodynamics, the solutions inside D can be obtained in terms of the Green's function and the boundary data.

$$u_k(\mathbf{x}) = \int_{C_0 + C_\mp + C_1} \left\{ G_{ik}(\boldsymbol{\xi}, \mathbf{x}) \sigma_{ij}(\mathbf{u}) - u_i(\boldsymbol{\xi}) \tau_{ij}(\mathbf{G}_k) \right\} n_j ds(\xi) \tag{3.10}$$

where

$$\sigma_{ij}(\mathbf{u}) = C_{ijpq} u_{p,q} \qquad \tau_{ij}(\mathbf{G}_k) = C_{ijpq} G_{kp,q} \tag{3.11}$$

and commas indicate differentiation with respect to $\boldsymbol{\xi}$. Note that in the Representation Theorem Eq. (3.10) the location of the virtual force for the Green's function is at the field point $\mathbf{x}$. Since C_0 and $\mathbf{C_1}$ are traction free,

$$\sigma_{ij}(\mathbf{u}) n_j = \tau_{ij}(\mathbf{G}_k) n_j = 0 \text{ on } C_0 \tag{3.12}$$

15

Thus,

$$u_k(\mathbf{x}) = -\int_0^H \{ G_{ik}(\boldsymbol{\xi},\mathbf{x})\,\sigma_{i1}(\mathbf{u}) - u_i(\boldsymbol{\xi})\,\tau_{i1}(\mathbf{G_k}) \}_{\xi_1=-a}\,ds(\xi_2)$$

$$+\int_0^H \{ G_{ik}(\boldsymbol{\xi},\mathbf{x})\,\sigma_{i1}(\mathbf{u}) - u_i(\boldsymbol{\xi})\,\tau_{i1}(\mathbf{G_k}) \}_{\xi_1=b}\,ds(\xi_2) \quad (3.13)$$

Let $u_k(\mathbf{x}) = U_k^n(x_2)\,e^{ik_n x_1}$ be a wave eigenfunction for the multilayered media propagating in the positive x_1-direction. Note that on $x_1 = -a$, $x_1 < \xi_1$, so that

$$G_{ik}(\boldsymbol{\xi},\mathbf{x}) = \sum_m A_k^m(x_2)\,U_i^m(\xi_2)e^{ik_m(\xi_1 - x_1)} \quad (3.14)$$

and on $x_1 = b$, $x_1 > \xi_1$, so that

$$G_{ik}(\boldsymbol{\xi},\mathbf{x}) = \sum_m B_k^m(x_2)\,(U_i^m)^*(\xi_2)e^{-ik_m(\xi_1 - x_1)} \quad (3.15)$$

Substituting from Eqs. (3.14) and (3.1) into Eq. (3.13) we have,

$$U_k(\mathbf{x_2})\,e^{ik_n x_1} = -\sum_m A_k^m(x_2)\,e^{-ik_m x_1 - i(k_m + k_n)a}\int_0^H (U_i^m S_{i1}^n - U_i^n S_{i1}^m)\,d\xi_2$$

$$+\sum_m B_k^m(x_2)\,e^{ik_m x_1 + i(k_n - k_m)b}\int_0^H \left((U_i^m)^* S_{i1}^n - U_i^n (S_{i1}^m)^*\right)\,d\xi_2 \quad (3.16)$$

By applying the orthogonality condition (Eq. (3.7)) to Eq. (3.16), the function B_k^m can be written as

$$B_k^n(x_2) = \frac{U_k^n(x_2)}{R^n} \quad (3.17)$$

By assuming that $u_k(\mathbf{x}) = (U_k^n(x_2))^*\,e^{-ik_n x_1}$, which is a wave eigenfunction propagating in the negative x_1-direction in Eq. (3.13), it can be proved that

$$A_k^n(x_2) = \frac{(U_k^n(x_2))^*}{R^n} \quad (3.18)$$

Using Eqs. (3.17) and (3.18) in Eq. (3.9), the Green's function may be written in the form,

$$G_{ki}(\mathbf{x},\boldsymbol{\xi}) = \sum_m \frac{U_k^m(x_2)\,(U_i^m(\xi_2))^*\,e^{ik_m(x_1 - \xi_1)}}{R^m}; \quad x_1 > \xi_1$$

$$G_{ki(\mathbf{x},\boldsymbol{\xi})} = \sum_m \frac{(U_k^m(x_2))^*\,U_i^m(\xi_2)e^{-ik_m(x_1 - \xi_1)}}{R^m}; \quad x_1 < \xi_1 \quad (3.19)$$

16

and its associated stress as,

$$T_{ki}(\mathbf{x}, \boldsymbol{\xi}) = \sum_m \frac{U_k^m(x_2)\left(S_i^m(\xi_2)\right)^* e^{ik_m(x_1-\xi_1)}}{R^m}; \quad x_1 > \xi_1$$

$$T_{ki(\mathbf{x}, \boldsymbol{\xi})} = \sum_m \frac{\left(U_k^m(x_2)\right)^* S_i^m(\xi_2) e^{-ik_m(x_1-\xi_1)}}{R^m}; \quad x_1 < \xi_1 \tag{3.20}$$

With this form of the Green's function, the inverse Fourier transform with respect to the wavenumber k is not required to obtain the Green's function in the frequency domain. Only the modal functions of the layered media obtained in the wavenumber domain are needed, which can be calculated with a fair approximation through the Singular Value Decomposition (SVD) of the Global Matrix.

3.2 Singular Value Decomposition of the Global Matrix

An approximation of the modal component of the displacements and stresses for guided waves may be obtained from the singular value decomposition (SVD) of the dispersion equation [87]. The inherent error in the numerical solution of the transcendental equation leads to a none singular matrix $\mathbf{G}$ in the Global Matrix, and therefore it may not be possible to get the null space vector of G. The null space vector contains the mode shapes of the displacements and the stresses. In order to circumvent this difficulty, the SVD of the matrix $\mathbf{G}$ has been proposed to obtain an approximation of the wave mode shapes. In order to get a fair approximation of the shapes, the acceptance of the minimum singular value σ_{min} of the SVD of $\mathbf{G}$ depends on the uniqueness of $\mathbf{G}$'s null space γ and a condition number κ. By following these controls, the stability of the modal functions at each frequency can be guaranteed. The steps to obtain the approximate modal functions are described below:

1. Calculation of the matrix $\mathbf{G}$'s SVD, and extraction of the minimum singular value σ_{min}

2. Evaluation of the condition number κ

$$\kappa = \frac{\sigma_{\max}}{\sigma_{\min}} \tag{3.21}$$

   where σ_{max} is the largest value calculated in each iteration. The value of κ tends to infinity as $\mathbf{G}$ gets close to a singular matrix.

3. Evaluation of the uniqueness of the null space γ

$$\gamma = \frac{\sigma_2}{\sigma_{\min}} \tag{3.22}$$

This value should be infinity for all cases since the Null($\mathbf{G}$) should always be one dimension other than the crossing point, which means ideally there is always only one zero singular value for the matrix $\mathbf{G}$.

It should be noticed that as a result of the approximation, its is expected that the boundary conditions are not exactly satisfied. However, it has been demonstrated that this method provides a less expensive computational method to find the mode shapes of the guided waves for layered media with acceptable results.

3.3 Numerical Validation

3.3.1 Single-layered plates

In this section, the new form of the Green's function is evaluated and its results are compared to the results from the Residue Theorem approach. In the first validation case, an aluminum plate with thickness 4 mm is excited by a point force on the top surface, and the plate's response is evaluated in the near field on the loaded surface. Since the model is an isotropic single-layer, the analytical modal functions used in the calculation of the components of the Green's tensor G21 and G22 can be easily found in the literature [1]. The first three modes of the dispersion curves of the layer are shown in Fig. 3.2a. In order to validate the plate response, the spectra of the displacements U_1, U_2 are compared to G21 and G22, respectively. Figs. 3.2b and 3.2c show a perfect match among the spectra. In order to verify the wave's distribution through the thickness, the normalized modal functions have been compared. As an example of the results, the mode shapes of G22 and G21 and compared to the corresponding displacements U2 and U1 for the frequencies 20 kHz, 100 kHz, and 1000 kHz. As depicted in Fig. 3.3, the Green's function components do not differ from the displacements U_1 and U_2.

(a) Dispersion curves

(b) Displacement U_1
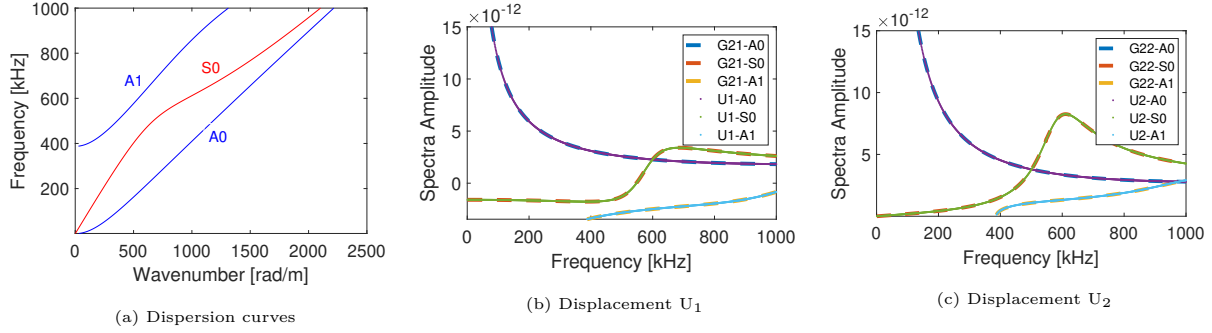
(c) Displacement U_2

Figure 3.2: Dispersion curves and response to a surface normal line load for an aluminum plate with properties: $c_1 = 6.2\,\text{mm}/\mu s$, $c_2 = 3.1\,\text{mm}/\mu s$, and $\rho = 2.7\,\text{g/cm}^3$

(a) Normalized displacement G21(U1)

(b) Normalized displacement G22(U2)
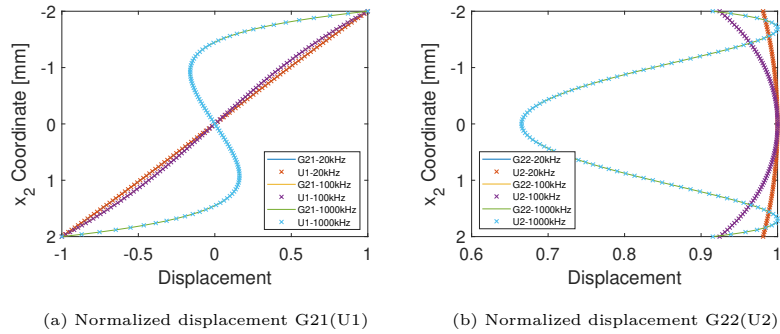
Figure 3.3: Normalized distribution of the displacements in an aluminum plate due to surface normal load for selected frequencies. Plate's properties listed in Fig. 3.2

For the next case study, an isotropic plate (Glass) is subjected to a unit normal load at the top surface with step time dependence H(t), and the vertical displacement G22 is evaluated at a point 96 mm from the source. The calculated displacements show an earlier arrival of the Reighley wave ($1.78\,\mu s$) compared to time reported in [90]. This discrepancy could be attributed to the step-time-dependency of the solution. The time increment used for the calculations in this study guarantee convergence in the solution. The first two symmetric and antisymmetric modes for the component G22 are shown in Fig. 3.4. Although the contribution to the vertical displacement from the A0 mode cannot be recovered by the FFT due the unbalanced loading [83], the result is useful to validate the new form of the Green's function obtained in section 3.1.

(a) Mode S0 G22. Maximum peak 1.17×10^{-12} m

(b) Mode S1 G22

(c) Mode A0 G22

(d) Mode A1 G22
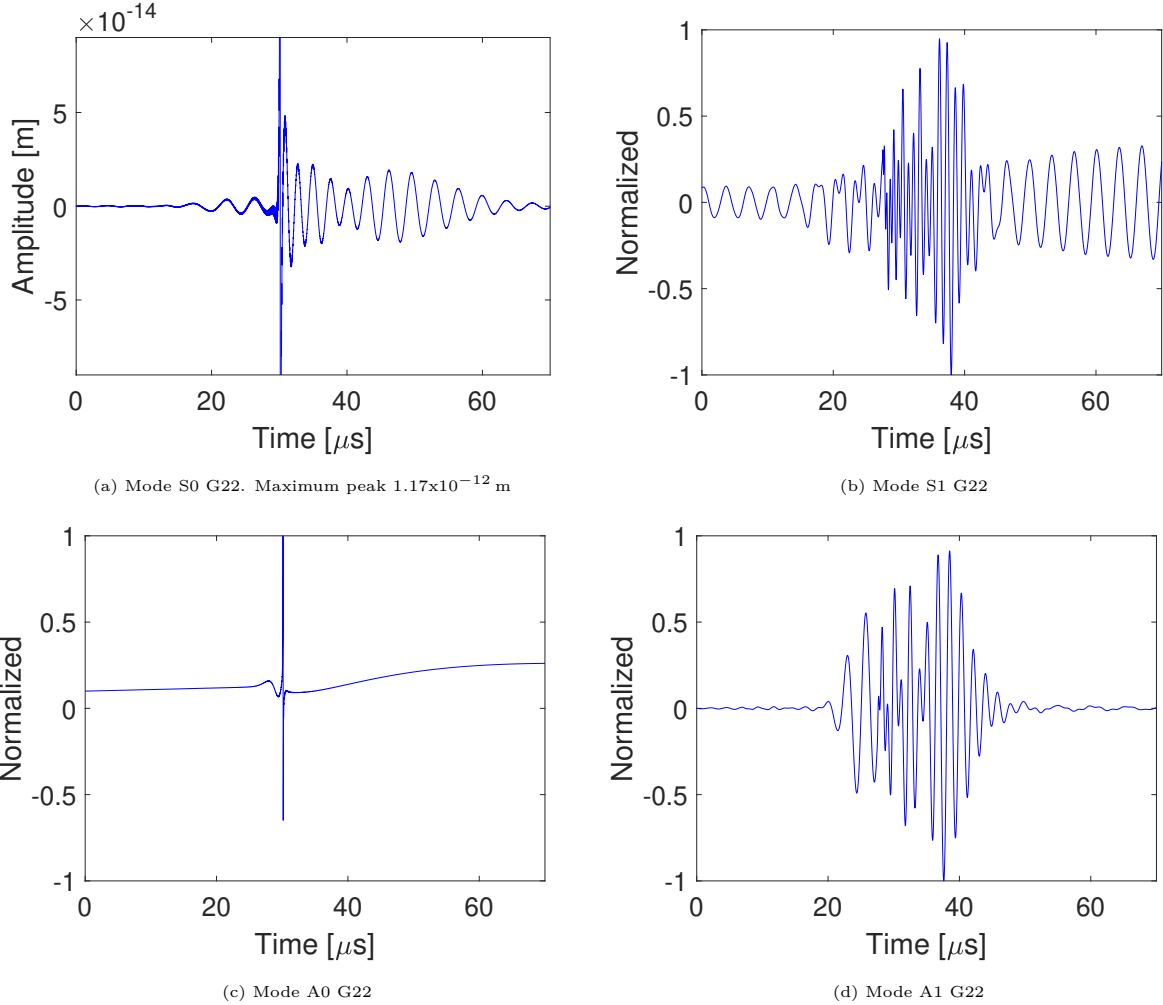
Figure 3.4: Response to a surface normal load, step function H(t) with unit amplitude, in a glass plate with properties: $c_1 = 5.76 \, \text{mm}/\mu\text{s}, \ c_2 = 3.49 \, \text{mm}/\mu\text{s}, \ \text{and} \ \rho = 2.3 \, \text{g/cm}^3$

3.3.2 Multilayered plates

For the last case study, the modal functions for the Green's function are obtained through the SVD applied to the Global Matrix. To this end, the aluminum plate is modeled as a layered plate with three isotropic layers, whose thicknesses are listed from top to bottom as follows: 1 mm, 2 mm, and 1 mm. As a result of the comparison between the displacements U_1 and U_2, which are calculated by using the Residue Theorem approach, and their equivalent pairs G21 and G22, the spectra do not show any difference. However, the distribution through

20

(a) 10 kHz

(b) 100 kHz
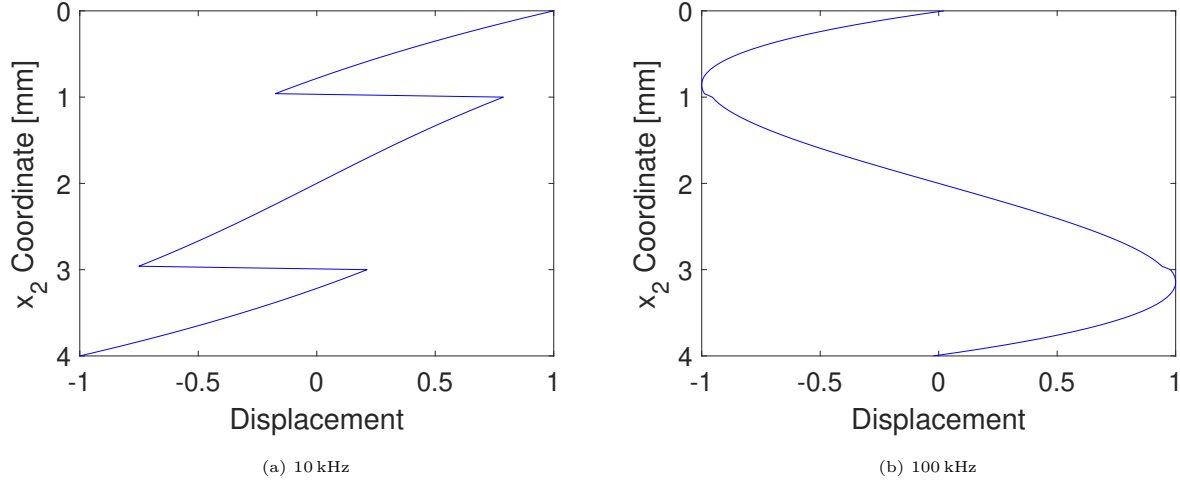
Figure 3.5: Normalized distribution of the shear stress T212(S_{12}) in a 3 layers aluminum plate due to a surface normal load for selected frequencies. Plate's properties listed in Fig. 3.2

the thickness of the shear stress T212 (S_{12}) (of the S0 mode is significantly discontinuous between layers in the frequency range between $10\,\mathrm{kHz}$ and $100\,\mathrm{kHz}$, as seen in Fig. 3.5. It might be the result of the approximation of the modal functions by SVD of the Global Matrix. However, no discontinuity is found in the other stresses, T211 (S_{11}) and T222 (S_{22}), in the frequency range of this study, $10\,\mathrm{kHz}$ and $1000\,\mathrm{kHz}$.

3.4 Transmitted Field Calculation in Plates with Geometric Features Like Steps

In this section the new Green's function is applied to approximately solve the transmission amplitudes of waves traveling toward a reduced section of an isotropic two-dimensional guided wave (see Fig 3.6a). By enclosing the domain of interest with a contour S, as shown in Fig 3.6a, the transmitted field can be calculated by integration over the four sections, in which contour S has been divided, with the integral Eq. 3.23 [18].

$$u_k\left(\mathbf{x}\right) = \sum_m \int \left\{ G_{ki}^m\left(\boldsymbol{\xi}, \mathbf{x}\right) \tau_{ij}^m\left(\mathbf{u}\right) - u_i^m\left(\boldsymbol{\xi}\right) \tau_{ij}^m\left(\mathbf{G_k}\right) \right\} n_j \mathrm{dS} \qquad (3.23)$$

where m represents all the possible modes of waves propagating in the transmitted region.

(a) Guided wave with contour of integration

(b) Dispersion curves for sections left (dashed line) and right (solid line) to the step
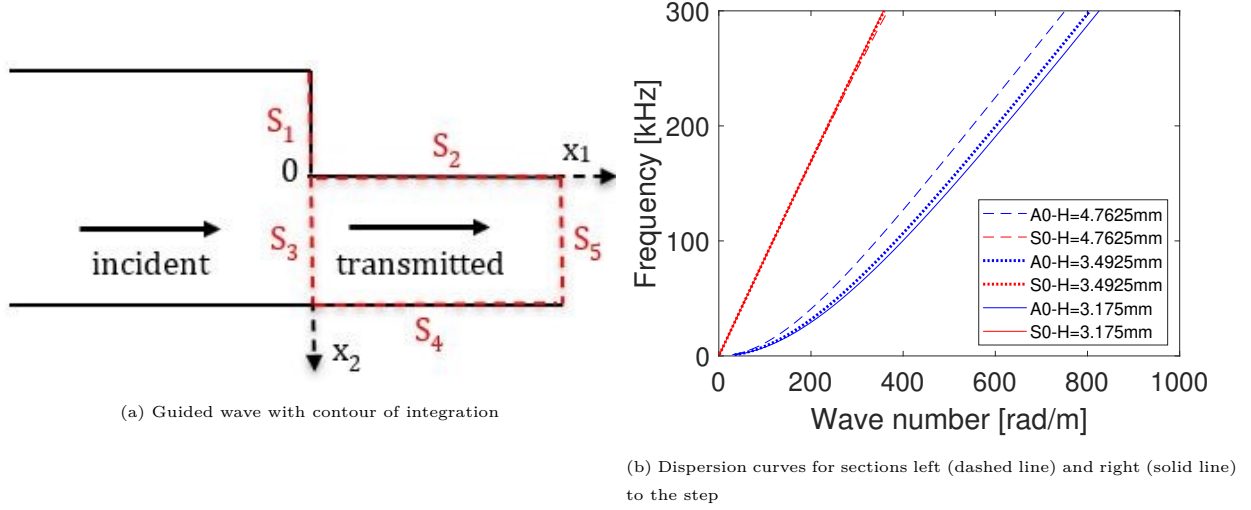
Figure 3.6: Aluminum guided wave with thickness reduction

Application of the traction free boundary conditions to the integrals over the sections S_2 and S_4, and the fact that the integrand is identically zero at section S_5, the transmitted field can be obtained by the integration over the surface S_3. In this way, the Eq. (3.23) is reduced to Eq. (3.24)

$$u_k(\mathbf{x}) = \sum_m \int_{S_3} \left\{ G_{ki}^m(\xi_2, \mathbf{x}) \tau_{i1}^m(\mathbf{u}) - u_i^m(\xi_2) \tau_{i1}^m(\mathbf{G_k}) \right\}_{\xi_1=0} (-1) \mathrm{d}\xi_2 \qquad (3.24)$$

The integral equation can be solved approximately by means of the successive or iterative approximations known as the Born series. The zero-order solution is given by $(u_i^m)_0 = (u_i^n)^{inc}$, where the subscript 0 referrers to the zero-order solution. The first-order solution $(u_i^m)_1$ is obtained by inserting $(u_i^m)_0 = (u_i^n)^{inc}$ into the integral. The second-order solution is obtained by inserting $(u_i^m)_1$ into the integral equation. Continuing this way, (u_i^m) can be obtained to any desired order. In the case that the step is small enough, compared to the wavelength of the incident waves, so the Green's function will distort only slightly the incident field, the first Born approximation can be applied. The first Born approximation consists then of approximating the transmitted wave functions by the incident waves. Thus, using $(u_i^n)^{inc}$ in Eq. (3.24), the transmitted displacement in the first-order approximation can

22

be written as follows:

$$u_k(\mathbf{x}) \approx \sum_n \sum_m \int_{S_3} \left\{ (u_i^n(\xi_2'))^{\text{inc}} \tau_{i1}^m(\mathbf{G_k}) - G_{ki}^m(\xi_2, \mathbf{x})(\tau_{i1}^n(\mathbf{u}))^{\text{inc}} \right\}_{\xi_1=0} d\xi_2 \qquad (3.25)$$

where ξ_2' corresponds to the translated coordinate for the incident field and n represents all the possible modes of waves propagating in the incident region.

Substituting the Green's function from Eq. (3.19) for advancing waves $x_1 > \xi_1$ into Eq. (3.25), we have the equation to calculate the transmitted displacement

$$u_k(x_2) \approx \sum_n \sum_m \frac{U_k^m(x_2)}{R^m} \int_{S_3} \left\{ (u_i^n(\xi_2'))^{\text{inc}} (T_{i1}^m(\mathbf{u})(\xi_2))^* - (U_i^m(\xi_2))^* (\tau_{i1}^n(\mathbf{u}))^{\text{inc}} \right\}_{\xi_1=0} d\xi_2$$
$$(3.26)$$

where the approximate amplitude A^m for the transmitted wave u^m due to the incident wave u^n can be easily found. Note that to simplify the Eq. (3.26), the wave propagation term has been omitted.

To study the effects of the first-order approximation on the calculation of the transmitted displacements, two cases are modeled for an aluminum guided wave with properties: $c_1 = 6.2\,\text{mm}/\mu\text{s}$, $c_2 = 3.1\,\text{mm}/\mu\text{s}$, and $\rho = 2.7\text{e}-6\,\text{kg/mm}^3$. In the first case, waves are transmitted to a guided wave with thickness $3.175\,\text{mm}$ from a $10\,\%$ elevated guided wave. In the second case, the elevation is increased to $50\,\%$. The maximum frequency in the study has been limited to $300\,\text{kHz}$ to guarantee only propagating waves in the fundamental modes for all cases. Fig. 3.7 shows the spectra of the transmitted displacement, which has been normalized with respect to the incident displacement evaluated at the origin. The results in Fig. 3.7a show that there is essentially no mode conversion from S0 mode incident waves to the A0 mode transmitted waves. For all the other cases, which include the displacement presented in Figs. 3.7b to 3.7d, the mode conversion is more notorious as the frequency increases. However, the results do not satisfy energy balance, and they are not consistent with the ones presented in [74]. Therefore, one could conclude that the first order approximation cannot be applied to the calculation of the transmitted field when only propagating Lamb waves are considered.
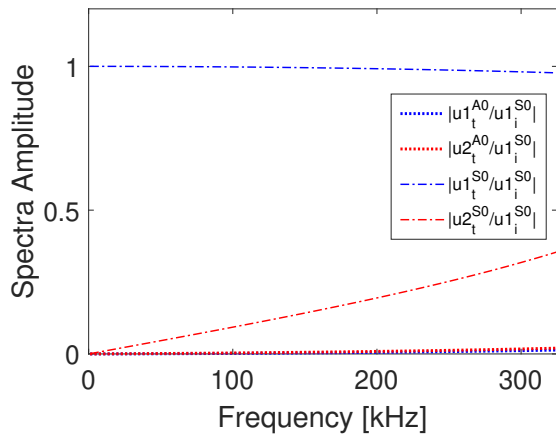
(a) Incident S0 mode 10 %
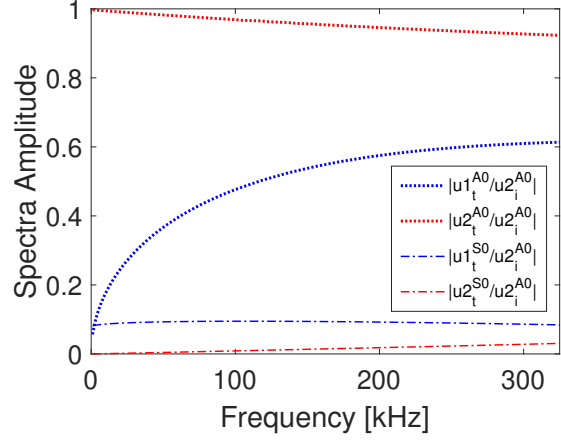
(b) Incident A0 mode 10 %
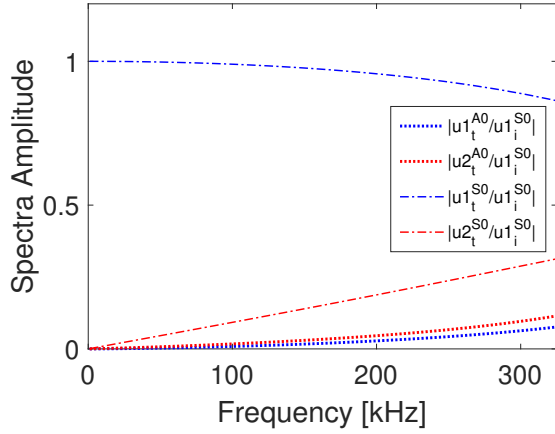
(c) Incident S0 mode 50 %
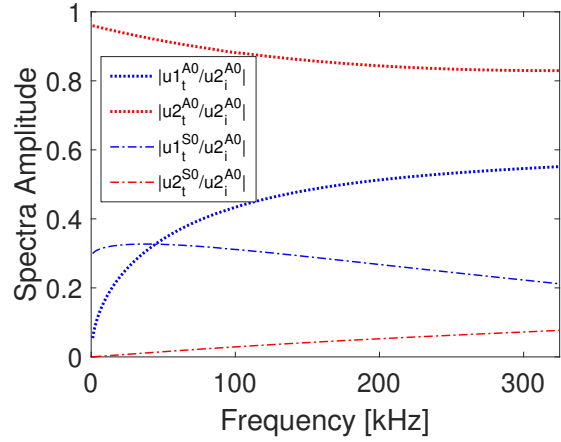
(d) Incident A0 mode 50 %

Figure 3.7: Normalized transmitted displacements on surface $x_2 = 0$

3.5 Acoustic Emission Waveform from the Initiation of Microcracks

3.5.1 Model

Consider an elastic multilayered structure with known Green's function where the wave propagation is not affected by scattering sources other than the formation of an isolated crack. The displacement vector $\mathbf{u}(\mathbf{x})e^{-i\omega t}$ in each mode satisfies the equation of motion,

$$\sigma_{ij,j}(\mathbf{u}) + \rho\omega^2 u_i = 0 \qquad i, j = 1, 2, 3 \tag{3.27}$$

at all points within the medium except at the interfaces. Furthermore, $u_i(\mathbf{x})$ and $\sigma_{i2}(\mathbf{u})$ are continuous across each interface, and $\sigma_{i2}(\mathbf{u}) = 0$ on the top and bottom surfaces of the multilayered media.

According to [45, 7], the displacement field from crack initiation and propagation can be calculated by the expression,

$$U_k(\mathbf{x}, \omega) = \int_S [U_i(\boldsymbol{\xi}, \omega)]_-^+ T_{ij}^k(\boldsymbol{\xi}, \mathbf{x}, \omega) n_j^+ ds \qquad (3.28)$$

where $[U_i(\boldsymbol{\xi}, \omega)]_-^+$ represents the displacement discontinuity at the location of the crack $\boldsymbol{\xi}$, T_{ij}^k are the components of the stress vector on the crack surface S at $\boldsymbol{\xi}$ due to a point force at x (Eq. 3.20), and n_j^+ is the normal on the positive face of the crack S^+.

The elastodynamic field produced by a small surface element $\mathbf{ds}$ of the microcrack is given by [45, 7],

$$U_k(\mathbf{x}, \omega) = [U_i(\boldsymbol{\xi}, \omega)]_-^+ T_{ij}^k(\boldsymbol{\xi}, \mathbf{x}, \omega) n_j^+ ds \qquad (3.29)$$

If the displacement discontinuity $[U_i(\boldsymbol{\xi}, \omega)]_-^+$ can be represented by a normalized function f(t) with magnitude D, which is the maximum static of the dislocation on $\mathbf{ds}$, then the above Eq. (3.29) becomes

$$U_k(\mathbf{x}, \omega) = D\, ds\, F(\omega)\, \gamma_i^+ T_{ij}^k(\boldsymbol{\xi}, \mathbf{x}, \omega) n_j^+ \qquad (3.30)$$

where γ^+ denotes the direction of the dislocation on the positive face of $\mathbf{ds}$, and $F(\omega)$ is the Fourier Transform of f(t). It should be noted that the field produced by a finite crack with known properties can be calculated by evaluating the integral in Eq. (3.28)

In the case where the field equations are independent of one of the coordinates (x_3, ξ_3) and $x_1 > \xi_1$, T_{ij}^k may take the form of Eq. (3.20) for advancing waves. Therefore, Eq. (3.30) can be written as,

$$U_k(x_2, \omega) = D\, ds\, F(\omega) \sum_m \frac{U_k^m(x_2)}{R^m} \gamma_i^+ \left(S_{ij}^m(\xi_2)\right)^* n_j^+ e^{ik_m(x_1 - \xi_1)}; \; x_1 > \xi_1 \qquad (3.31)$$

where $\mathbf{ds}$ represents a line element instead of a surface element.

As a special case where the element δs of arbitrary orientation is at the origin of the coordinate system, the expression to calculate the displacement can be defined in terms of

25
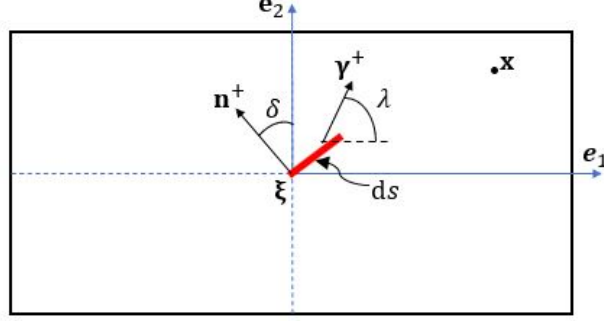
Figure 3.8: Geometry of the crack with its origin at origin of the coordinate system

the angles δ and λ. The angle δ is made between the unit normal $\mathbf{n}^+$ and $\mathbf{e2}$, and λ is the angle between $\mathbf{e1}$ and γ^+ as shown in Figure 3.8.

The unit vectors are then defined with the angles δ and λ as,

$$\mathbf{n}^+ = -\mathbf{e}_1\sin\delta + \mathbf{e}_2\cos\delta \quad \gamma^+ = \mathbf{e}_1\cos\lambda + \mathbf{e}_2\sin\lambda$$

Thus Eq. (3.31) may be expressed as,

$$U_k(x_2,\omega) = D\ ds\ F(\omega)\sum_m \frac{U_k^m(x_2)}{R^m}\{\Lambda\}\,e^{ik_m(x_1-\xi_1)};\ x_1 > \xi_1 \tag{3.32}$$

where,

$$\Lambda = -\cos\lambda\sin\delta\,(S_{11}^m(\xi_2))^* + \sin\lambda\cos\delta\,(S_{22}^m(\xi_2))^* + \cos(\lambda+\delta)(S_{12}^m(\xi_2))^*$$

In this model, the form of the displacement in the vicinity of the crack is determined by the orientation and direction of the crack, the mode shapes of the propagating waves, and the function describing the sudden jump in the displacement at the origin of the crack. Notice that the crack's size does not affect the waveform.

3.5.1.1   Mode-I microcrack

By setting the $\delta = 90°$ and $\lambda = 180°$, the sudden separation of the two sides of the microcrack takes place on the vertical plane of the plate, $x_1 = 0$ as shown in Fig. 3.9a. As a result of the discontinuity in the material, only the normal components S_{11} of the stress tensor $\mathbf{T}$

26

(a) Mode I (b) Mode II
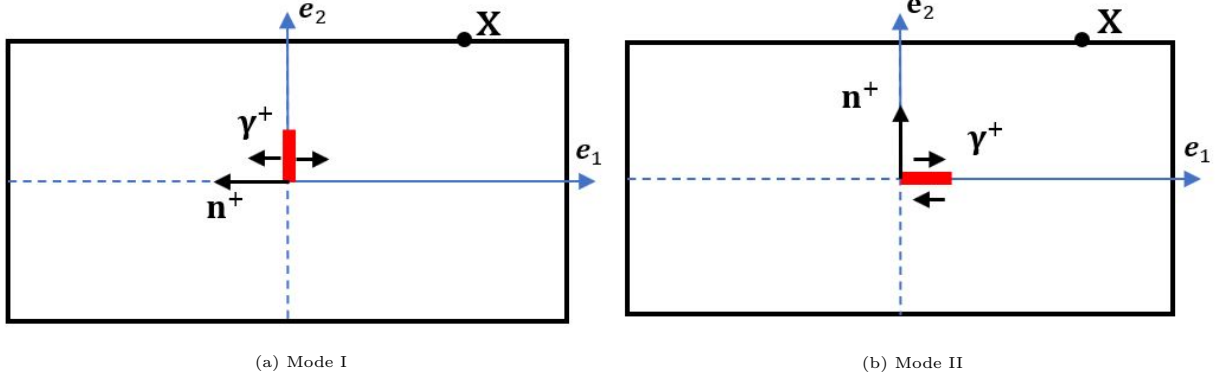
Figure 3.9: Crack orientations in a plate

of the symmetric modes contribute to the displacement. Substituting the angle values into Eq. (3.32) we have,

$$U_k\left(x_2, \omega\right) = D\ ds\ F\left(\omega\right) \sum_m \frac{U_k^m\left(x_2\right)}{R^m} \left\{\left(S_{11}^m\left(\xi_2\right)\right)^*\right\} e^{ik_m\left(x_1 - \xi_1\right)};\ x_1 > \xi_1 \qquad (3.33)$$

where m represents only the symmetric and propagating modes.

3.5.1.2 Mode-II microcrack

In this model, the discontinuity of the displacement is developed on the middle plane of the plate, $x_2 = 0$ as depicted in Fig. 3.9b. As a result of the slip in the material, only the shear components of the stress tensor **T** of the antisymmetric modes add to the displacement. Thus by setting the $\delta = 0°$ and $\lambda = 0°$, Eq. (3.32) becomes

$$U_k\left(x_2, \omega\right) = D\ ds\ F\left(\omega\right) \sum_m \frac{U_k^m\left(x_2\right)}{R^m} \left\{\left(S_{12}^m\left(\xi_2\right)\right)^*\right\} e^{ik_m\left(x_1 - \xi_1\right)};\ x_1 > \xi_1 \qquad (3.34)$$

where m represents only the antisymmetric family of propagating modes.

3.5.1.3 The displacement discontinuity function

The Heaviside step function H(t) may be initially chosen to represent the discontinuity of the displacement f(t). However, this function might not be physically consistent with the fact that the displacement, prior to becoming constant, should start the sudden onset at

27

(a) Time Series

(b) Fourier Transform of Fig. 3.10a (logarithmic scale)
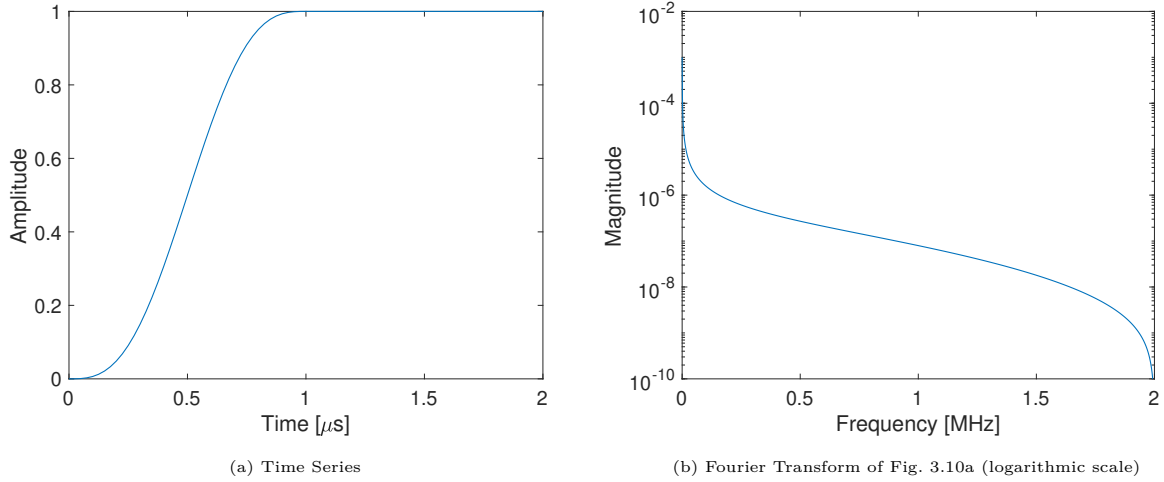
Figure 3.10: Displacement discontinuity function for $\tau = 1\,\mu$s

t = 0 and end it with velocity v = 0. Therefore, the consideration of the modulated ramp function perhaps represent better the physics of the event. The proposed modulated ramp function and its Fourier time transform are,

$$f(t) = \left(t/\tau - \left(\frac{1}{2\pi}\right)\sin\left(\frac{2\pi t}{\tau}\right)\right)H(t - \tau) \tag{3.35}$$

$$F(\omega) = -\frac{\tau}{\omega^2\tau^2}\left(1 - e^{-i\omega\tau}\right)\left(\frac{1}{1 - \frac{4\pi^2}{\omega^2\tau^2}} - 1\right) + \pi\delta(\omega)e^{-i\omega\tau} \tag{3.36}$$

where τ is the rise time of the displacement's jump. Fig. 3.10 shows the functions for $\tau = 1\,\mu$s. It should be noted that Eq. (3.36) has a singularity of $0(1/\omega)$, which has been handled by the time domain inversion algorithm IFFT [83]. Following a different approach, [21, 7] did not use the Eq. (3.36) to compute the displacement, but instead used the FFT of Eq. (3.35) followed by the application of a band-pass filter. Both approaches have been applied in Section. 3.5.1.2, and the results are up to some extent different.

3.5.2   Plate response to mode I and mode II microcracks

In this section, the models presented in Section. 3.5.1.1 and 3.5.1.2 are applied to the calculation of the vertical displacement on the top surface of a plate at X = 50 mm using a rise time $\tau = 1\,\mu s$ to study the effects of different functions f(t), crack orientations and crack directions

28

on the waveform. The first 25 propagating modes have been considered in the calculation, and a Bessel band-pass filter of the first order $0.05\,\mathrm{MHz} - 2\,\mathrm{MHz}$ has been applied for both cases. The results are presented in Figs. 3.11-3.14 for an aluminum plate with thickness $10\,\mathrm{mm}$ and properties: $c_1 = 6.2\,\mathrm{mm}/\mu s$, $c_2 = 3.1\,\mathrm{mm}/\mu s$, and $\rho = 2.7\mathrm{e} - 6\,\mathrm{kg}/\mathrm{mm}^3$.

In Section. 3.5.1.3, alternatives to handle the numerical error produced by the source-function's singularity $0(1/\omega)$ on the calculation of the displacement have been introduced. In order to treat the singularity, one option is to use Eq. (3.36) to obtain the displacement in the frequency domain followed by the implementation of the IFFT to get the displacement's time series [83]. The result of using this procedure are depicted in Figs. 3.11a and 3.11b. An alternative approach to calculate the displacement is to use the FFT of Eq. (3.35) instead of the its analytical FT expression [21, 7]. The results are shown in Figs. 3.11c and 3.11e. It can be seen from the comparison between the spectra that the singularity $0(1/\omega)$ dominates the spectrum of the first approach at low frequencies, while the displacement obtained through the FFT of f(t) in the second option exhibits better control of the singularity. However, the static displacement for large times described in [83] cannot be captured by the second approach. On the other hand, the waveform with positive peak at $17.65\,\mu s$ in the displacement obtained through the first approach is significantly different compared to the one from experimental measurements [21]. The waveform with the maximum peak in the result through the second option arrives a little earlier at $16.88\,\mu s$. There is a third option which has been explored with excellent results. Since the study of the effect of the ramp on the calculations is our main objective, removing the part related with the DC component from Eq. (3.36) may help to overcome the numerical issue at $\omega = 0$. The modified expression is given by,

$$F\left(\omega\right) = \frac{4\pi^2 \left(1 - \mathrm{e}^{-\mathrm{i}\omega\tau}\right)}{\omega^2\tau \left(4\pi^2 - \omega^2\tau^2\right)} - \frac{\mathrm{i}}{\omega} \tag{3.37}$$

Fig. 3.11e shows that there is no distinction between the results obtained through the Eq. (3.37), and the FFT. However, by looking at the spectra of the second and third options in Fig. 3.11f, it should be noted that the two solutions become slightly different at frequencies higher than $10\,\mathrm{MHz}$.

In addition to the f(t)'s singularity, the other issue discussed in Section. 3.5.1.3 is the effect of using the modulated ramp mr(t) over the Heaviside function H(t) as the source f(t). By using H(t) as a source, the time series of the displacement becomes noisy, as shown in Fig. 3.12, when it is compared to Fig. 3.11d. The manifestation of the noise in the waveform might be the result of the lack of a smooth transition in the source function between t = 0 and the time when the maximum static displacement is achieved. Applications of different filters have not improved the waveform.

As a result of the observation of the results presented in Fig. 3.11, one can infer that using the modulated ramp function with its FFT as the source to compute the displacement provides an acceptable representation of its waveform in the frequency range of this study.

Shown in Fig. 3.13 is the displacement of the microcrack mode-I. In contrast to the resultant displacement from a microcrack mode-II's, the contribution of the symmetric modes arise in a completely different waveform with lower amplitude vibrations for $t < 8\,\mu s$. Furthermore, after the first arrival, there is a sudden peak with higher amplitude, followed by some vibrations for $t > 22\,\mu s$. The vibrations' amplitude is up to 2 times higher than the oscillations present in the waveform depicted in Fig. 3.11d for $t > 18\,\mu s$.

In order to fully define the source function, the rise time τ can be obtained from experimental measurements [21]. In the study, the value of τ was associated with different mechanisms of failure in CFRP plates. However, in this study , it has been noticed that the waveform from the calculations of the displacement using different values of τ are fairly the same. As an example, Fig. 3.14 shows the waveform of the displacement for different values of τ ($0.5\,\mu s$, $1\,\mu s$ and $2\,\mu s$) for microcracks of type Mode-I and Mode-II. In all cases, only a very small difference in the time of arrivals is observed which leads to the conclusion that the rise time of the modulated ramp does not have a significant effect in the time series of the displacement other than its amplitude.

As the last case of study in this section, the vertical displacement on the top surface of a thin aluminum plate with thickness $1\,\mathrm{mm}$ at X = $5\,\mathrm{mm}$ using a rise time $\tau = 1\,\mu s$ is calculated. The properties of the plate are: $c_1 = 6.2\,\mathrm{mm}/\mu s$, $c_2 = 3.1\,\mathrm{mm}/\mu s$, and $\rho = 2.7\mathrm{e} - 6\,\mathrm{kg}/\mathrm{mm}^3$.

Applying a Bessel band-pass filter of the first order $0.05\,\text{MHz} - 2\,\text{MHz}$, the results are presented in Figs. 3.15 - 3.17. Compared to the results of the thick plate, the waveform presents less oscillations for the mode-I case, as it can be seen in Fig. 3.15b, and the waveform of the mode-II case presents a more notorious settle down to the static value, as shown in Fig. 3.15d.

To analyze the influence of the location of the sensing point X in the results, the vertical displacement is calculated for two additional distances, $X = 10\,\text{mm}$ and $X = 50\,\text{mm}$. At $50\,\text{mm}$ for the Mode-I case, the high frequency oscillations after the first arrival develop into two well defined packets between $24\,\mu\text{s}$ and $31\,\mu\text{s}$, as illustrated in Fig. 3.16f. Similar packets are not clearly identified at the other two distances, as shown in Figs. 3.16d and 3.16e.

For the mode-II case, it is noticed for the three distances in Fig. 3.17 that the first arrival corresponds to the contribution of the mode A0 to the displacement, and that the higher modes are visible as tiny oscillations after the first arrival. Another observations are the $180°$ wave shifting at $X = 10\,\text{mm}$, and the low frequency oscillation at $X = 50\,\text{mm}$ in Figs. 3.17e and 3.17f, respectively.
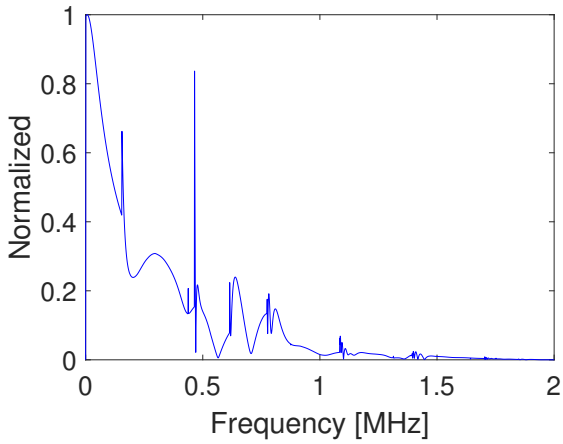
(a) Spectrum of Fig. 3.11b
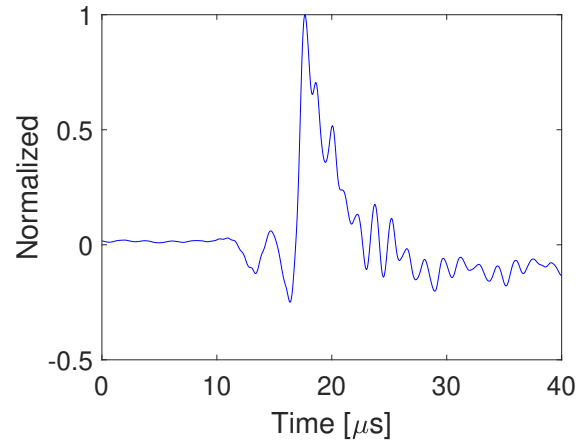
(b) Time series using analytical FT of mr(t)
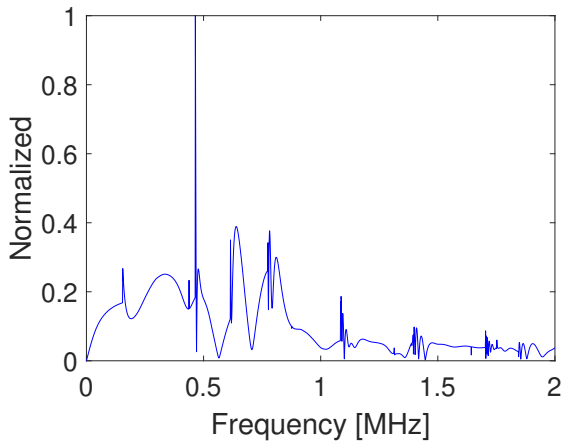
(c) Spectrum of Fig. 3.11d
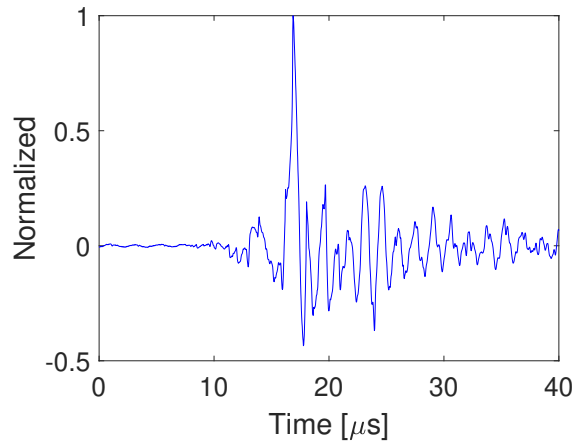
(d) Time series using FFT of mr(t)
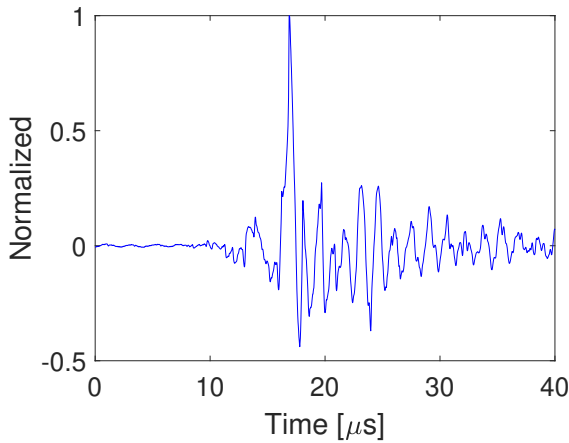
(e) Time series using modified analytical FT of mr(t)
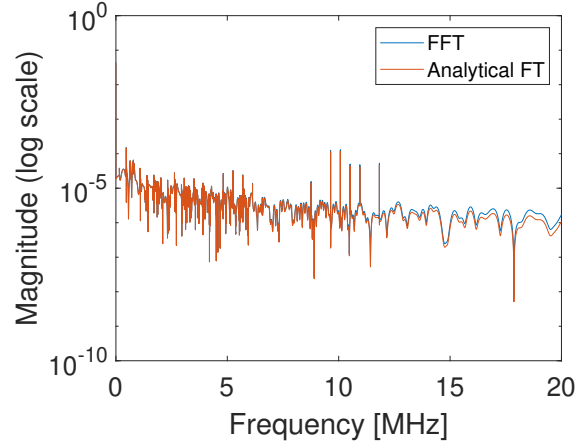
(f) Spectra of Figs. 3.11d (FFT) and Fig. 3.11e (Analytical FT)

Figure 3.11: Vertical surface displacement due to a mode-II microcrack at X = 50 mm in an aluminum plate with thickness 10 mm
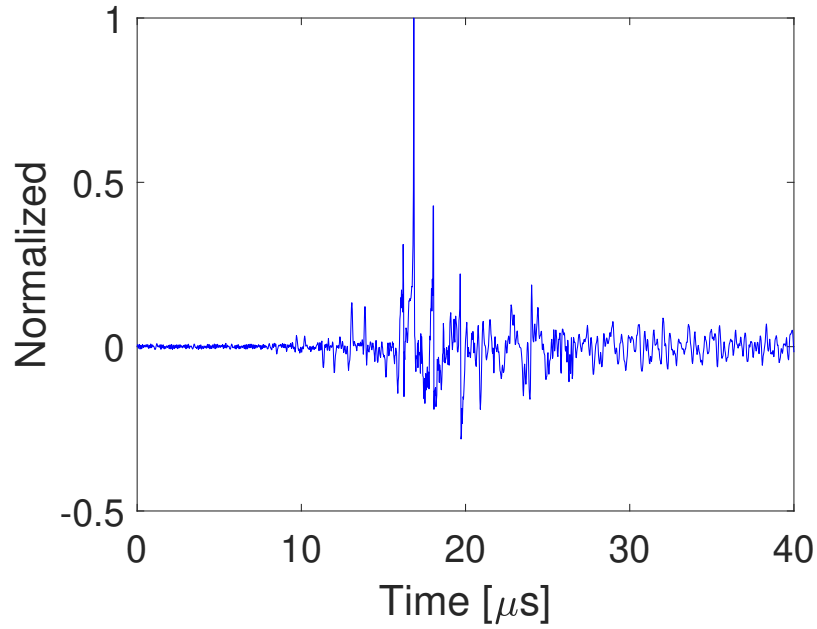
Figure 3.12: Vertical surface displacement due to a mode-II microcrack at $X = 50\,\text{mm}$ in an aluminum plate with thickness $10\,\text{mm}$ with Heaviside step H(t) as the source.

(a) Spectrum of Fig. 3.13b

(b) Time series using FFT of the source
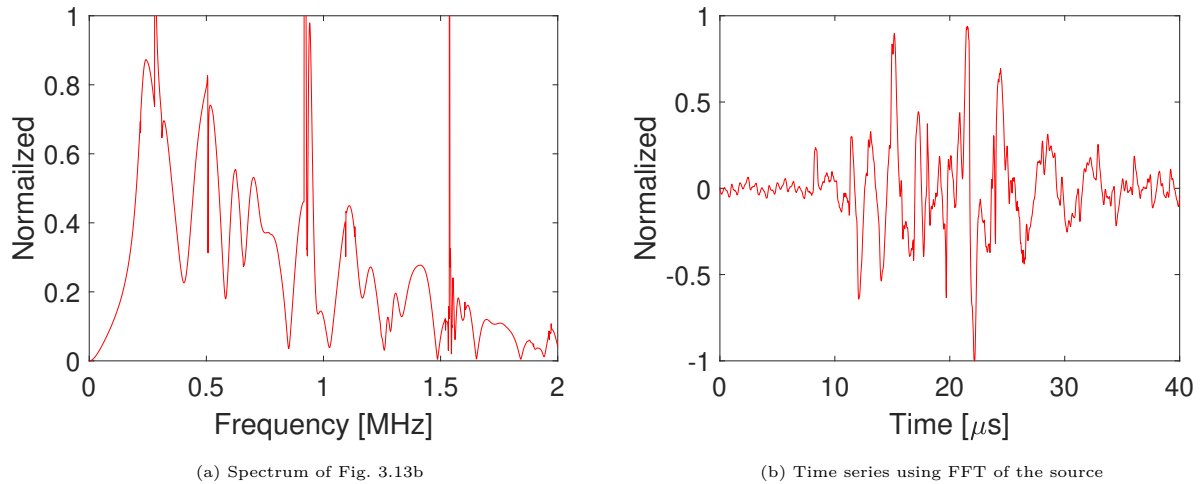
Figure 3.13: Vertical surface displacement due to a mode-I microcrack at $X = 50\,\text{mm}$ in an aluminum plate with thickness $10\,\text{mm}$
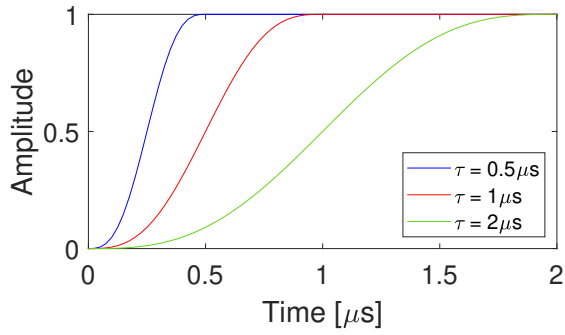
(a) Displacement Discontinuity Function
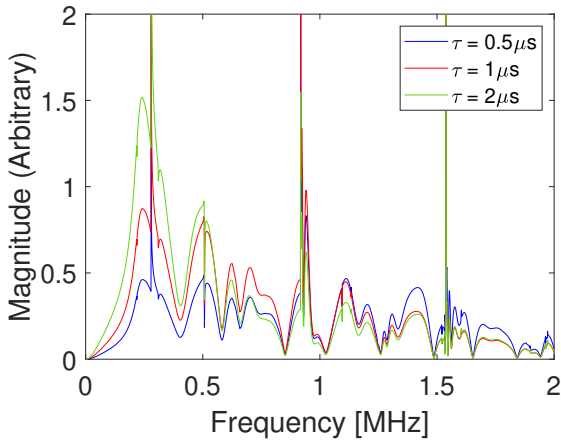
(b) Spectrum of Fig. 3.14c
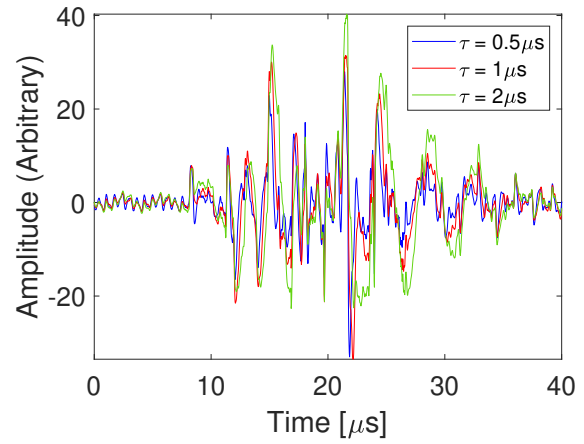
(c) Time series (Mode-I)
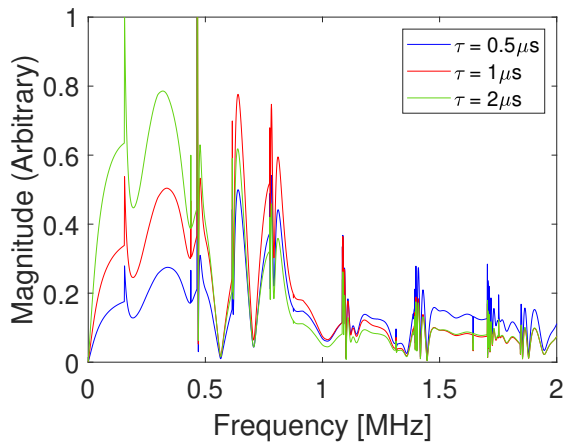
(d) Spectrum of Fig. 3.14e
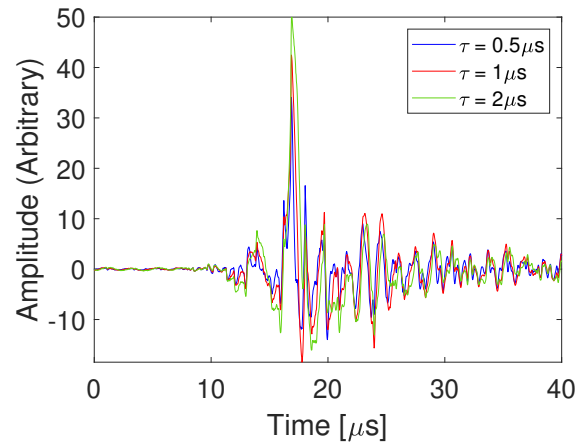
(e) Time series (Mode-II)

Figure 3.14: Vertical surface displacement at X = 50 mm due to a microcrack in an aluminum plate with thickness 10 mm and various rise times τ

34
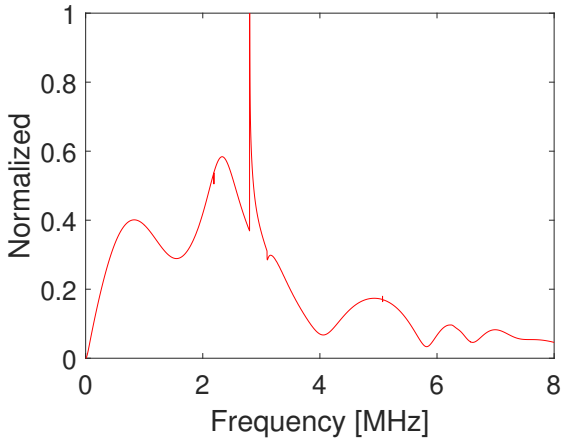
(a) Spectrum of Fig. 3.15b
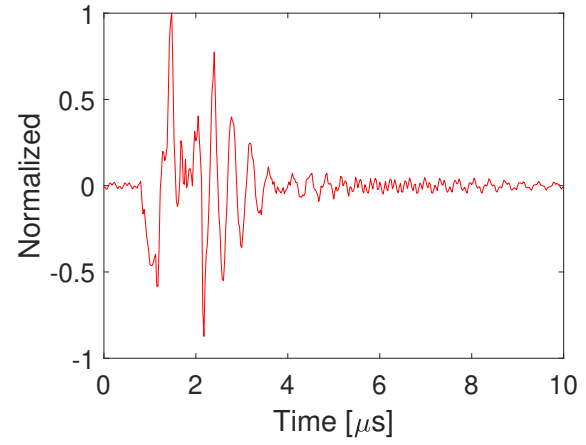
(b) Time series (Mode-I)
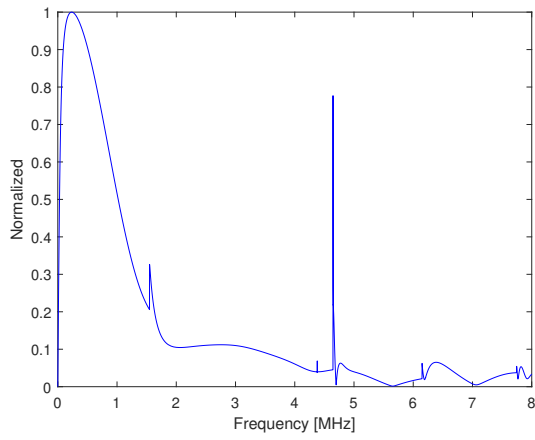
(c) Spectrum of Fig. 3.15d
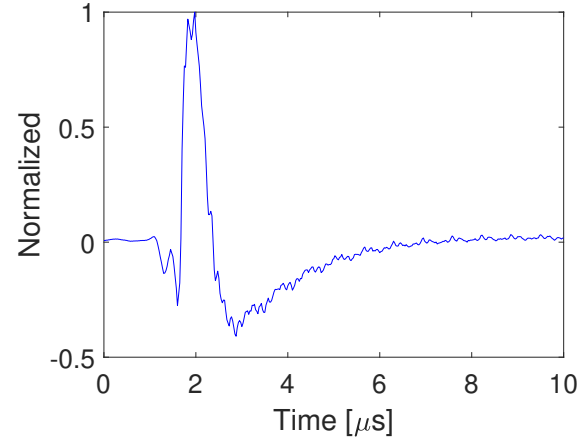
(d) Time series (Mode-II)

Figure 3.15: Vertical surface displacement at X = 5 mm due to a microcrack in an aluminum plate with thickness 1 mm

(a) Spectrum of Fig. 3.16d   (b) Spectrum of Fig. 3.16e   (c) Spectrum of Fig. 3.16f

(d) Time series at X = 5 mm   (e) Time series at X = 10 mm   (f) Time series at X = 50 mm
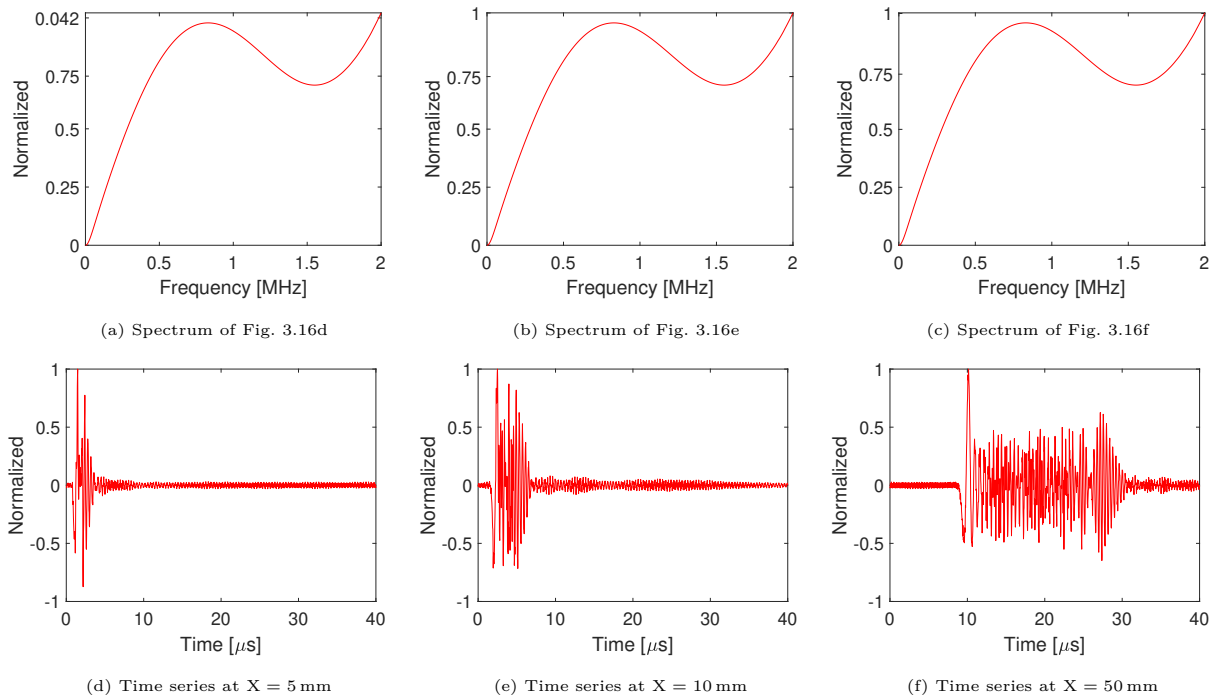
Figure 3.16: Vertical surface displacement due to a mode-I microcrack in an aluminum plate with thickness 1 mm at various sensing points

(a) Spectrum of Fig. 3.17d

(b) Spectrum of Fig. 3.17e

(c) Spectrum of Fig. 3.17f

(d) Time series at X = 5 mm

(e) Time series at X = 10 mm

(f) Time series at X = 50 mm
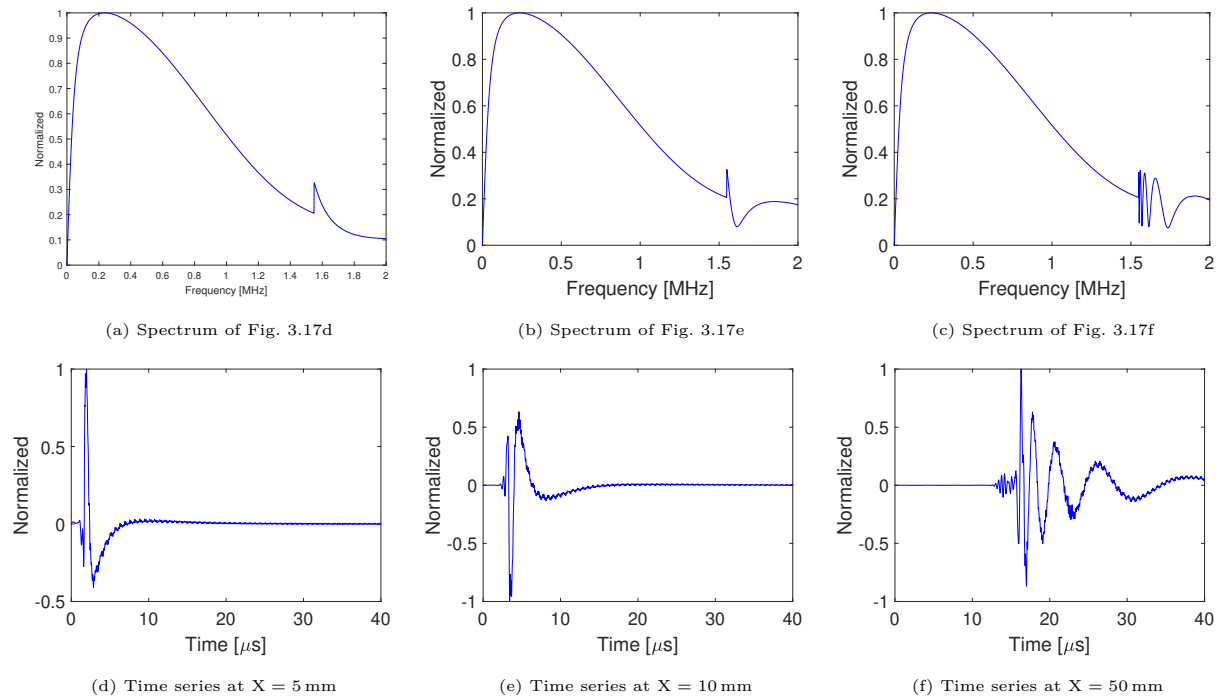
Figure 3.17: Vertical surface displacement due to a mode-II microcrack in an aluminum plate with thickness 1 mm at various sensing points

CHAPTER 4

Uncertainty Analysis Applied to Material Characterization

Manufacturing of composite materials typically results in a higher variability as compared to manufacturing with conventional materials. As an example, laminates made out of fiber-reinforced polymer matrix composites that are used in many modern critical structures, require sophisticated process control to avoid compromising the structural integrity throughout the entire life cycle of the components and systems. Thus, efficiently determining the material properties and their degradation may be the key to allow for an even more widespread adoption of composites.

In addition to the stacking sequence of the laminates, the strength and stiffness of fiber-reinforced polymers (FRPs) are largely dominated by the fiber characteristics in each ply as well as the quality of the bonding at the fiber-matrix interfaces [82]. Standards, such as ASTM D3039M or D7264M, to determine the effective material properties of composites have been defined. However, the destructive nature of the tests requires resource-intensive preparation and evaluation of samples, these methods are not suitable for in-situ applications. Moreover, with continuous improvements in manufacturing techniques and the development of new material architectures, there is a growing need for material characterization and testing. In particular, natural fiber composites, including hemp [56] and flax fibers [63], have received increasing attention in recent years [39]. Due to the natural nature of the fibers, inherent variability in the overall properties of these composites as compared to synthetic fibers is higher. Additionally, fiber-matrix bonding is found to be challenging and requires chemical treatment and continuous testing during development and production [32].

Nondestructive testing (NDT) methods are appealing to address these testing needs. Previous studies for material characterization of anisotropic media used ultrasound velocity measurements from a through-transmission technique to calculate the elastic constants in a unidirectional glass fiber-reinforced polymer [94] and cubic crystals through an optimization procedure [17]. In other studies, phase velocity measurements from leaky Lamb waves are used together with inversion schemes [68, 69, 34, 10] or ray theory [8] to obtain the material constants in unidirectional carbon fiber-reinforced polymers (CFRPs). However, these techniques rely on the water immersion of the specimen. In an attempt to simplify the leaky Lamb waves techniques, an approach of using a pair of variable-angle contact transducers in a pitch-catch mode with an inversion procedure was proposed for isotropic plates [67]. More recently, machine learning and other optimization procedures have recently been applied to both numerical models and experimental data [49, 14, 13].

Most of the aforementioned NDT methods, however, do not consider uncertainty [29] in models and material parameters. In addition to interval computation and statistical methods, such as Monte-Carlo Simulations [54], fuzzy arithmetical approaches have been developed to identify epistemic uncertainty in model parameters more efficiently without yielding overestimation [25, 53, 22]. A small number of studies investigated the effect of the variation in the material properties on vibration [26] and mechanical testing [64] of CFRP plates (forward fuzzy analysis). Others researchers have developed fuzzy logic-based structural health monitoring techniques [19, 11] for composite substructures (inverse fuzzy analysis). Early attempts of adopting this methodology for guided wave-based techniques focused on uncertainty propagation in dispersion models [73], model development [71] and their influence on crack detection [72].

To account for the inherent epistemic uncertainty in the material characterization of composites, the development of new NDT techniques is needed. Furthermore, the implementation of the advanced fuzzy arithmetic theory to study the influence of material constants in the group velocity of CFRP may contribute to the implementation of Guided Waves based NDT methods. It has been demonstrated that the influence of the uncertainty in the ma-

terial constants on the wave velocity varies with frequency and wave propagation angle [5]. Following these ideas, the uncertainty in the material constants of a quasi-isotropic CFRP could be identified by applying an inverse procedure based on fuzzy arithmetical theory coupled with experimentally measured group velocities. New nominal values may be result from the defuzzyfication of the identified fuzzy-values of the material properties [4].

In this chapter, the effects of the uncertainty of the material properties on the group velocities of two composite plates is studied in Section 4.3. The first plate is a quasi-isotropic carbon fiber reinforced polymer (CFRP) laminate, which is considered as a homogenized single-layered model. The second plate is a unidirectional CFRP. In section 4.4 a fuzzy model, in conjunction with group velocities obtained from experimental data, is used to generate a new set of material properties by solving an inverse problem through an optimization procedure. To this end, a fuzzy arithmetical approach based on the Transformation Method is used to create the model that represents a monotonic relationship between material properties and Lamb wave velocities, as shown in Section 4.4.3 . The nominal group velocities for a CFRP laminate are calculated through an efficient root finding algorithm. This root-finding algorithm has been developed based on a numerical algorithm to solve transcendental dispersion equations [93]. Additionally, in section 4.4.1, group velocities are extracted from laboratory experiments on a quasi-isotropic CFRP plate at three different locations in order to account for variations in the properties of the laminate. Lastly, it is shown that the uncertainty due to the material properties can be substantially reduced by re-evaluating their nominal values through the inverse fuzzy arithmetic, as shown in section 4.4.5. Furthermore, findings of using a single guided wave mode for this nondestructive material characterization technique are compared with those obtained from a multi-mode analysis.

4.1   Forward Fuzzy Arithmetic

Following the classification by Hoffman and Hammonds [29], one type of uncertainty is due to stochastic variability of the quantities in the model under study. The uncertainty of this type is usually referred to as aleatory uncertainty and represented by a probability. The second

(a) Fuzzy model parameter $\bar{p}_i$

(b) Fuzzy model output $\tilde{q}_k^m$. Experimental data is marked by $\times$
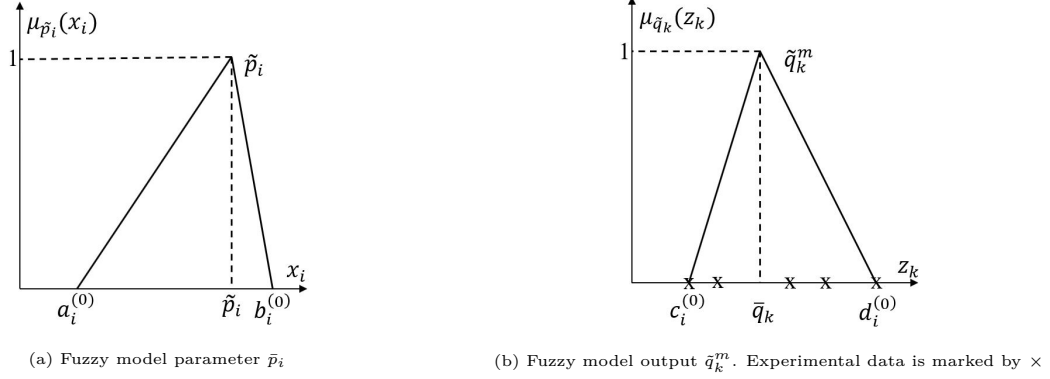
Figure 4.1: Membership functions of triangular fuzzy numbers

type is called the epistemic uncertainty and is derived from the lack of knowledge about the quantities in the analysis. Interval analysis and different theories, including possibility, evidence, and probability are commonly used to represent epistemic uncertainty [27].

Different from parameters defined by real numbers, fuzzy numbers allow the inclusion of the parameter uncertainty and its possibility of occurrence. The possibility of occurrence can be quantified by a triangular function for a linear fuzzy number $\tilde{p}_i$ [25]. This function is known as the membership function $\mu_{\tilde{p}_i}(x_i) \in [0,1]$, whose highest and lowest values are at the nominal value $\tilde{p}_i$ and worst-case interval $[a_i^{(0)}, b_i^{(0)}]$, respectively (see Fig. 4.1a). In this study, the Transformation Method is used to propagate the uncertainty of independent fuzzy input values $\tilde{p}_i$, i=1,...,n, to fuzzy output values $\tilde{q}_k$ in a dynamic model with frequency s as an independent input variable [25, 20].

$$\tilde{q}_k(s) = f_k(\tilde{p}_1, \tilde{p}_2, \ldots, \tilde{p}_n, s), \quad k = 1, \ldots, K \tag{4.1}$$

Based on the type of objective function f, the Transformation Method has two forms, the general and the reduced. The general form takes sampling points between the α-cuts at each membership level for the calculations, while the reduced form only uses the α-cut values. Therefore, the latter form is restricted to linear systems. Considering that f is monotonic with respect to the input variables (as in this case), the five major steps of the Reduced Transformation Method are briefly described as follows:

41

1. Decomposition of the fuzzy input parameters $\tilde{p}_i$, into m intervals (α-cuts) $X_i^{(j)}$

$$P_i = \{X_i^{(0)}, X_i^{(1)}, \ldots, X_i^{(m)}\}, \tag{4.2}$$

where,

$$X_i^{(j)} = \left[a_i^{(j)}, b_i^{(j)}\right], \quad i = 1, \ldots, n, \quad j = 1, \ldots, m. \tag{4.3}$$

2. Transformation of the input intervals $X_i^{(j)}$ into arrays arrays $\widehat{X}_i^{(j)}$

$$\widehat{X}_i^{(j)} = \overbrace{\left(\left(\alpha_i^{(j)}, \beta_i^{(j)}\right), \left(\alpha_i^{(j)}, \beta_i^{(j)}\right), \ldots, \left(\alpha_i^{(j)}, \beta_i^{(j)}\right)\right)}^{2^{i-1}\text{pairs}}, \tag{4.4}$$

where,

$$\alpha_i^{(j)} = \underbrace{\left(a_i^{(j)}, \ldots, a_i^{(j)}\right)}_{2^{n-i}\text{elements}} \quad \text{and} \quad \beta_i^{(j)} = \underbrace{\left(b_i^{(j)}, \ldots, b_i^{(j)}\right)}_{2^{n-i}\text{elements}}. \tag{4.5}$$

3. Evaluation of the model is performed by calculating the function f_k for each column of the array $\widehat{X}_i^{(j)}$ and the independent variable s, using the classical arithmetic of crisp numbers:

$$^r\hat{z}_k^{(j)} = f_k\left(^r\hat{x}_1^{(j)}, {}^r\hat{x}_2^{(j)}, \ldots, {}^r\hat{x}_n^{(j)}, s\right), \quad j = 1, \ldots, m. \tag{4.6}$$

where $^r\hat{x}_i^{(j)}$ is the rth element of the arrays $\widehat{X}_i^{(j)}$. The outputs are then organized in the arrays $\widehat{Z}_k^{(j)}$:

$$\widehat{Z}_k^{(j)} = \left(^1\hat{z}_k^{(j)}, {}^2\hat{z}_k^{(j)}, \ldots, {}^{2n}\hat{z}_k^{(j)2^n}\right). \tag{4.7}$$

4. Retransformation of the output arrays $\widehat{Z}_k^{(j)}$ into intervals $Z_k^{(j)} = [c_k^{(j)}, d_k^{(j)}]$ for each membership level gives the decomposed form of the fuzzy output values $\tilde{q}_k(s)$

$$Q_k = \left(Z_k^{(0)}, Z_k^{(1)}, \ldots, Z_k^{(m)}\right) \tag{4.8}$$

The interval bounds, $c_k^{(j)}$ and $d_k^{(j)}$, are obtained from the recursive formulas

$$c_k^{(j)} = \min_r\left(c_k^{(j+1)}, {}^k\hat{z}_k^{(j)}\right), \quad j = 1, \ldots, m \tag{4.9}$$

$$d_k^{(j)} = \max_r\left(d_k^{(j+1)}, {}^k\hat{z}_k^{(j)}\right), \quad j = 1, \ldots, m \tag{4.10}$$

and

$$c_k^{(m)} = \min_r\left(^k\hat{z}_k^{(m)}\right) = \max_r\left(^k\hat{z}_k^{(m)}\right) = d_k^{(m)} = \bar{z}_k. \tag{4.11}$$

5. Recomposition of the outputs intervals $Z_k^{(j)}$ leads to the fuzzy output values $\tilde{q}_k$ with membership functions $\mu_{\tilde{q}_k}(z_k)$.

To analyze the results of the parameterized dynamic model, the influence of each model parameter $\tilde{p}_i$ can be quantified by the absolute and relative measurement of influence, φ_{ik} and ω_{ik}, respectively. The former shows the absolute uncertainty of each of the model parameters, while the latter normalizes the contribution of the uncertainty of each model parameter in the overall uncertainty [25, 20].

4.2 Inverse Fuzzy Arithmetic

The goal of the Reduced Transformation Method is to propagate the uncertainty of the fuzzy-valued input parameters to the outputs of the model. As a consequence, the accuracy of the results strongly relies on the original guess of the worst-case interval of the input parameters. The inverse fuzzy arithmetical approach allows the identification of the uncertainty of input parameters, worst-case interval, in the dynamic model, based on experimental data of the real system [23]. The steps to implement the inverse fuzzy arithmetical approach are described below:

1. Calculation of the gain factors $\eta_{ki-}^{(j)}$ and $\eta_{ki+}^{(j)}$, based on the arrays $\widehat{X}_i^{(j)}$ and $\widehat{Z}_k^{(j)}$ from the forward simulation with the Reduced Transformation Method, and an interpolation procedure. The gain factors are then assembled in the system $H^{(j)}(s)$. To performed the forward simulation, an assumption of the fuzzy-valued input parameters is needed.

2. Representation of the measured data by linear fuzzy numbers, $\tilde{q}_k^m$, whose worst-case intervals $[c_i^{(0)}, d_i^{(0)}]$ contain all collected data, and their nominal values $\bar{q}_k$ are obtained from the forward simulation (see Fig. 4.1b).

3. Considering that the relation between the input and output uncertainties is linear, the unknown lower and upper bounds, $a_i^j(s)$ and $b_i^j(s)$, of the input parameters are solved

for each μ_j from $U^{(j)}(s)$, through the quadratic objective function

$$J^{(j)}(s) = \frac{1}{2}\mathbf{U}^{(j)T}(s)\mathbf{W}(s)\mathbf{U}^{(j)}(s) \tag{4.12}$$

with linear inequality constraint

$$\mathbf{H}^{(j)}(s)\mathbf{U}^{(j)}(s) \leq \mathbf{M}^{(j)}(s) \tag{4.13}$$

where,

$$\mathbf{U}^{(j)}(s) = \begin{bmatrix} a_1^{(j)}(s) - \bar{p}_1(s) \\ b_1^{(j)}(s) - \bar{p}_1(s) \\ \vdots \\ a_n^{(j)}(s) - \bar{p}_n(s) \\ b_n^{(j)}(s) - \bar{p}_n(s) \end{bmatrix} \tag{4.14}$$

$$\mathbf{M}^{(j)}(s) = \begin{bmatrix} c_1^{(j)}(s) - \bar{q}_1(s) \\ -(d_1^{(j)}(s) - \bar{q}_1(s)) \\ \vdots \\ c_k^{(j)}(s) - \bar{q}_k(s) \\ -(c_k^{(j)}(s) - \bar{q}_k(s)) \end{bmatrix} \tag{4.15}$$

and

$$\mathbf{W}(s) = \mathbf{W} = \mathrm{diag}\left(\frac{1}{\bar{p}_1^2}, \ldots, \frac{1}{\bar{p}_n^2}\right) \quad \forall \bar{p}_i \neq 0 \tag{4.16}$$

4. Recalculation of the resultant input parameters $\tilde{p}_i(s)$ to reduce the undesirable s-dependence is carried out by the introduction of the conservative-parameter $\gamma \in [0, 1]$ together to the union and mean operators. This approach provide input parameters $\tilde{p}_i$, which are representative for all s, with bounds at each μ_j given by

$$a_i^{(j)} = a_{i,\mathrm{mean}}^{(j)} + \gamma\left(a_{i,\mathrm{union}}^{(j)} - a_{i,\mathrm{mean}}^{(j)}\right), \quad i = 1, 2, \cdots, n, \quad j = 0, 1, \cdots, m-1 \tag{4.17}$$

$$b_i^{(j)} = b_{i,\mathrm{mean}}^{(j)} + \gamma\left(b_{i,\mathrm{union}}^{(j)} - b_{i,\mathrm{mean}}^{(j)}\right) \tag{4.18}$$

44

4.3 Analysis of Fuzzy-Parameterized Dynamic Systems

Two models are used to analyze the uncertainty in the calculation of the dispersion curves introduced by the uncertainty in the material properties. The first is a transversely isotropic single-layer. The second model is a unidirectional CFRP plate, which is assumed to be transversely isotropic with the symmetry axis along the fiber direction.The material properties of the models are linear fuzzy parameters, whose nominal values and worst case-interval are given in (Table 4.1). The fuzzy-valued material properties are Young's moduli $\tilde{E}_{11}$, $\tilde{E}_{11}$ and $\tilde{E}_{33}$, shear modulus $\tilde{G}_{13}$, Poisson's ratio $\tilde{\nu}_{12}$, $\tilde{\nu}_{13}$ and $\tilde{\nu}_{23}$. The density ρ and plate thickness H are considered as accurate in order to limit the complexity of problem. Their corresponding values are $\rho = 1600\,\text{kg/m}^3$ and H = 2.25 mm. Assuming a monotonous relation between the fuzzy-valued parameters and the fuzzy-valued outputs, i.e. the group velocities, the Reduced Transformation Method is used to propagate the uncertainty in the fuzzy-parameterized dynamic system. Thus, each fuzzy input parameter is divided in 3 equally spaced intervals (m = 3), which results in 4 membership levels μ_j. As a result of the decomposition, at each membership level, 32 parameter combinations are evaluated for every frequency. Since the material properties are not functions of frequency, they are considered independent variables in the fuzzy-parameterized models. To this end, the software FAMOUS (Fuzzy Arithmetical Modeling of Uncertain Systems) is used, which implements the Transformation Method as

	$a_i^{(0)}$	$\bar{p}_i$	$b_i^{(0)}$
$\tilde{E}_{11}$ [GPa]	48.8	51.4	54
$\tilde{E}_{33}$ [GPa]	12	12.6	13.3
$\tilde{G}_{13}$ [GPa]	4.6	4.8	5.1
$\tilde{\nu}_{12}$	0.31	0.33	0.35
$\tilde{\nu}_{13}$	0.27	0.28	0.29

(a) Transversely isotropic layer

	$a_i^{(0)}$	$\bar{p}_i$	$b_i^{(0)}$
$\tilde{E}_{11}$ [GPa]	127.1	133.8	140.5
$\tilde{E}_{22}$ [GPa]	9.9	10.4	10.9
$\tilde{G}_{13}$ [GPa]	4.56	4.8	5.04
$\tilde{\nu}_{12}$	0.31	0.33	0.35
$\tilde{\nu}_{23}$	0.44	0.46	0.48

(b) Unidirectional CFRP plate with x_2x_3 plane of isotropy

Table 4.1: Nominal values and worst-case intervals of linear fuzzy parameters

a pre- and post- processing tool.

In order to solve the dispersion equations, a root-finding algorithm based on a search in polar coordinates is used [93]. The main steps of the algorithm can be described as follows:

1. Find the initial root (wavenumber) of each propagating mode for a predetermined frequency by applying an interval search method to a range of wavenumbers, where the initial interval is the result of searching for sign changes in the complex characteristic equations.

2. Define a search area (radius and angle) for the next root in local, polar coordinates in the frequency-wavenumber plane, where the origin is the previous root.

3. Find the next root by applying an iterative interval search until a convergence criterion is met.

4. Repeat steps 2 and 3 for the entire frequency range.

4.3.1 Fuzzy simulations for a transversely isotropic single-layer

The results of the evaluation of the dispersion equation Eq. (2.17) with fuzzy-valued material properties are shown in Fig. 4.2b, where only the fundamental modes, S0 and A0, as well as the first higher-order mode A1 are presented. The conventional representation of the dispersion curves are lines, as shown in Fig. 4.2a. This is the result of evaluating the dispersion curve by using the nominal values of the material properties, which could be considered as a single combination of material parameters. In the case of the fuzzy-valued group velocity dispersion curves, the dispersion equation is evaluated by using special combinations of the material parameters, instead of a single combination. As a result, the group velocity for each mode at a specific frequency is not an unique value, but a set of possible velocities. This result explains why the dispersion curve for each mode appears as a bundle of curves instead of a single line. Furthermore, the color gradient in Fig. 4.2b represents different levels of the membership function μ, where the lowest level corresponds to $\mu^{(0)}$ at the worst-case intervals and the highest level indicates $\mu^{(3)}$ at the nominal values.

(a) Nominal dispersion curves

(b) Fuzzy-valued output for m = 3
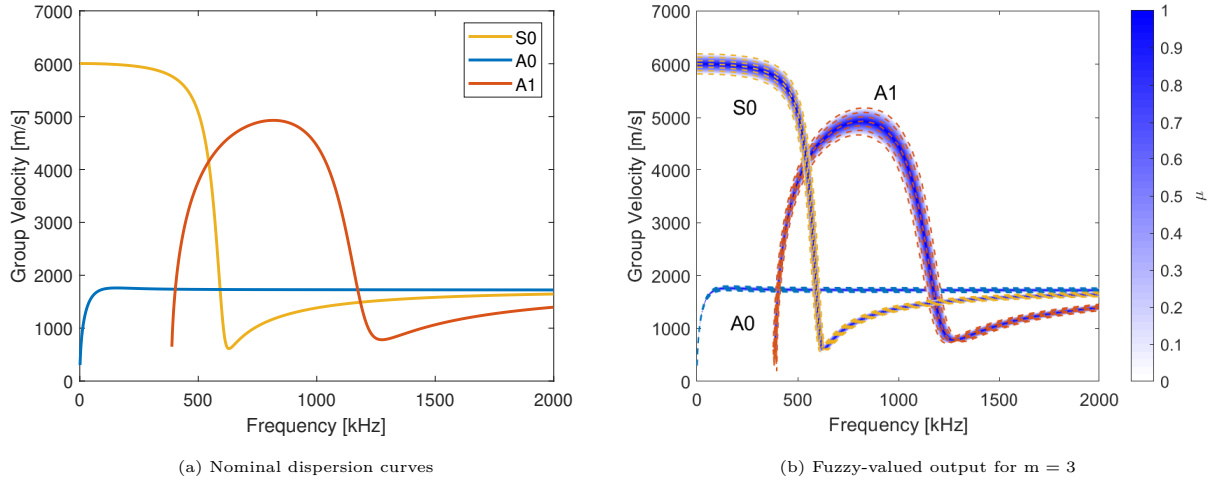
Figure 4.2: Group velocity dispersion curves in a quasi-isotropic CFRP plate

The fuzzy-valued group velocities at frequencies, 200kHz, 550kHz and 2MHz are extracted and shown in Fig. 4.3. It can be seen that the outputs are triangles without vertical flanks, which is an indicator of monotonic mapping between parameters and outputs. Similar inspections at different frequencies also did not present an indication of non-monotonic behavior. Furthermore, it is observed that the uncertainty in the velocities for each mode vary throughout frequency, where the fundamental mode, A0, exhibits the smaller uncertainty variation among the three modes. In contrast, the velocity of the mode S0 shows a large variation, especially in the highly dispersive zone between $450\,\text{kHz}$ and $650\,\text{kHz}$. As an example of the large variation in this zone, the velocity's uncertainty of mode S0 is compared to the uncertainty for mode A0 in Fig. 4.3b, where the highest uncertainty of the mode S0 at 550kHz is around 20 times lager than mode A0's uncertainty. As the mode S0 approaches to Rayleigh wave velocity, its velocity's uncertainty decreases to the mode A0's uncertainty level as Fig. 4.3c shows. From this figure, it can also be seen that the velocity's uncertainty at high frequencies is less than 90 m/s. Similar to mode S0, the uncertainty in group velocities of mode A1 is higher in highly dispersive regions and is lower at high frequencies.

The relative measure of influence ω_{ik} of the material parameters on the fuzzy-valued group velocities is shown in Fig. 4.4 for the modes S0, A0 and A1. This measurement

(a) A0 and S0 modes at 200 kHz   (b) A0 and S0 modes at 550 kHz   (c) A0, S0 and A1 modes at 2 MHz
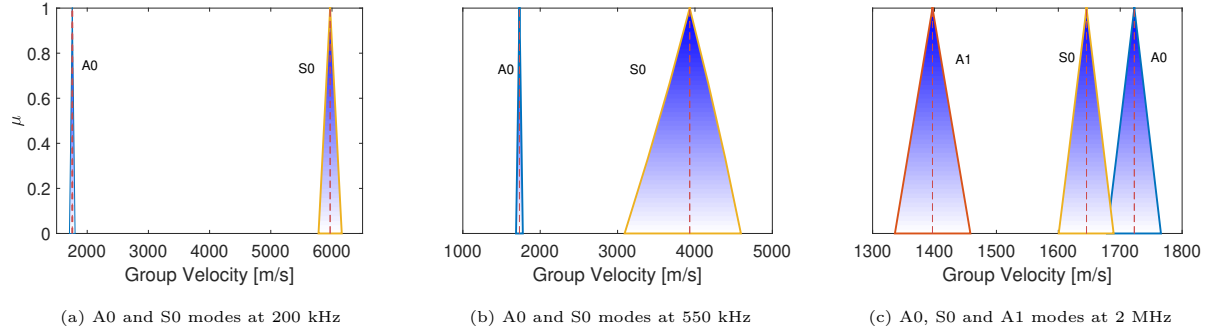
Figure 4.3: Fuzzy-valued group velocities for the modes A0, S0 and A1 at selected frequencies for a quasi-isotropic CFRP plate

indicates that the influence of the fuzzy-valued material properties is not equally weighted for the three modes, and strongly dependent on frequency. Fig. 4.4a shows that the group velocity of mode A0 is to a major part only affected by the shear modulus $\tilde{G}_{13}$ in frequencies above 160kHz, where the mode becomes less dispersive. It is observed in this figure that the Young's modulus $\tilde{E}_1$ vanishes completely at 160kHz and 400kHz. Different from the mode A0, the material parameters' influence on the velocity for modes S0 and A1 continuously changes throughout frequency as shown in Fig. 4.4b and Fig. 4.4c, respectively. As an example of these variations, for the velocities of mode S0, the Young's modulus $\tilde{E}_1$ goes from having 80% influence at low frequencies to having no influence at 1500kHz. Similar to $\tilde{E}_1$, the influence of $\tilde{E}_3$ drops to around 10% at 2MHz from 90% at 600kHz, which is considered a highly dispersive region. In the highly dispersive region it is also observed that the influence of the Poisson's ratio $\tilde{\nu}_{12}$ vanishes above 500kHz, while $\tilde{G}_{13}$ does not have any substantial effect on the velocity below 600kHz.

4.3.2 Fuzzy simulations for a unidirectional CFRP plate

The fuzzy-valued group velocity dispersion curves obtained from Eqs. (2.18) and (2.18) for the fundamental modes A0 and S0 for selected wave propagation angles θ are depicted in Fig. 4.5 for a unidirectional CFRP plate (0° fiber orientation). Note that some results are

(a) A0 mode   (b) S0 mode   (c) A1 mode

Figure 4.4: Relative Measure of influence ω_{ik} of fuzzy-valued parameters on the group velocities for the modes A0, S0 and A1 for a quasi-isotropic CFRP plate

(a) Mode A0   (b) Mode S0
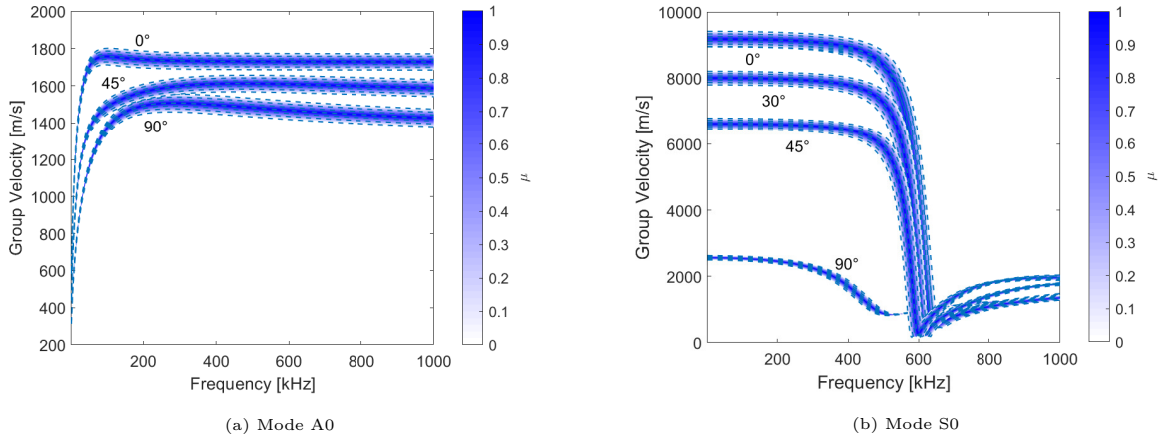
Figure 4.5: Fuzzy-valued group velocity dispersion curves for the fundamental modes A0 and S0 in an unidirectional CFRP plate for m = 3 and selected wave propagation angles θ

omitted for the sake of clarity. It is well known that in unidirectional CFRP plates, waves travel at higher velocities in the direction of the fibers and the waves' velocities decrease as the angle θ increases, as can be seen in the figure. In Fig. 4.5b, it can also be observed that in addition to a reduction of the wave propagation velocity, an increase in the wave propagation angle also reduces the group velocity's uncertainty for mode S0 at frequencies below 600kHz.

The relative measure of influence ω_{ik} of fuzzy-valued parameters on the group velocities

49

(a) Wave propagation along $\theta = 0°$ (b) Wave propagation along $\theta = 45°$ (c) Wave propagation along $\theta = 90°$
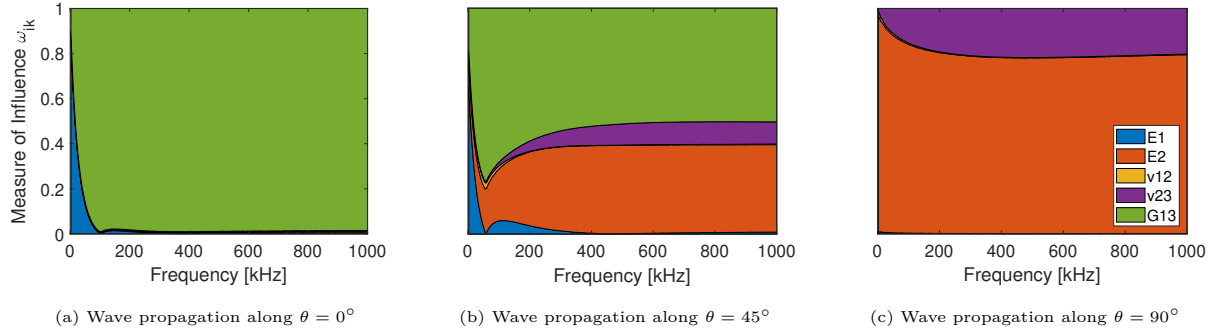
Figure 4.6: Relative measure of influence ω_{ik} of fuzzy-valued parameters on the group velocities for the mode A0 for an unidirectional CFRP plate

for the mode A0 is shown in Fig. 4.6. A comparison of the parameters' influence at different angles θ shows that uncertainty of the shear modulus $\tilde{G}_{13}$ loses influence in the calculation of the velocities as θ increases, while the parameters Young's modulus $\tilde{E}_{22}$ and Poisson's ratio $\tilde{\nu}_{13}$ gain importance in the calculation. Moreover, only the uncertainties of the parameters $\tilde{E}_{22}$ and Poisson's ratio $\tilde{\nu}_{23}$ are involved in ω_{ik} at 90° as shown in Fig. 4.6c. In addition, the cases in Fig. 4.6 reveal that the influence of the parameter of Poisson's ratio $\tilde{\nu}_{12}$ is negligible to the velocities for all frequencies and angles, except for around $160\,\text{kHz}$ at $\theta = 60°$.

Fig. 4.7 shows the relative measure of influence ω_{ik} of fuzzy-valued parameters on the group velocities for the mode S0 at different angles θ. In this figure, an increasing influence of the Poisson's ratio $\tilde{\nu}_{23}$ in ω_{ik} is observed. Poisson's ratio $\tilde{\nu}_{23}$ ends affecting the group velocities at low frequencies as shown in Fig. 4.7c. However, the highest influence is still from Young's modulus $\tilde{E}_{22}$ with more than 80% for most of the frequencies. Another observation in Fig. 4.7 is the variation of the influence of $\tilde{G}_{13}$. At $\theta = 0°$ (see Fig. 4.7a), its influence is limited to frequencies above 600kHz. In figure Fig. 4.7b, $\tilde{G}_{13}$ starts affecting the velocities at low frequencies. However, at 90°, the influence of $\tilde{G}_{13}$ vanishes completely (see Fig. 4.7c).

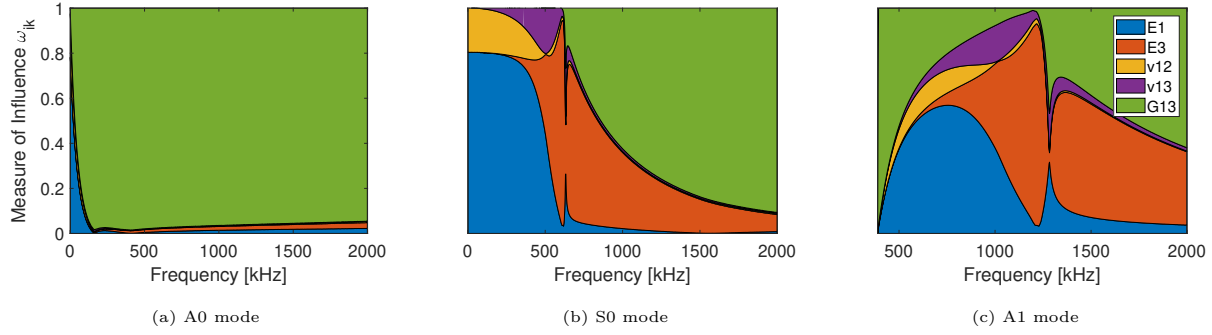(a) Wave propagation along $\theta = 0°$ (b) Wave propagation along $\theta = 45°$ (c) Wave propagation along $\theta = 90°$
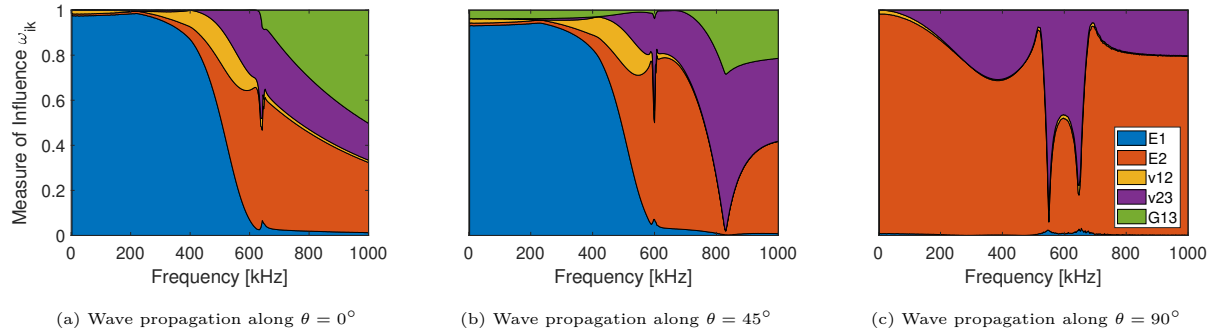
Figure 4.7: Relative measure of influence ω_{ik} of fuzzy-valued parameters on the group velocities for the mode S0 for an unidirectional CFRP plate

4.4 Material Characterization of Composites

In this section, the material characterization of a quasi-isotropic CFRP plate is carried out using the the inverse fuzzy arithmetic approach presented in Section 4.2. In the first result, two sets of identified parameters are obtained from individual analyses of the S0 and A0 modes. In the second result, both modes are used during the inversion procedure to identify the parameters. For the first approach, the measured and calculated group velocities of the S0 mode in the frequency range between 120 kHz and 300 kHz are used to identify the first set of parameters. To obtain the second set, the velocities of the mode A0 in the frequency range between 40 kHz and 180 kHz are utilized. In the second approach, the parameter identification is based on the measured and calculated group velocities only in the frequency range between 120 kHz and 180 kHz to include both modes during the identification procedure (couple analysis).

4.4.1 Dispersion data from laboratory experiments

The specimen used in this study is an aerospace-grade quasi-isotropic CFRP laminate of thickness 2.089 mm and dimension 860 x 860 mm². The plate is comprised of eight woven plies (plain weave, density $\rho = 1463 \, \text{kg/m}^3$) made from Hexcel AS4 carbon fiber pre–impregnated with the Newport 301 epoxy resin system, and cured in an autoclave with
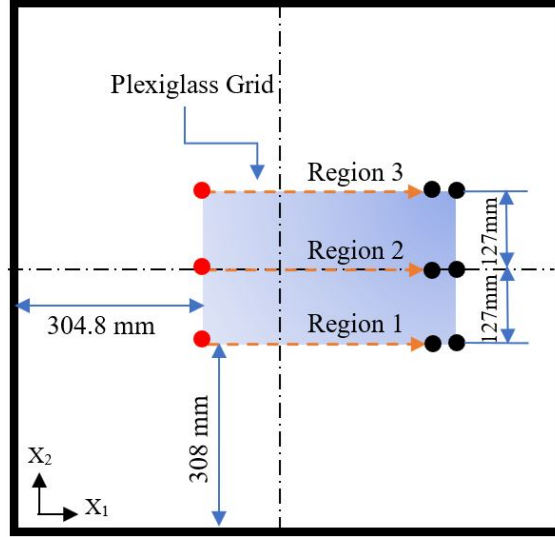
Figure 4.8: Positions of actuator (red) and receiver (black) transducers in a composite plate.

a stacking sequence of $[0, 45, -45, 90]_\mathrm{s}$. Three regions on the smooth face of the CFRP are selected to measure the group velocities along the x_1-direction ($0°$), as shown in the Fig. 4.8. The three regions are $127\,\mathrm{mm}$ ($5\,\mathrm{in}$) away from each other in the x_2-direction. A pair of broadband transducers (Digital-Wave B225) with a relatively flat frequency response from $50 - 400\,\mathrm{kHz}$ are used for the experiments in a pitch-catch mode [86, 65, 79], where one acts as an actuator (red) and the other as the roving sensor (black). Precise and repeatable measurements are accomplished through using a CNC machined Plexiglass grid ($330\,\mathrm{mm} \times 250\,\mathrm{mm}$, machining tolerance of $\pm 0.02\,\mathrm{mm}$) to accurately position the transducers on the plate. An ultrasound couplant (Sonotech) is used to improve the transmission of energy between the transducers and the specimen. A function generator (NI PXI-5402) is used to generate the ultrasonic signals, which are then amplified by a Ritec A3000 voltage amplifier. The measurement signals are boosted by a Digital Wave FM-1 signal conditioner before being digitized by an oscilloscope (Agilent 54624A). To further improve the signal-to-noise ratio (SNR), the average of 32 repeated measurements is recorded.

In order to determine the group velocities, the signals are recorded at $304.8\,\mathrm{mm}$ ($12\,\mathrm{in}$) and $330.2\,\mathrm{mm}$ ($13\,\mathrm{in}$) away from the source within each region. The narrow-banded waves are excited in the frequency range between $30\,\mathrm{kHz}$ and $300\,\mathrm{kHz}$. The short-time Fourier

transform (STFT) is used to evaluate the time-of-flight (TOF) of the dispersive signals [24, 38]. To minimize any random experimental errors, four independent readings are taken and averaged for each measurement location, and velocities are calculated based on the differences in arrival times of waves at the sensing locations by using the same transducer rather than taking the TOF between the excited and the arrived waves. Thus, the uncertainty introduced by the response of each transducer is (nearly) eliminated from the calculation of the velocities. Therefore, the majority of the random experimental errors can be attributed to varying amounts of couplant and applied pressure. Since the signal strength of the A0 and S0 waves cannot be considered equal throughout the entire studied frequency range [76], the A0 mode is only studied in the frequency range $40 - 180\,\text{kHz}$ and the S0 mode at $120 - 300\,\text{kHz}$. Thus, signals with poor SNR have been omitted from the analysis. Fig. 4.9 shows the determined group velocities with error bars for both the S0 and A0 modes. It should be noted that the former has a high signal-to-noise ratio (SNR) between $110\,\text{kHz}$ and $210\,\text{kHz}$, and the latter for $30\,\text{kHz}$ and $90\,\text{kHz}$ for region 3. As can be seen from Figs. 4.9a to 4.9c, measured group velocities include aleatory uncertainty within each region and epistemic uncertainty across the three regions for the S0 mode. The mode A0 velocities' variation is smaller but not negligible, as can be seen from Figs. 4.9d to 4.9f.

The data from each region and mode is averaged to reduce the random error in the experimental data. The corresponding mean values for each region are shown in Fig. 4.10. As can be seen from the figures, despite this averaging over the four trials in each region, a substantial uncertainty remains. The largest uncertainty in the velocities for both modes occurs in the frequency range between $110\,\text{kHz}$ and $210\,\text{kHz}$. For the symmetric mode, the difference in velocity can be as much as $400\,\text{m/s}$ at $200\,\text{kHz}$, as shown in Fig. 4.10a. It should be noted that this discrepancy exists despite the small spatial distance between regions 1 and 3 of only $254\,\text{mm}$ ($10\,\text{in}$), and careful monitoring of the manufacturing process. This difference is about 10 times larger than the maximum variation in the group velocity of the mode A0 that occurs at $150\,\text{kHz}$, as shown in Fig. 4.10b. Since for any given frequency, the group velocities vary between the regions, the experimental data are best represented by
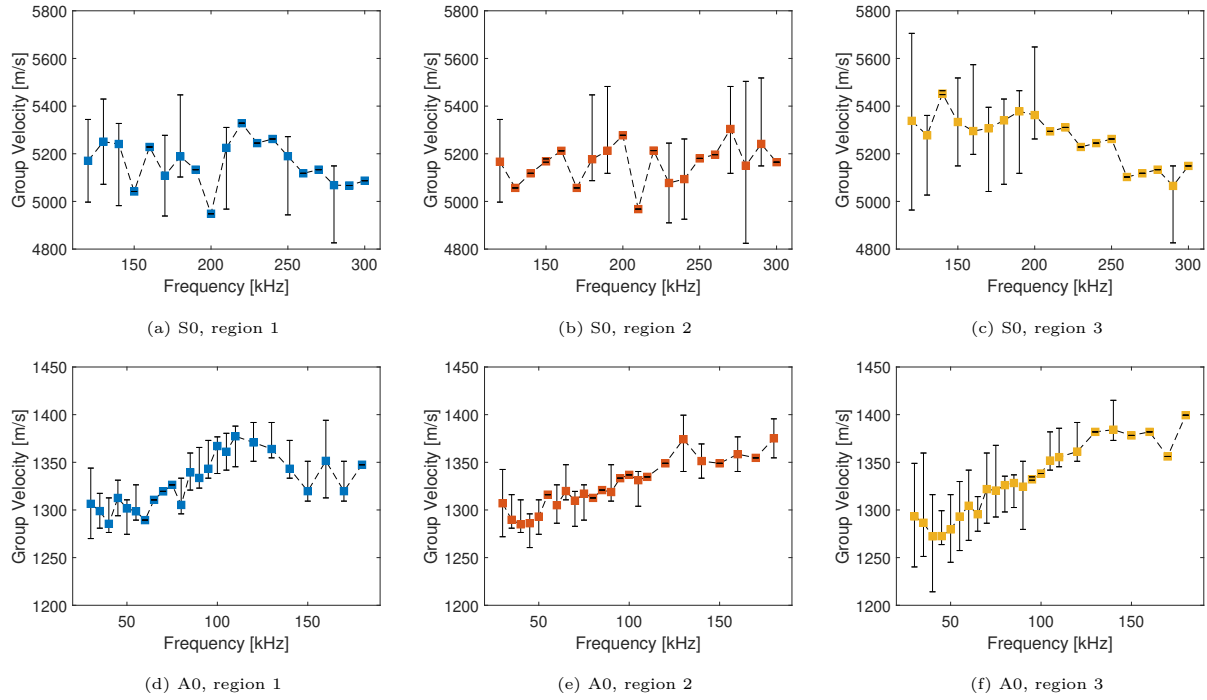
Figure 4.9: Experimentally determined group velocities for the S0 and A0 modes in three different regions of a quasi-isotropic CFRP plate
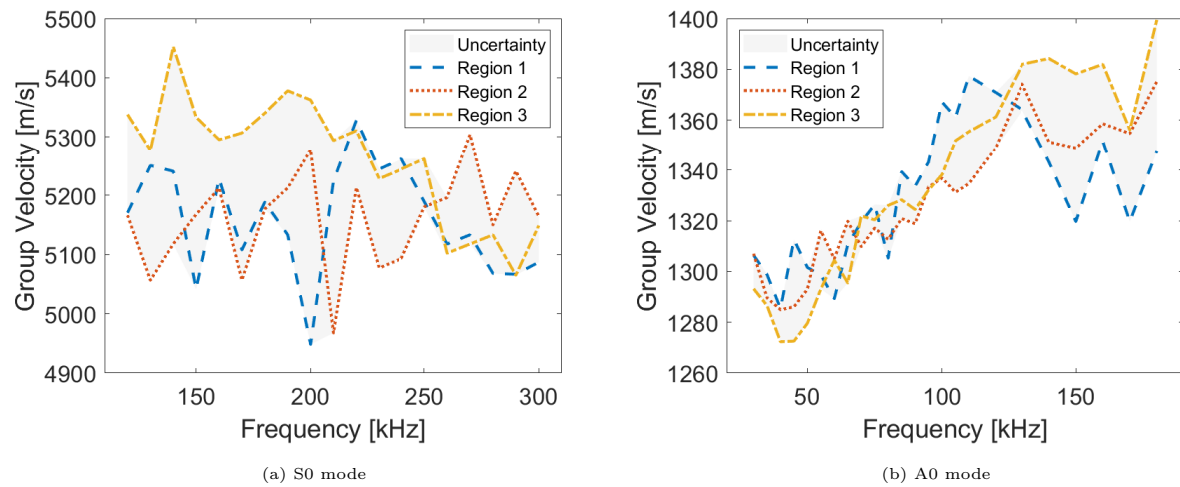
Figure 4.10: Uncertainty in experimentally determined group velocities based on measurements in different regions of a quasi-isotropic CFRP plate

fuzzy numbers due to the assumed epistemic nature of the uncertainty. Thus, the dispersion models should be based on fuzzy-valued parameters whose uncertainty would ideally be

54

identified based on the measured data, as discussed in Section 4.4.4.

4.4.2 Material model

For a quasi-isotropic CFRP plate, classical lamination theory is used to represent the laminate as a transversely isotropic, homogenized, single-layer model with the symmetry axis about the off-plane axis (here: x_3-axis). Assuming a quasi-isotropic composite plate model, the transversely isotropic stiffness constants C_{ij} [33] are fuzzyfied by defining the following material properties as linear fuzzy parameters: Young's moduli $\tilde{E}_{11}$ and $\tilde{E}_{33}$, shear modulus $\tilde{G}_{13}$, and Poisson's ratios $\tilde{\nu}_{12}$ and $\tilde{\nu}_{13}$. The density ρ and plate thickness H are considered as accurate in order to limit the complexity of the problem. A decomposition number of m = 3 is chosen, thus creating four membership levels μ_j for each fuzzy input parameter. As a result of the decomposition, 128 parameter combinations need to be evaluated for every frequency at the first three membership levels in addition to the nominal value case. Since the material properties are not functions of frequency, they can be considered independent variables of the fuzzy model.

In order to determine the nominal parameter values, this study utilizes Maxwell's methodology [51, 50] in conjunction with CLT [33]. Maxwell's methodology applied to composites allows for estimating the effective material properties of transversely isotropic, unidirectional laminae from the properties of the fibers and the matrix system. CLT is then used to obtain the material properties for the woven laminae. Finally, the nominal values for the transversely isotropic single-layer homogenized model (see Section 4.4.2) are the effective material properties of the full laminate, which are also obtained by means of CLT.

The worst-case intervals may be initially chosen in an attempt to allow the fuzzy output from the simulation to cover the experimental data. Another consideration in the selection of the worst-case intervals is that the input sets in the forward fuzzy simulation are physically consistent within the framework of the mathematical elasticity model[33]. For this study, the second avenue is chosen and the nominal values and initially guessed worst-case intervals of the material properties are given in (Table 4.2a). In the case that a particular set of

material properties is not physically possible, it is reported and excluded from the fuzzy analysis. Thus, these reported sets are not used in the calculation of the gain factors during the forward simulation, and subsequent parameters identification procedure.

To prevent that the difference in magnitude between the input parameters affects the inversion procedure, their values are input in the units of GPa [5].

4.4.3 Forward fuzzy arithmetic

In order to create the linear mapping between the input material parameters and the output group velocities, the worst-case deviations in the parameters are implemented based on the values from Table 4.2a. The results of the evaluation of the dispersion equation Eq. (2.17) with the fuzzy-valued material properties are shown in Fig. 4.11a and Fig. 4.11b for the S0 and A0 modes, respectively. As can be seen from Fig. 4.11a, the S0 mode is nearly non-dispersive in this frequency range with a practically constant uncertainty in the velocity of approximately $400\,\mathrm{m/s}$. In contrast, the uncertainty of the A0 mode considerably varies due to the highly dispersive behavior of the mode's velocity for frequencies below $100\,\mathrm{kHz}$, where the the uncertainty at $100\,\mathrm{kHz}$ is $25\,\%$ higher than the one at $40\,\mathrm{kHz}$. In the the frequency range between $100\,\mathrm{kHz}$ and $180\,\mathrm{kHz}$, the A0 mode's velocity remains nearly constant, re-

	$a_i^{(0)}$	$\bar{p}_i$	$b_i^{(0)}$
$\tilde{E}_{11}$ [GPa]	45.16	47.54	49.92
$\tilde{E}_{33}$ [GPa]	7.95	8.37	8.79
$\tilde{G}_{13}$ [GPa]	2.71	2.85	2.99
$\tilde{\nu}_{12}$	0.306	0.322	0.339
$\tilde{\nu}_{13}$	0.273	0.288	0.302

(a) Nominal values $\bar{p}_i$ and assumed worst-case intervals $[a_i^{(0)}, b_i^{(0)}]$ of linear fuzzy parameters

	Lower bound	Upper bound
$\tilde{E}_{11}$ [GPa]	0	free
$\tilde{E}_{33}$ [GPa]	0	free
$\tilde{G}_{13}$ [GPa]	0	free
$\tilde{\nu}_{12}$	-1	1
$\tilde{\nu}_{13}$	free	free

(b) Constraints for inverse fuzzy arithmetic

Table 4.2: Fuzzified material properties for forward simulation and constraints for model inversion

(a) S0 mode

(b) A0 mode

(c) S0 mode

(d) A0 mode
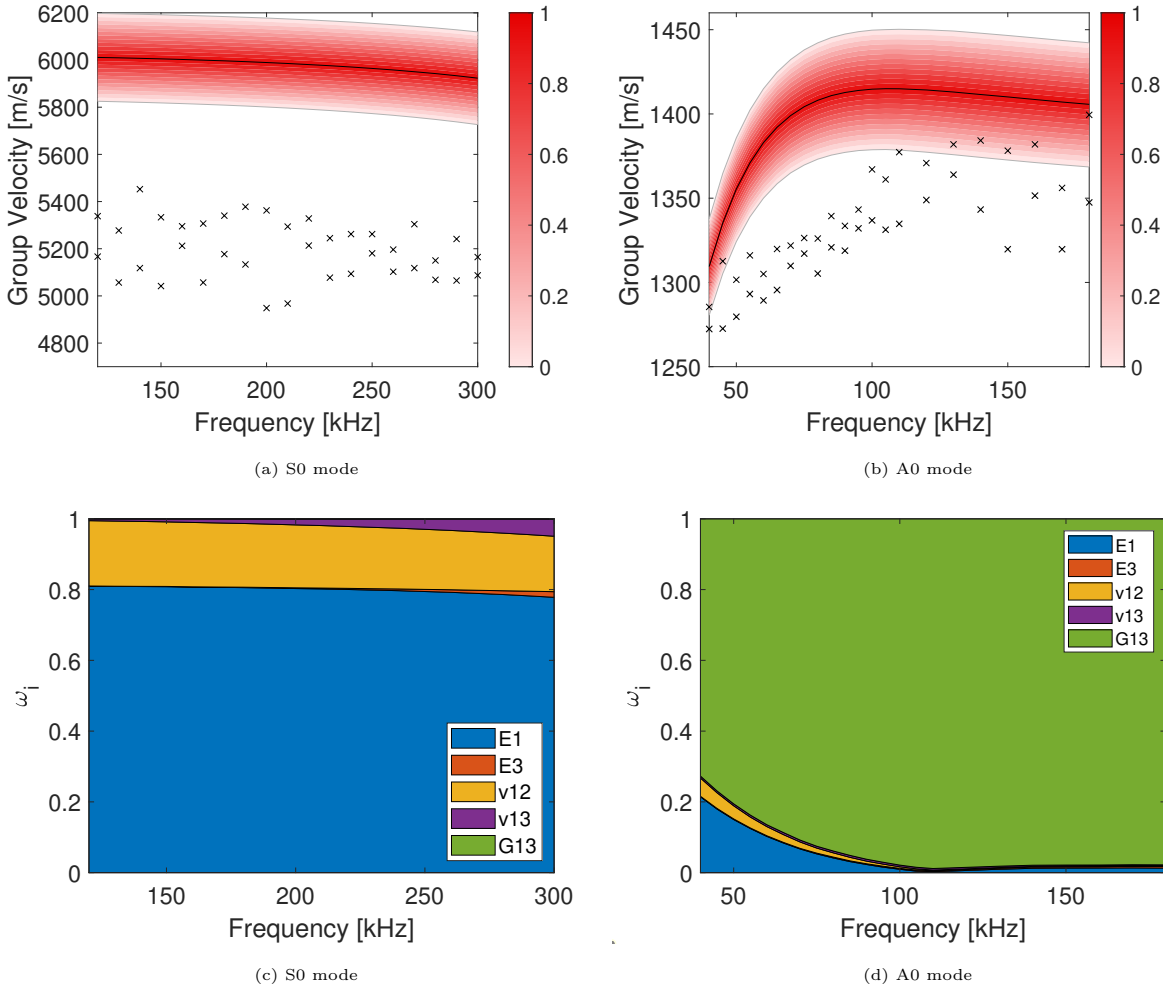
Figure 4.11: Forward fuzzy analysis outputs for m = 3, including relative measure of influence ω_{ik} of fuzzy-valued parameters on the group velocities. Experimental lower and upper bounds are marked by ×

sulting in a nearly constant uncertainty of approximately 70 m/s, as shown in Fig. 4.11b. It should also be noted that the predicted uncertain group velocities do not enclose the measured values, shown as ×, for neither of the two modes. In addition, all the measured values are below the nominal value of the velocity for both modes. However, despite the difference between the measured velocities and the model's output in Fig. 4.11a and Fig. 4.11b, some characteristics prevail in both cases. As can be seen from the forward simulation, the influence of the material parameter uncertainty on the uncertainty of the group velocity of the

S0 wave is significantly higher as compared to the A0 wave in the frequency range between 120 kHz and 180 kHz. However, the uncertainty does not exceed $\sim 7\,\%$ of the nominal value in neither case. In addition, the uncertainty in the velocity appears to be increasing with frequency for the A0 mode. Therefore, by taking in consideration the matching trends between simulation and experimentation, one can infer that the substantial variation in the uncertainty of the measured velocities is mostly the result of the variation of the material properties instead of random experimental errors.

Although it is not shown in Fig. 4.11b, the measured velocities at 30 kHz and 35 kHz are the only values which are above the nominal value of the velocities. To prevent that these outliers affect the parameter identification, they have been excluded from the inverse procedure.

To analyze the influence of the material parameters on the fuzzy-valued group velocities, the relative measurement of influence, ω_{ik} is calculated [25, 20]. This measurement of influence normalizes the contribution of the uncertainty of each material parameter in the overall uncertainty of the group velocities at each frequency. The relative measures of influence ω_{ik} are shown in Fig. 4.11c and Fig. 4.11d for the S0 and A0 modes, respectively. As can be seen from the figures, the influence of the fuzzy-valued material properties is not equally weighted for both modes, and mostly constant on this frequency range. Fig. 4.11d shows that the group velocity of the A0 mode is to a large extent only affected by the shear modulus $\tilde{G}_{13}$ by 98 % for frequencies between 100 kHz and 180 kHz. In the range of frequencies between 40 kHz and 100 kHz the influence of the the Young's modulus $\tilde{E}_1$ starts at 21 % and decreases as the frequency approaches to 100 kHz. Similar to $\tilde{E}_1$, the influence of the Poisson's ratio $\tilde{\nu}_{12}$ in the velocities decreases in this frequency range. Starting with 6 % at 40 kHz, $\tilde{\nu}_{12}$'s influence reduces to practically none influence in the velocity in the frequency range between 100 kHz and 180 kHz. Different from A0 mode, $\tilde{G}_{13}$ does not have any substantial effect on the S0 mode's velocity, as shown in Fig. 4.11c. Instead, the main contributors are the Young's modulus $\tilde{E}_1$ and Poisson's ratio $\tilde{\nu}_{12}$, making up approximately 80 % and 19 % of the overall uncertainty, respectively, and mostly constant on the frequency range between

<table>
<tr><td>(a) S0 mode</td><td>(b) A0 mode</td></tr>
</table>
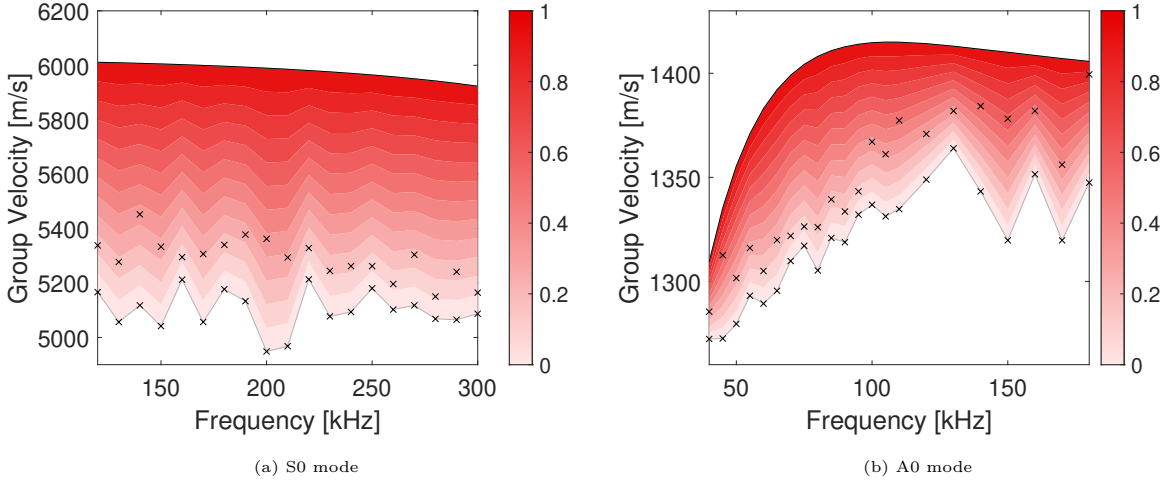
Figure 4.12: Fuzzyfied group velocities based on measured data and nominal values of forward simulation. Experimental lower and upper bounds are marked by ×

120 kHz and 180 kHz. As the frequency increases, the influence of the Poisson's ratio $\tilde{\nu}_{13}$ becomes more notorious with nearly 5 % influence in the velocity at 300 kHz.

4.4.4 Inverse fuzzy arithmetic

By taking the nominal values of the output from the forward simulation and the uncertainties in the measured group velocities, fuzzyfied group velocities are now built at each frequency as the input for the optimization process. The "new" fuzzyfied group velocities are shown in Fig. 4.12. From these plots, it can again be seen that the nominal values are outside the area of uncertainty created by the measured velocities for all frequencies and modes. Furthermore, the velocity of the S0 mode has larger deviations (approx. 1000 m/s) as compared to the A0 mode (less than 100 m/s). Thus, it can be noted that either the material parameters and/or underlaying dispersion model do not match with the experimental data. Hence, a re-identification of the nominal values is attempted through inverse fuzzy arithmetic.

In the inverse method, the optimization problem is constraint such that certain material property combinations are excluded from the fuzzy inverse analysis as they would be infeasible. A summary of the constraints is given in Table 4.2b. These constraints follow

Figure 4.13: Initially guessed (blue dashed) and identified (red solid) fuzzy–valued material parameters for m = 3 based on S0 mode analysis.
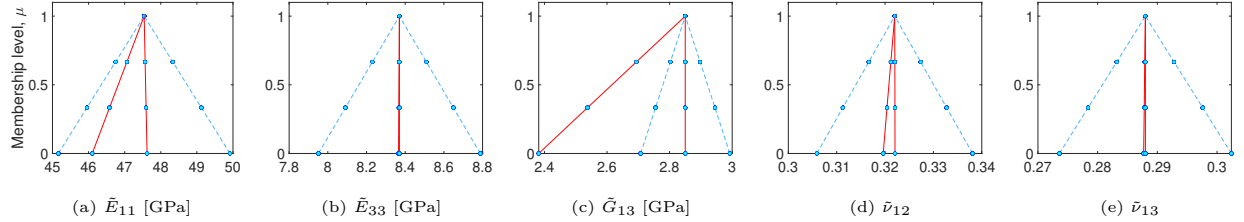
Figure 4.14: Initially guessed (blue dashed) and identified (red solid) fuzzy–valued material parameters for m = 3 based on A0 mode analysis.

the energy strain considerations as defined by Jones [33]. That is, the lower bounds of the Young's moduli and shear modulus are set such that only combinations with positive values are permitted. The lower and upper bounds for the Poisson's ratio $\tilde{\nu}_{12}$ are set to -1 and $+1$ due to fact that the transverse isotropy assumption enforces $E_{11} = E_{22}$. While there are physical constraints on $\tilde{\nu}_{13}$, they cannot be incorporated into the optimization problem as they depend on the (to be determined) values of $\tilde{E}_{11}$ and $\tilde{E}_{33}$. Instead, unphysical cases of $\tilde{\nu}_{13}$ are excluded in post-processing step.

Considering the aforementioned constraints, the inverse fuzzy procedure is applied for the individual mode approach, and the results are presented in Fig. 4.13 and Fig. 4.14, where the initially guessed and identified parameters with their respective uncertainty are shown as blue dashed and red lines, respectively.

The figures show that the uncertainty for most of the found material parameters is represented by triangles to the left, it is because the measured group velocities are below the nominal values of the calculated velocities. Moreover, $\tilde{E}_{11}$ (S0 mode analysis) and $\tilde{G}_{13}$ (A0

60

(a) Approach 1: S0 mode.

(b) Approach 1: A0 mode

(c) Approach 2: S0 mode

(d) Approach 2: A0 mode
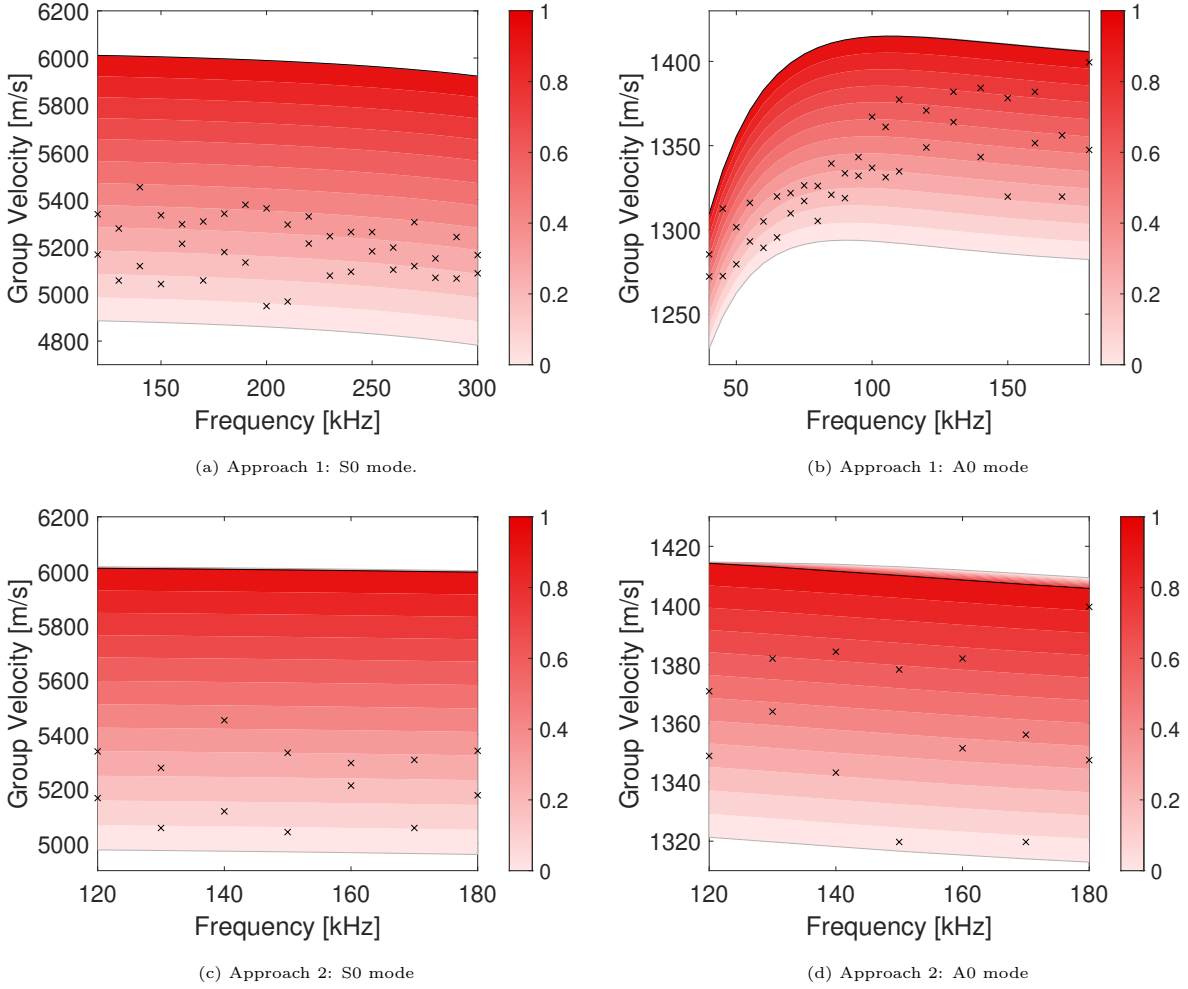
Figure 4.15: Fuzzy–value group velocities using identified material parameters for m = 3. Experimental data is marked by ×

mode analysis) exhibit higher uncertainty than the initially guessed ones, as depicted in Figs. 4.13a and 4.14e, respectively. However, none uncertainty is identified for the parameters $\tilde{G}_{13}$ (Fig. 4.13c) in the S0 mode analysis, and $\tilde{E}_{33}$ (Fig. 4.14b) and $\tilde{\nu}_{13}$ (Fig. 4.14e) in the A0 mode analysis. These results appear consistent with the results from the sensitivity analysis, where the most influential parameters in the calculation of the group velocities are $\tilde{E}_{11}$ and $\tilde{\nu}_{12}$ for the velocity of S0 mode, and $\tilde{G}_{13}$ and $\tilde{E}_{11}$ for A0 mode's velocity. The resimulation with the identified parameters from the individual mode analysis are presented in Figs. 4.15a and 4.15b

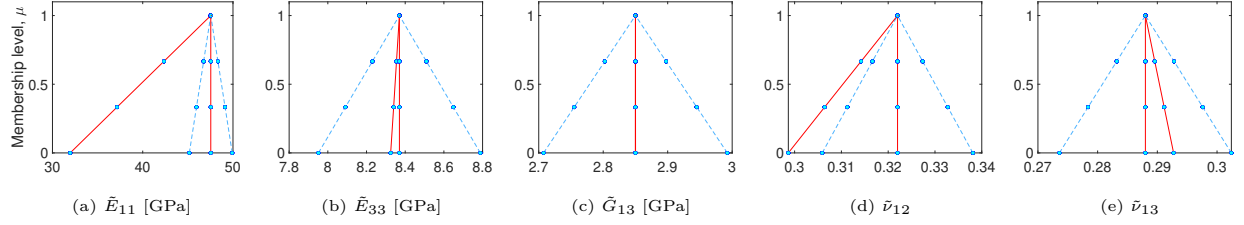(a) $\tilde{E}_{11}$ [GPa] (b) $\tilde{E}_{33}$ [GPa] (c) $\tilde{G}_{13}$ [GPa] (d) $\tilde{\nu}_{12}$ (e) $\tilde{\nu}_{13}$
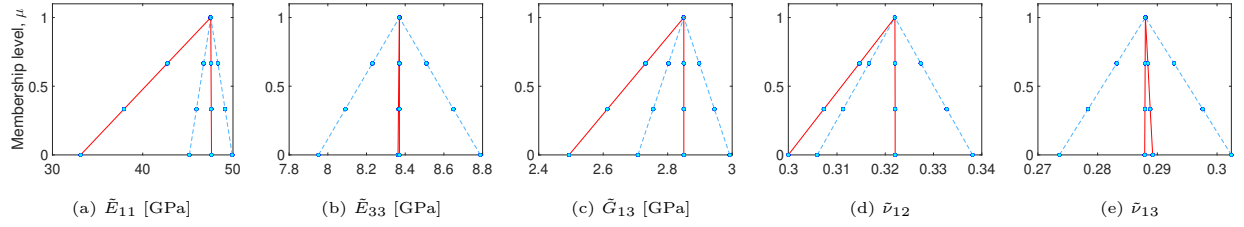
Figure 4.16: Initially guessed (blue dashed) and identified (red solid) fuzzy–valued material parameters for m = 3. Couple mode analysis

For both modes, a relatively close match with the measured data is achieved in a conservative manner as desired with $\gamma = 1$ for the inverse procedure. As depicted in Fig. 4.15a, the lower bound of the uncertainty interval extends approximately $88\,\mathrm{m/s}$ below the lowest measured velocity at $200\,\mathrm{kHz}$ for the S0 mode. Similarly, for the A0 mode, it is observed that the extension of the lower bound of the uncertainty is roughly $8\,\mathrm{m/s}$ at $60\,\mathrm{kHz}$, as shown in Fig. 4.15b.

Considering each mode separately during the inverse procedure has resulted in two sets of identified parameters, which need to be consolidated in a single set capable to represent the material and its modal velocities. One option could be selecting the most dominant identified parameters from the two sets, e.g. $\tilde{E}_{11}$ from the S0 mode analysis, to represent the material property. An alternative approach to obtain a single set of material parameters is simultaneously including both modes during the inversion procedure. Although in this particular case, based on the sensitivity analysis, the most influential parameters obtained from the S0 mode analysis have practically not influence in the velocity of A0 mode and vice versa, it cannot be generalized to other cases. In addition, since for the overall frequency rage between $40\,\mathrm{m/s}$ and $300\,\mathrm{m/s}$ two modes of wave propagation are present, it is expected that both modes are considered during the inversion procedure. Thus, the second strategy is chosen to identify a single set of material parameters. The single set of identified parameters from the couple mode analysis are presented in Fig. 4.16 and the corresponding re-simulations in Figs. 4.15c and 4.15d

The newly identified parameters show that the dominant parameters in Figs. 4.13 and 4.14

prevails, with a slightly reduction of $\tilde{G}_{13}$ ' uncertainty with respect to the one in Fig. 4.14c. Similar to the previous approach, one more time, the re-simulations of both modes result in a good agreement with the measured data. The re-simulation of the S0 mode in Fig. 4.15c presents an expansion of the lower bound of the uncertainty from the measured velocity of nearly $73\,\mathrm{m/s}$ at $150\,\mathrm{kHz}$, which is practically the same deviation presented in the individual mode analysis (see Fig. 4.15a). However, for the A0 mode, it is observed that the upper bound of the uncertainty additionally extends above the nominal curve, as shown in Fig. 4.15d. Thus, this could be a manifestation of the large uncertainty introduced by $\tilde{E}_{11}$ in the re-simulation of the A0 mode.

4.4.5 Defuzzyfication of Identified Material Parameters

In an effort to identify new nominal material properties, the identified parameters are de-fuzzyfied. Since all of the identified parameters are represented by single-sided triangles, the mean value of each parameter's worst-case interval is calculated for the individual and couple analyzes (see Table 4.3).

Based on these values, the group velocities are calculated and the results are shown as red dashed dotted and magenta dotted lines in Fig. 4.17 for the individual and couple mode analyses, respectively. It should be noticed that the original frequency range, $120\,\mathrm{kHz}$ to $180\,\mathrm{kHz}$, of the calculated velocity from the couple mode analysis has been extended to a larger frequency range for both modes. For the sake of comparison, the results from originally

	$\tilde{E}_{11}$ [GPa]	$\tilde{E}_{33}$ [GPa]	$\tilde{G}_{13}$ [GPa]	$\tilde{\nu}_{12}$	$\tilde{\nu}_{13}$
$\bar{p}_i$ (Couple Analysis)	37.92	8.37	2.61	0.307	0.289
$\bar{p}_i$ (S0 mode Analysis)	37.15	8.34	2.85	0.306	0.291
$\bar{p}_i$ (A0 mode Analysis)	46.58	8.37	2.54	0.3204	0.289

Table 4.3: Defuzzyfied values of linear fuzzy parameters identified through individual and couple mode analyses of the applied inverse fuzzy arithmetic

|(a) S0 mode | (b) A0 mode |
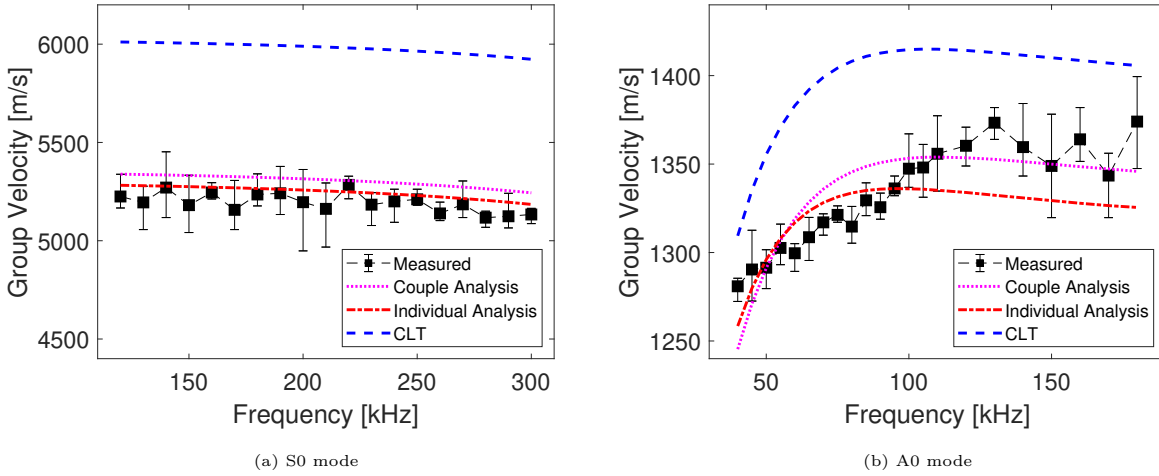
Figure 4.17: Group velocities using new nominal values obtained from defuzzyfied identified parameters based on couple (magenta dotted) and individual (red dashed dotted) analyses. Group velocities using nominal values obtained through CLT (blue dashed). Uncertainty in experimental data is marked with error bars

determined nominal values through CLT of the chosen material model from Section 4.4.2, are shown as blue dashed lines.

It can be seen that the fuzzy arithmetical evaluation leads to material properties consistent with the measured data in both analyzes. In the frequency range between 120 kHz and 180 kHz, Fig. 4.17b shows that the velocity from the couple mode analysis has the best fit to the uncertain region created by the measured velocities. This result has a direct relation with the identified parameter $\tilde{E}_{11}$, whose identified uncertainty is dominated by its effect in the velocity of the S0 mode. Although $\tilde{E}_{11}$'s influence in the velocity of the A0 mode is less than 2 % in this frequency range, the identified parameter has a significant impact in the velocity of the mode. The difference in the velocity between the two analyses is about 20 m/s. Another observation is that the extension of the calculated velocity from the couple analysis is a descent curve fitting of the measured data for both modes. In the case of the S0 mode, Fig. 4.17a shows an almost constant difference in the velocity between the couple and individual analyses of about 57 m/s, while this difference, smaller than 20 m/s, varies for the A0 mode as depicted in Fig. 4.17b. These results demonstrate the capabilities of the inver-

64

sion method, since the method with data from only seven frequencies in the frequency range between 120 kHz and 180 kHz has identified material parameters to represent the velocities in a larger frequency band.

In an attempt to measure the differences between the velocities from the nominal values (new and original) and the measured data, the root mean square deviation (RMSD) in units of **m/s** is proposed. The RMSD values in Table 4.4 confirm that the new set of nominal values adequately represent the material properties of the laminate, considering inherent epistemic uncertainty. A normalized RMSD has also been calculated and included in the table. To normalized the RMSD values, the mean value of the measured velocities from each mode is used and the normalized value is shown in percentage.

	RMSD	NRMSD
Couple Analysis	115	2.2 %
Individual Analysis	63	1.2 %
CLT	786	15.1 %

(a) S0 mode

	RMSD	NRMSD
Couple Analysis	18	1.4 %
Individual Analysis	21	1.6 %
CLT	67	5 %

(b) A0 mode

Table 4.4: Root mean square deviation of defuzzyfied identified parameters and nominal values with respect to experimentally measured velocities

CHAPTER 5

Delamination Localization in Structures with Prior Damage

To date, most of the developed guided ultrasonic wave-based techniques endure fitness of service. However, they depend on reference data, which could make the techniques less attractive for inspection of practical composite structures.

Initial studies in baseline free damage detection with guided waves were conducted in isotropic media. The first study applied the time reversal theory to trace back the signals from the sensing points to the location of the damage in metal plates [85]. Later, the time reversal technique was applied to long-range ultrasound in pipe lines [16]. Following a different approach, Anton proposed a baseline–free method based on the information collected from the undamaged regions, which is used as a baseline to localize the damage in aluminum plates [3]. Other authors refined the time reversal method to improve damage localization in metallic plates [60, 2]. Among these studies, a few of them applied the time reversal technique to composite materials [58, 62, 89, 59]. However, the time reversal technique is infeasible for large composite structures because of the weak reflections. Most recently, a transmission-based method based on the reciprocity principle was used to detect added mass without utilizing baseline data in composites [30]. The type of damage investigated is not representative of delamination.

In this chapter, a guided ultrasonic wave-based method for damage detection – in absence of baseline data – is proposed. The NDE technique is used to localized delamination in a quasi-isotropic carbon fiber reinforced polymer (CFRP) laminate. A network of signal-paths is created by two contact transducers to localize the damage by comparing signals from

waves traveling equal distances and in the same direction, as shown in Section 5.1.2. The signals from waves crossing defective regions are compared with those from waves traveling in healthy zones of the plate. In Section 5.2, damage indices based on the cross–correlation and energy of the signals (see Section 5.1.3), in conjunction with an imaging method based on wave–transmission (see Section 5.1.5), is utilized to locate the damage in the composite plate.

5.1 Methods

5.1.1 Experimental setup

The two specimens used in this study are quasi-isotropic CFRP plates with thickness $2.25\,\text{mm}$ $(0.09\,\text{in})$ and dimensions $910 \times 910\ \text{mm}^2$ $(36 \times 36\,\text{in}^2)$. The plates are manufactured with eight woven plies made from Hexcel AS4 carbon fiber pre–impregnated with Newport 301 epoxy resin system, with a stacking sequence of $[0, 45, -45, 90]_\text{s}$. The material properties for the lamina are shown in Table 5.1. An artificial delamination is introduced in one of the plates, while the other is a pristine plate, which is used as a control sample in the study to validate the damage detection technique. In order to create an artificial delamination, a circular patch of release film with diameter $25.4\,\text{mm}$ $(1\,\text{in})$ is placed in the middle of the plate between the 4th and 5th plies. To verify the presence of the artificial delamination in the plate, ultrasonic c-scan inspection was conducted. As it can be seen in Fig. 5.1a, the image does not present significant loss in any area of the pristine plate, while the defective plate shows the delamination as an area with attenuation $< 20\,\text{dB}$ at the center of the panel as shown in Fig. 5.1b.

Table 5.1: Material properties for the lamina. Prepreg Hexcel AS4 Newport **301**

E_{11} [GPa]	E_{22} [GPa]	E_{33} [GPa]	G_{12} [GPa]	G_{13} [GPa]	G_{23} [GPa]	ν_{12}	ν_{13}	ν_{23}	ρ [kg/m]
67.9	67.9	8.37	3.13	2.85	2.85	0.03	0.41	0.41	1463

(a) Pristine plate

(b) Defective Plate

Defect size:
40x10 sq.mm

Defect size:
24mm dia.

(c) Defective Plate - Flaw
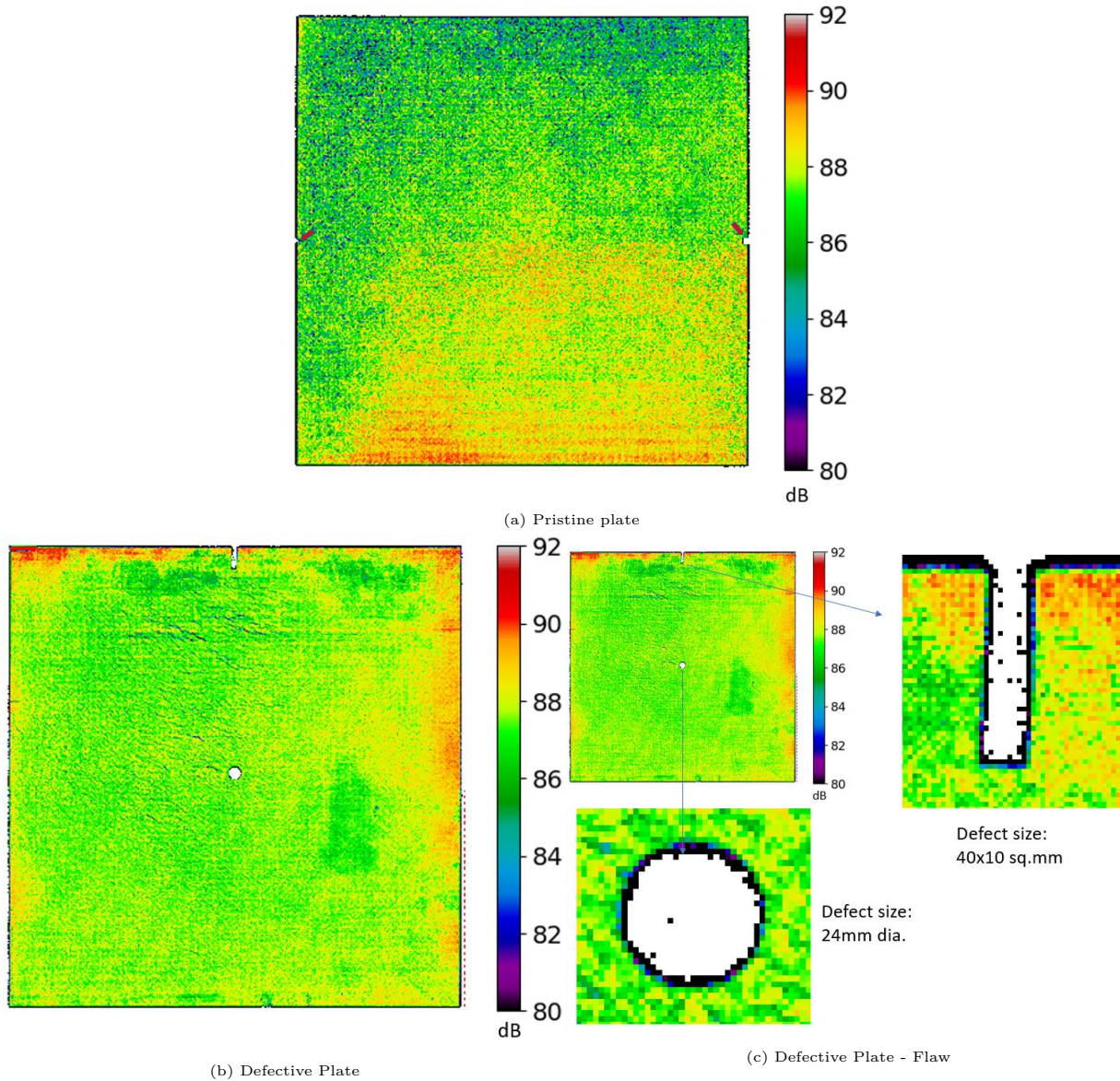
Figure 5.1: Trough Transmission Ultrasonic (TTU) C-Scan of CFRP plates

Since only two Digital–Wave B225 transducers are used during the data acquisition, a plexiglass grid with dimensions 410 x 250 mm^2 (16 x 10 in^2) is utilized to position the transducers on the plate to simulate a sensing network (see Fig. 5.2a). Spacers between the grid and the plate prevent waves from traveling along the grid. An ultrasonic couplant from Sonotech is used to improve the transmission of energy between the transducers and the test plate. A function generator, NI PXI-5402, is used to generate the ultrasonic signals. The signals are recorded by an oscilloscope, Agilent 54624A. The generated and sensing signals

are amplified by an A3000-Ritec voltage amplifier and Digital Wave FM-1, respectively.

5.1.2 Excitation of guided waves

Due to the dispersive behavior of Lamb waves, the material dispersion curves are essential to avoid the excitation of waves in highly dispersive or multi-modal frequencies for simpler signal interpretation. To calculate the dispersion curves, the quasi-isotropic CFRP plate is modeled as a transversely isotropic homogenized single-layer. Classical lamination theory is used to obtain the homogenized model [6]. The homogenized material properties are shown in Table 5.2. Fig. 5.2b shows the group velocity dispersion curves of the homogenized model for a frequency range below $600\,\text{kHz}$, where only the modes A0, S0 and A1 are present. The plate is actuated with a chirp signal of frequencies between $20\,\text{kHz}$ to $420\,\text{kHz}$ and signals are recorded with a recording time of $1\,\text{ms}$ with a sampling frequency of $2.8\,\text{MHz}$. Fig. 5.3 shows the network of signal-paths over the scan area. In this figure, the transducer acting as an actuator is positioned on the left of the damage, and the transducer acting as a receiver is placed on the right. The positions of the actuator are denoted by S_i, $i = 1,\ldots,11$, and those of the receiver as R_j, $j = 1,\ldots,11$. The positions S_i and S_{i+1} are spaced by $25.4\,\text{mm}$ ($1\,\text{in}$). The same spacing is applied to the receiver's position. The distance between transducers is $0.41\,\text{m}$ (16") for positions where the indices are the same, $i = j$. A total of 91 signal-paths are recorded which are separated in eleven groups according to the direction that the direct waves travel.

Table 5.2: Material properties for Quasi-isotropic CFRP plate with $\mathbf{x_1 x_2}$ plane of isotropy

$E_{11}[\text{GPa}]$	$E_{33}[\text{GPa}]$	$G_{13}[\text{GPa}]$	ν_{12}	ν_{13}	$\rho[\text{kg/m}^3]$
47.54	8.37	2.85	0.32	0.29	1463
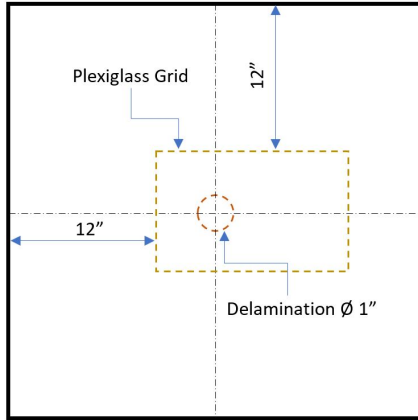
(a) Grid positioning in a composite plate
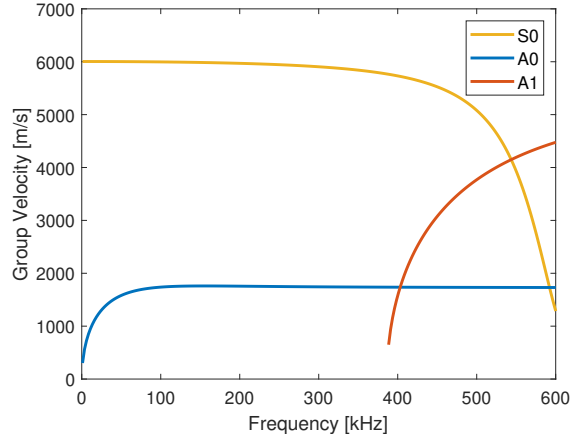
(b) Group velocity dispersion curves in a Quasi-isotropic CFRP plate

Figure 5.2: Experimental setup
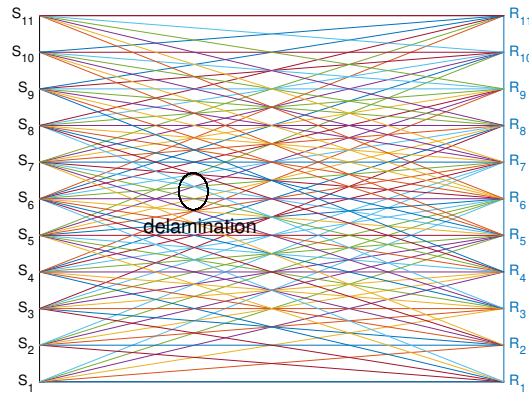
Figure 5.3: Path-network created by two contact transducers.

5.1.3   Damage index

A narrow-band signal extraction from chirp signals is used to find the most sensitive signal to the delamination. Among the extracted signals, as illustrated in Fig. 5.4, the signal response to a 5-cycle Hann windowed sine signal at $70\,\mathrm{kHz}$ is more sensitive to delamination. Compared to the normalized signal of the healthy path from S_{11} to R_{11}, the signal of the waves travelling along the damage path, from S_6 to R_6, has a time delay in the time window from $0.30\,\mathrm{ms}$ to $0.38\,\mathrm{ms}$ as depicted in Fig. 5.4b. Due to the fact that the time delay between signals can be used to identify the signal-paths crossing the defective region in the plate, a

(a) Paths of waves in group 0

(b) Time-windowed signals of paths $S_{11}R_{11}$ and S_6R_6
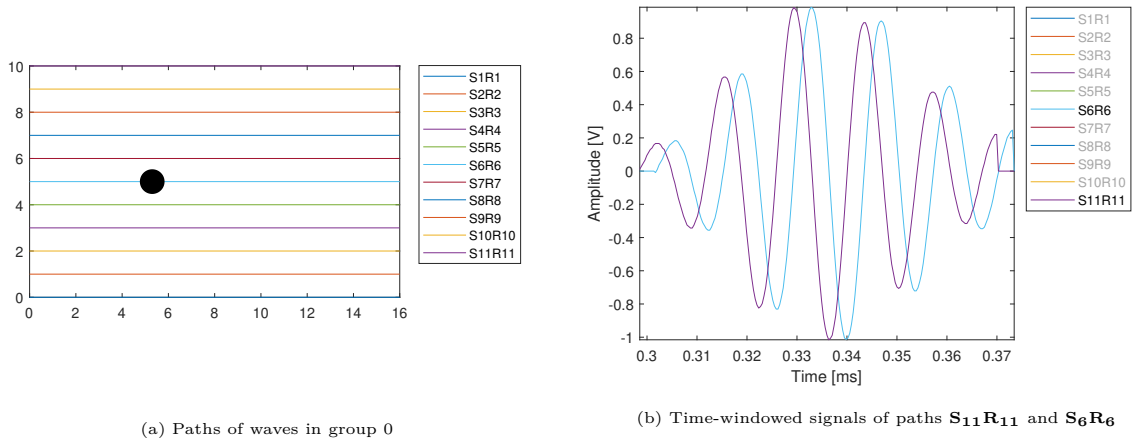
Figure 5.4: Signal sensitivity to delamination of a group of waves with propagation angle $0°$

damage index (DI) based on the cross-correlation between two signals is one of the damage indices chosen for this study. The lag associated to the maximum of the cross-correlation $\mathcal{X}$ between signals with parallel paths τ_k is given by,

$$\tau_k = \max\left(\mathcal{X}(x_j(w), y_j(w))\right) \tag{5.1}$$

where the signals x_j and y_j are the narrow-band extractions from the chirp signals at the sensing point j. The signal y_j is any signal used as a reference in the group to calculate the cross-correlation. This selection implies that one of the values of τ_k is the result of the auto-correlation of the signal y_j. A time–window w with the same period as the excitation signal s_i is applied to the signals x_j and y_j. To apply the time–window, starting from the time of arrival (ToA) of the peak of the envelope of the signal r_j, half of the period of signal s_i is subtracted from the ToA to bound signal r_j on the left. Half of the period of signal s_i is added to ToA to bound signal r_j on the right. Considering that cross-correlation lags for paths crossing the defective region should have a considerable difference with respect to lags for other paths in the group of parallel paths, the following form of DI is proposed,

$$DI_k^I = \left(\tau_k - \widetilde{\mathcal{T}}\right)^2 \tag{5.2}$$

where $\widetilde{\mathcal{T}}$ is the median of the collection of the lag–values of all signal–paths of waves propagating in the same direction. This form of damage index considers the deviation of the

71

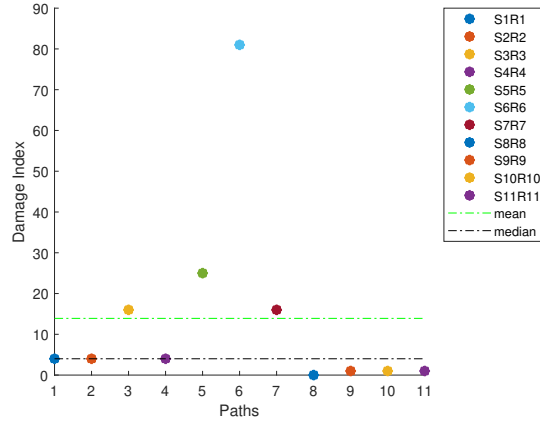Figure 5.5: Damage indices DI^{I} of a group of waves with propagation angle $\mathbf{0}°$

cross-correlation lag of each path with respect to the median of the lag values of the same group, $\widetilde{\mathcal{T}}$. Fig. 5.5 shows the distribution of the damage indices of the signal–paths presented in Fig. 5.4a. In the distribution of the damage indices, the furthest DI_k^{I} from the median value is S_6R_6, which is a signal–path affected by the delamination in the group. Another result of the interaction between the propagating waves and the defect is the change in the waves amplitude. Fig. 5.6b shows a significant drop in the amplitude of the signals of the waves travelling from S_6 to R_8. Compared to the maximum amplitude of the signal–path $\text{S}_9\text{R}_1 1$, the maximum amplitude of the signal at path S_6R_8 is less than 50%. Signal–path S_5R_7 is the second lowest amplitude in the group. Similar drops in amplitude are observed when interactions between the signal–paths and the boundaries of the flaw occur. However, in the case of signal–paths crossing the defect as Fig. 5.6d shows, there is not much variation in amplitude compared to other signals in the group. Small variations in the signals' amplitudes, such as S_6R_9, cannot be attributed to physical interaction but rather random experimental errors. Hence, to account for the signals' variations in amplitude due to the presence of damage, a second DI is proposed by the following formula,

$$\text{DI}_k^{\text{II}} = |e_k - \widetilde{\mathcal{E}}| \tag{5.3}$$

where $\mathcal{E}$ groups the square magnitude of the signals e_k of parallel paths, and $\widetilde{\mathcal{E}}$ is the median value of $\mathcal{E}$. Fig. 5.7 shows the magnitude of the damage indices DI_k^{II} of each path with respect
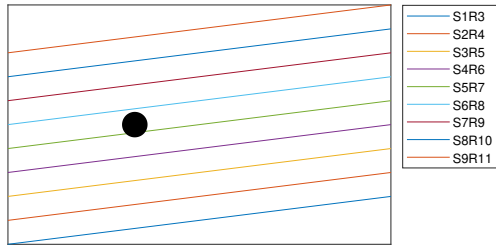
(a) Paths of waves in group 2
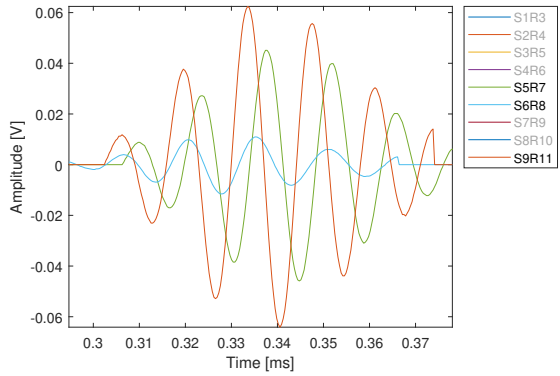
(b) Time-windowed signals of paths S_5R_7, S_6R_8 and S_9R_{11}
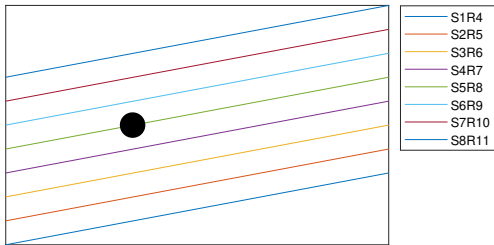
(c) Paths of waves in group 3
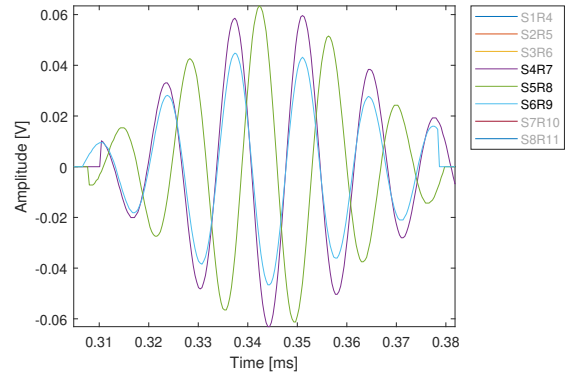
(d) Time-windowed signals of paths S_4R_7, S_5R_8 and S_6R_9

Figure 5.6: Signal sensitivity to delamination of group of waves 2 and 3

to the median value of the group of parallel paths presented in Fig. 5.6a, where the DI of the path S_6R_8 is the highest in the group.

5.1.4 Defining damage parameter

The overall likelihood of damage in the specimen can be determined by inspecting the standard deviations of the DIs in each group of parallel paths. Compared to a pristine sample, where the damage indices would be clustered around the mean value, the presence of a defect would result in a higher standard deviation.
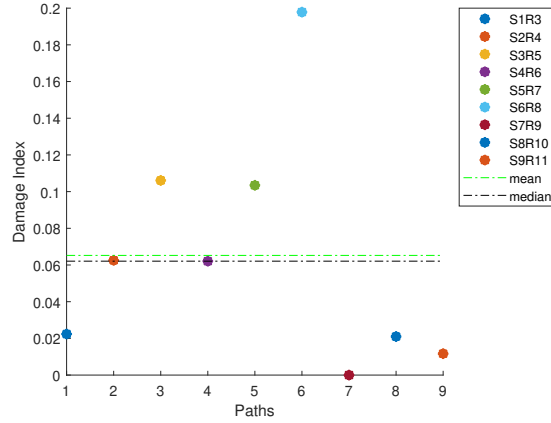
Figure 5.7: Damage indices $\mathrm{DI}^{\mathrm{II}}$ of waves in group 2

5.1.5 Imaging method

In the next section, an imaging method is used to predict the location of delamination in the inspected region. This imaging approach is based on the RAPID method [92], where the spatial distribution function has been modified. The proposed spatial distribution function expands the area of influence of each path k in a rectangular region, keeping the area of the rectangle constant along the path. This modification has shown to improve the imaging method in this work. The spatial function is given by,

$$A_k(x,y) = b_k(x,y) + \frac{b_k(x,y) - \beta_1}{\beta_2 - \beta_1} \quad \forall b_k \leq \beta_1, \qquad A_k(x,y) = \frac{b_k(x,y) - \beta_1}{\beta_2 - \beta_1} \quad \forall \beta_1 \leq b_k \leq \beta_2$$

$$(5.4)$$

where β_1 and β_2 are parameters to control the size of the area of influence. The variable b_k is obtained from the cross-product of the vectors from each imaging point in the inspection area to the transducers of the path k. The cross-product is then normalized with respect to the path's length. Fig. 5.8a presents the modified area of influence for path $\mathrm{S}_1\mathrm{R}_6$, where the influence goes from high values in the center of the path to no influence in remote points.

Considering that the transducer locations are points of convergence for different sig-nal–paths, areas around these locations affect the damage prediction by including fictitious defective spots. In order to remove the effect of the transducer location from the area of influence of the path, another spatial distribution function is required [88]. The function is

(a) Function A_k for path $S_1 R_6$. $\beta_1 = 0.1$ and $\beta_2 = 1$ (b) Function T_k for transducers S_1 and R_6. $\gamma = 3$
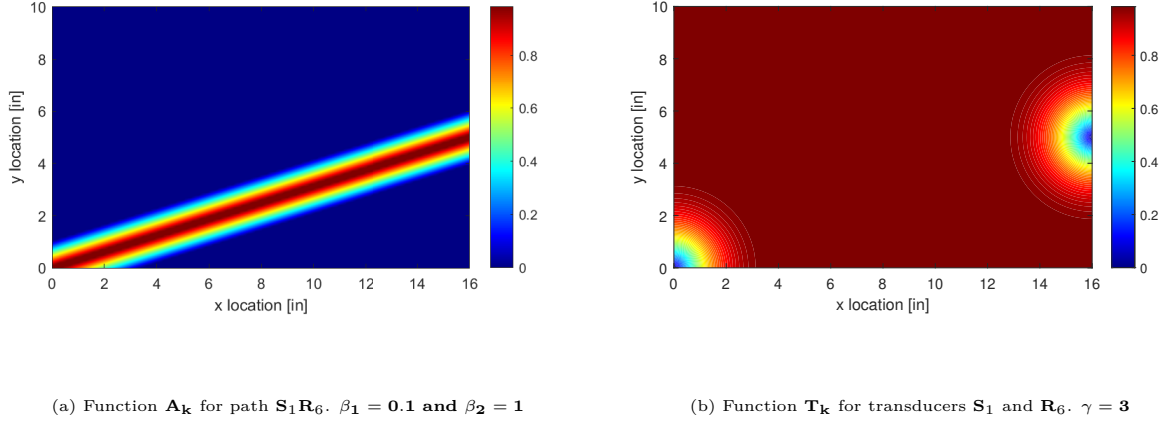
Figure 5.8: Areas of influence of the path $S_1 R_6$

defined as,

$$
T_k(x, y) = \left(1 - \frac{(r - r_i)^\gamma}{r^\gamma} \right) \left(1 - \frac{(r - r_j)^\gamma}{r^\gamma} \right) \quad \forall r_i, r_j < r, \qquad T_k(x, y) = 1 \quad r_i, r_j \geq r
$$

(5.5)

where γ is a parameter to control the size of the area of influence. The variables r_i and r_j are the vectors from each imaging point to the actuator and receiver transducers of the path k, respectively. r is one quarter of the path length. In Fig. 5.8b the areas of influence for the transducers of the path $S_1 R_6$ are shown. Note that for points close to the transducer locations the influence nearly vanishes. Therefore, the product of the spatial functions results in the subtraction of the transducers' influence from the path's. In order to interpolate each damage index DI_k along the corresponding path k, the spatial distribution functions are multiplied by the DI_k. The following interpolation function gives the area of influence of each DI_k in the inspection region:

$$
P_k(x, y) = DI_k A_k(x, y) T_k(x, y)
$$

(5.6)

To account for the contribution of all the signal-paths in the localization of the defect, the area of influence of the paths P_k are combined by the interpolation function [88],

$$
P(x, y) = |P_m(x, y) \cup P_n(x, y)| = |P_m(x, y) + P_n(x, y) - P_m(x, y) P_n(x, y)|
$$

(5.7)

(a) Prediction based on DI^{I} (b) Prediction based on DI^{II}
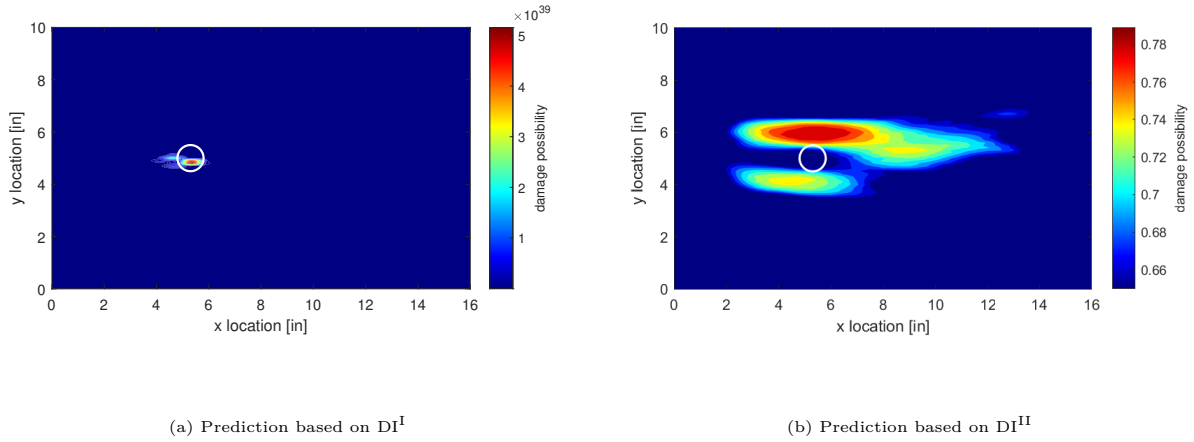
Figure 5.9: Predicted delamination's location in a quasi-isotropic CFRP plate. Delamination size is 1 in diameter and inspection area 16 in x 10 in

5.2 Results

Using the proposed baseline–free damage detection technique, damage indices based on the cross–correlation of the signals DI^{I} and their variation in amplitude DI^{II} are calculated for 91 signal–paths. Separately, the damage indices DI^{I} and DI^{II} are then combined by the interpolation function $\text{P}(x, y)$ to predict the location of a delamination in a CFRP plate. As seen in Fig. 5.9, the possibility of damage is higher inside the delamination region when DI^{I} is used in the interpolation, while the use of DI^{II} results in two indications of high damage possibility in areas near the defect. The results from DI^{II} are consistent with the observation made earlier that the signal amplitudes of paths crossing the delamination are not sensitive, while only the signals interacting with the boundaries of the defect contribute to localize the damage. On the other hand, the results in Fig. 5.9a suggest that the density of the crossing paths in the signal network could influence the prediction. To address this concern, considering that the signal–paths with the highest damage index DI^{I} in each group are the most influential localizing the defect, they are selected for the interpolation to predict the damage location. For instance, the signal–path S_6R_6 in Fig. 5.5 is selected among the others in the group for having the highest damage index to calculate its DI's area of
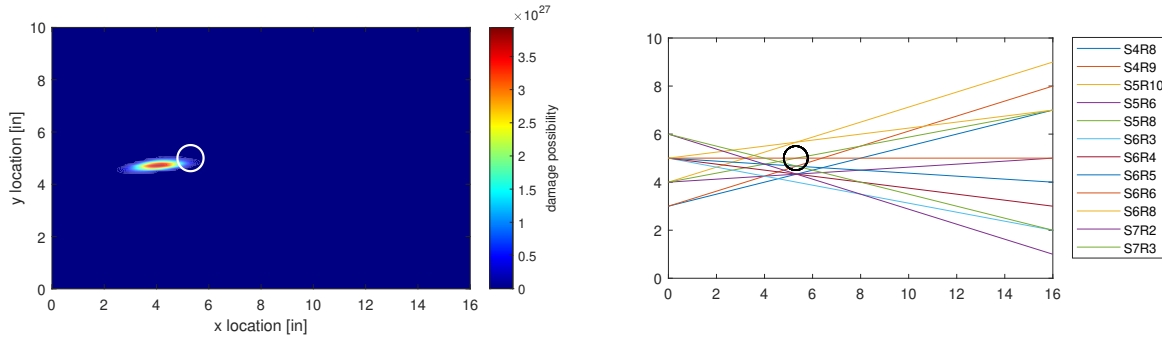
(a) Prediction using the signal–paths with the highest DI$^\text{I}$ (b) Signal–paths affected by the delamination

Figure 5.10: Predicted delamination's location in a quasi-isotropic CFRP plate using only the signal–paths with the highest DI$^\text{I}$ in each group of parallel paths . Delamination size is 1 in diameter and inspection area 16 in x 10 in

influence $\text{P}_\text{S6R6}(x, y)$ in Eqn. (5.6). $\text{P}_\text{S6R6}(x, y)$ together with the selected $\text{P}_k(x, y)$ from other groups are then interpolated in Eqn. (5.7) to make the prediction. Fig. 5.10a shows that the prediction of the defect's location moves 5 mm (0.2 in) to the left of the actual defect when only the twelve paths shown in Fig. 5.10b are selected for the analysis. The predicted location still remains in the vicinity of the actual delamination region, despite the total number of signals used in the analysis represents only a 13% of the original signals acquired.

To study the sensitivity of the damage detection technique using a sensor network with reduced number of paths where the position of the defect breaks the symmetry of the grid, the delamination is moved to a new location in the inspection area, as Fig. 5.11a shows. In the new position a fewer number of signal–paths interact with the defect. In addition, the new position of the defect does not lie on any of the axes of symmetry of the sensor–network. The results using all the signal–paths in the sensing network and only the paths with the highest DI$^\text{I}$ in each group are presented in Fig. 5.11b and Fig. 5.11d, respectively. In this particular case, the selection of the signal–paths with higher DI$^\text{I}$ improves the prediction of the damage's location.
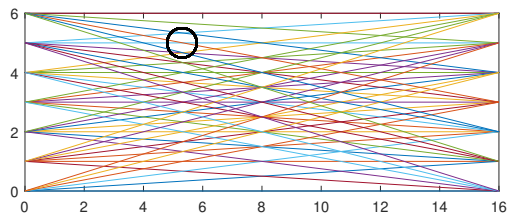
(a) Path–network
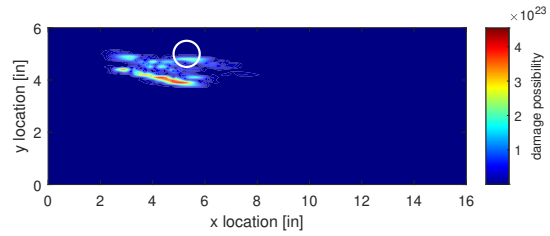
(b) Prediction based on DI$^\text{I}$
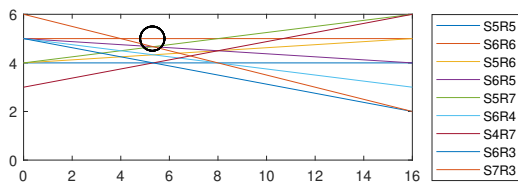
(c) Signal–paths affected by the delamination
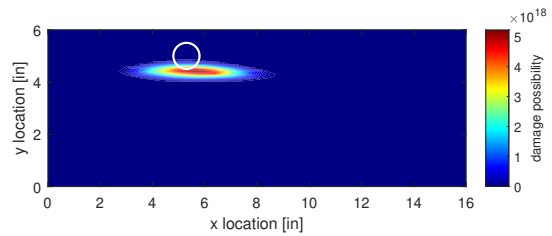
(d) Prediction using the signal–paths with the highest DI$^\text{I}$

Figure 5.11: Predicted delamination's location in a quasi-isotropic CFRP plate reducing the number of sensing paths. Delamination size is 1 in diameter and inspection area 16 in x 10 in

By looking at the damage possibility scale in the results, the values vary by more than one order of magnitude between cases, as the number of signal–paths increases. These variations make it difficult to set a level of confidence for non–destructive evaluation. However, defining a damage parameter based on the standard deviation of the DIs can provide a better decision–making path to set a threshold during the assessment. Fig. 5.12a shows the damage detection technique applied to a pristine plate by following the same experimental setup as Fig. 5.3 shows. As it is expected, some localized indications are seen in the figure at an arbitrary color scale which, in the case of no prior knowledge of the state of the structure, can lead to erroneous conclusions, despite the fact that the maximum value in the scale is very small compared to any of previous results. However, by inspecting the standard deviations

78

(a) Prediction based on DI^I on a pristine quasi-isotropic CFRP plate. Inspection area 16 in x 10 in

(b) Damage parameter based on DI^I. Plate with defect (blue). Pristine plate (orange)
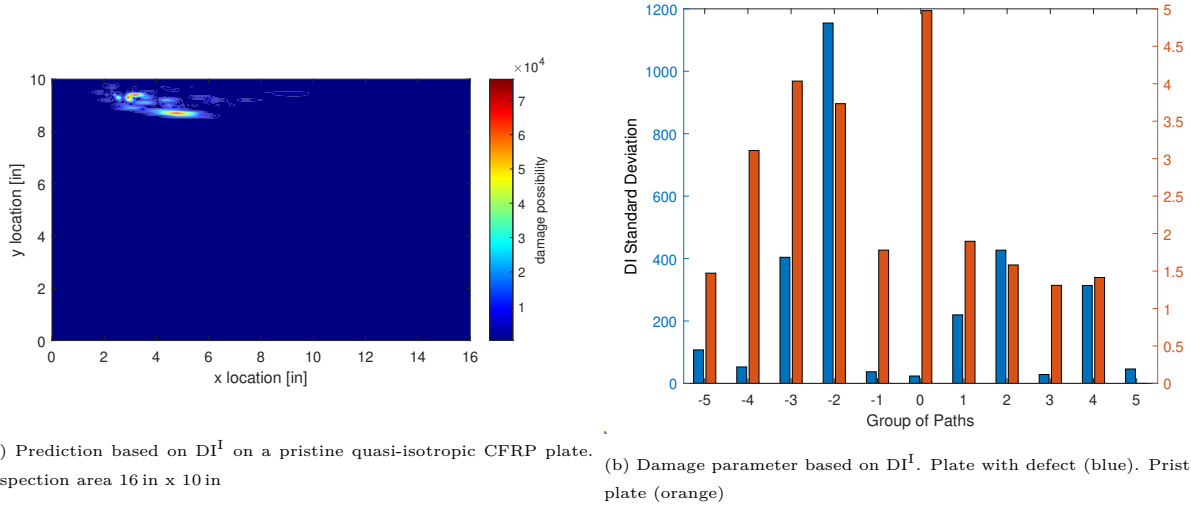
Figure 5.12: Level of confidence based on the standard deviation of the DIs for quasi-isotropic CFRP plates.

of the pristine and damaged plates, it is possible to set a threshold, which is independent of the number of sensing paths in the inspection area. Fig. 5.12b presents the standard deviations of the eleven groups of paths based on DI_k^1 for the pristine sample and the sample with the delamination in two different scales. In the figure, the blue scale illustrates that the minimum overall standard deviation value of the plate with a flaw is four times higher than the maximum overall value of the pristine plate, which is represented by the orange scale. In addition, the standard deviation of the parallel paths in group 5 for the pristine plate is zero because the DIs for all the paths is zero. According to these results, the red spot in Fig. 5.12a can be classified as trivial with a high level of confidence by setting a threshold based on the standard deviation of the plate with damage.

CHAPTER 6

Concluding Remarks

In this dissertation, an efficient guided ultrasonic wave-based technique to detect delamination in CFRP plates without baseline data has been developed. An existing theoretical model for the identification of the source type of AE events has been refined to make it more efficient. Moreover, a new nondestructive material characterization method has been developed by employing fuzzy arithmetic in conjunction with measured group velocity data. The inversion and defuzzyfication procedures to determine new nominal values for material properties have been shown to provide more accurate results.

In Chapter. 3, for two-dimensional problems, the new form of the Green's function for multilayered media has demonstrated to be more efficient than other analytical methods without sacrificing the integrity of the results. The new Green's function is calculated with the modal functions of the displacements and stresses obtained in the wavenumber domain. The fact that the inverse Fourier transform is not needed to obtain the function in the frequency domain reduces the computational time compared to other methods, and it decreases the possibility of introducing numerical errors in the calculations. Application of Born's first approximation theory in the calculation of the scatter field in a guided-wave with thickness change disagreed with the results found in the literature. The lack of consideration of the nonpropagating modes affects the energy balanced in the region of the plate near the step. Thereby, the calculated displacements do not show the expected variation in the frequency range due to the mode conversion. Unfortunately, the model developed with the new Green's function does not support the inclusion of the nonpropagating modes in the solution; only propagating modes can be considered. In an opposite result, the displacement calculated from different crack-types with the AE model has shown good agreement with results found

in the literature. The model has been capable of characterizing the nature of the AE event in isotropic plates through the waveform of the propagating waves calculated on the plates' surfaces. Only the antisymmetric and symmetric propagating modes contribute to the mode-II and mode-I microcracks, respectively. The results from the test cases indicate that the combination of the AE model with the new form of the Green's function has the potential to efficiently evaluate the response to AE events in composite plates. Future work on this subject includes the application of the model to thin and thick CFRP laminates.

Material characterization in composites without considering uncertainty could lead to a significant error when inversion procedures based on time-domain data are employed. In Chapter. 4, for the studied CFRP specimen, it has been shown that experimentally measured group velocities vary as much as $7\,\%$ of the nominal value at $200\,\mathrm{kHz}$ for the S0 mode across different regions of the laminate. Furthermore, the group velocities calculated with initially estimated nominal material values based on manufacturing data and standard material models have been shown to substantially differ from the experimentally measured velocities. In addition, it has been found that the level of influence of the material properties on the calculation of the group velocities strongly varies among the parameters. Specifically, the Young's modulus E_{11} and the Poisson's ratio ν_{12} are the most influential material properties for the S0 mode, while the shear modulus G_{13} is the most influential for the A0 mode. As a result, only these parameters see a substantial change through the fuzzy-based inversion technique. Moreover, inclusion of all propagating modes in a small frequency range has been found to be well-suited to consolidate the identified uncertainties of the material properties as compared to single-mode analysis in a broader frequency range. Furthermore, based on the normalized RMSD values, the inclusion of the highly dispersive zone of the A0 mode does not have a strong effect on the definition of the new nominal values. Although the normalized RMSD values are slightly different in the S0 mode, both analyses (multi-mode and single-mode) provide an adequate representation of the group velocities in the laminate.

It is acknowledged that the experimentally measured group velocities for the A0 mode do not show the expected frequency dependence between $50 - 100\,\mathrm{kHz}$. Thus, more research is

needed to investigate the efficacy of the employed experimental methods in conjunction with advanced fuzzy theory in material characterization of CFRP panels with different stacking sequences and material combinations. Future work comprises also the validation of the newly determined material properties with data from destructive material testing, and further refinement of the method by including higher order guided wave modes in the inversion technique.

In Chapter. 5, the baseline-free NDE technique employs the lag associated to the cross-correlation between signals DI^{I} and the signal energy DI^{II} to calculate a damage index distribution, where signals from waves crossing defective regions are identified. DI^{II} has demonstrated to be more sensitive to waves' trajectories affected by the diffraction of waves around the flaw, while DI^{I} identify waves' paths crossing the defect. To propagate the influence of the damage index of each signal path to the inspection region, spatial distribution functions are used. The combination of the damage indices in conjunction with interpolation functions enables the prediction of delamination. In an inspected area of $410 \times 250\,\text{mm}^2$ (16 x $10\,\text{in}^2$), this method successfully localized delamination of $25.4\,\text{mm}$ (1 in) diameter in a quasi-isotropic CFRP laminate. The reliability of the technique can be affected by the extension of the defective area and the proximity of the defect to wave reflectors. More research is necessary to set the limitations of the technique.

APPENDIX A

APPENDIX

A.1 Chapter 2

A.1.1 Transversely isotropic layer

The expressions A_q and C_{ij} for a transversely isotropic layer are given by

$$A_1 = \sqrt{\frac{-A + \sqrt{A^2 - 4B}}{2}} \quad A_2 = \sqrt{\frac{-A - \sqrt{A^2 - 4B}}{2}} \tag{A.1}$$

where

$$A = \frac{c^2}{c_{3L}^2} + \frac{c^2}{c_{3T}^2} - \frac{C_{11}C_{33} - C_{13}^2 - 2C_{13}C_{44}}{C_{33}C_{44}}, \quad B = \left(\frac{c^2}{c_{3T}^2} - 1\right)\left(\frac{c^2}{c_{3T}^2} - \frac{C_{11}}{C_{33}}\right). \tag{A.2}$$

and the definitions of the bulk wave velocities are

$$c_{1L} = \sqrt{\frac{C_{11}}{\rho}}, \quad c_{3L} = \sqrt{\frac{C_{33}}{\rho}} \quad \text{and} \quad c_{3T} = \sqrt{\frac{C_{44}}{\rho}}, \tag{A.3}$$

C_{ij} are respective elements of the elasticity tensor.

A.1.2 Unidirectional CFRP plate

The functions Δ_i of the dispersion equations for a unidirectional fiber-reinforced composite plate are given by.

$$\Delta_1 = \zeta_2\left[(\xi_2^2 + \zeta_3^2)q_{22} - (\xi_2^2 - \zeta_3^2)q_{12}\right]\left[(a_5 - a_3)\xi_1^2 q_{11} - (a_1 - 2a_4)\xi_2^2 q_{21} - a_1\zeta_1^2 q_{21}\right] \tag{A.4}$$

$$\Delta_2 = \zeta_1\left[(\xi_2^2 + \zeta_3^2)q_{21} - (\xi_2^2 - \zeta_3^2)q_{11}\right]\left[(a_5 - a_3)\xi_1^2 q_{12} - (a_1 - 2a_4)\xi_2^2 q_{22} - a_1\zeta_2^2 q_{22}\right] \tag{A.5}$$

$$\Delta_3 = 4a_4\xi_2^2\zeta_1\zeta_2\zeta_3(q_{11}q_{22} - q_{12}q_{21}) \tag{A.6}$$

where,

$$a_1 = C_{22}/\rho, \quad a_2 = C_{11}/\rho, \quad a_3 = (C_{12}+C_{55})/\rho, \quad a_4 = (C_{22}-C_{23})/2\rho, \quad a_5 = C_{55}/\rho \quad (A.7)$$

$$q_{11} = a_3 b_1, \quad q_{12} = a_3 b_2, \quad q_{21} = \omega^2 - a_2\xi_1^2 - a_5 b_1, \quad q_{22} = \omega^2 - a_2\xi_1^2 - a_5 b_2 \quad (A.8)$$

and

$$\zeta_1^2 = -\xi_2^2 + b_1, \quad \zeta_2^2 = -\xi_2^2 + b_2, \quad \zeta_3^2 = \frac{\omega^2 - a_5\xi_1^2 - a_4\xi_2^2}{a_4} \quad (A.9)$$

in which

$$\xi = \omega/c, \quad \xi_1 = \xi\cos(\theta), \quad \xi_2 = \xi\sin(\theta) \quad (A.10)$$

$$b_1 = -\frac{B}{2A} - \sqrt{\left(\frac{B}{2A}\right)^2 - \frac{C}{A}}, \quad b_2 = -\frac{B}{2A} + \sqrt{\left(\frac{B}{2A}\right)^2 - \frac{C}{A}} \quad (A.11)$$

$$A = a_1 a_5, \quad B = (a_1 a_2 + a_5^2 - a_3^2)\xi_1^2 - \omega^2(a_1 + a_5), \quad C = (a_2\xi_1^2 - \omega^2)(a_5\xi_1^2 - \omega^2) \quad (A.12)$$

Bibliography

[1] J. Achenbach. *Wave Propagation in Elastic Solids*. North Holland, Amsterdam, November 1987.

[2] Jitendra Agrahari and Santosh Kapuria. A refined lamb wave time-reversal method with enhanced sensitivity for damage detection in isotropic plates. *Journal of Intelligent Material Systems and Structures*, 27, 06 2015.

[3] Steven Anton and Daniel Inman. Reference-free damage detection using instantaneous baseline measurements. *AIAA Journal*, 47:1952–1964, 08 2009.

[4] Leonardo Araque, Lifu Wang, Ajit Mal, and Christoph Schaal. Inverse fuzzy arithmetic for material characterization of composites using guided waves. In Paul Fromme and Zhongqing Su, editors, *Health Monitoring of Structural and Biological Systems XV*, volume 11593, pages 201 – 213. International Society for Optics and Photonics, SPIE, 2021.

[5] Leonardo Araque, Lifu Wang, Steffen Tai, Ajit Mal, and Christoph Schaal. Uncertainty characterization of guided ultrasonic wave properties in composite materials. In Paul Fromme and Zhongqing Su, editors, *Health Monitoring of Structural and Biological Systems IX*, volume 11381, pages 28 – 36. International Society for Optics and Photonics, SPIE, 2020.

[6] Harsh Baid, Christoph Schaal, Himadri Samajder, and Ajit Mal. Dispersion of lamb waves in a honeycomb composite sandwich panel. *Ultrasonics*, 56(0):409–416, 2015.

[7] S Banerjee and A. K Mal. Acoustic emission waveform simulation in multilayered composites. *The Journal of Strain Analysis for Engineering Design*, 40(1):25–32, 2005.

[8] Yoseph Bar-Cohen, Ajit Mal, and Shyh-Shiuh Lih. Nde of composite materials using ultrasonic oblique insonification. *Materials Evaluation; (United States)*, 51:11, 11 1993.

[9] R. Burridge and L. Knopoff. Body force equivalents for seismic dislocations. *Bulletin of the Seismological Society of America*, 54(6A):1875–1888, 12 1964.

[10] Anna Castellano, Pilade Foti, Aguinaldo Fraddosio, Salvatore Marzano, and Mario D Piccioni. Mechanical characterization of cfrp composites by ultrasonic immersion tests: Experimental and numerical approaches. *Composites Part B: Engineering*, 66:299–310, 2014.

[11] M Chandrasekhar and Ranjan Ganguli. Impact of material uncertainty on delamination detection in composite plate structures using modal curvatures and fuzzy logic. In *AIAA Scitech 2019 Forum*, 01 2019.

[12] Ramadas Chennamsetti, Krishnan Balasubramaniam, M Joshi, and Krishnamurthy Chitti Venkata. Interaction of guided lamb waves with an asymmetrically located delamination in a laminated composite plate. *Smart Materials and Structures*, 19:065009, 04 2010.

[13] R. Cui and F. Scalea. Identification of elastic properties of composites by inversion of ultrasonic guided wave data. *Experimental Mechanics*, 03 2021.

[14] Ranting Cui and Francesco Lanza di Scalea. On the identification of the elastic properties of composites by ultrasonic guided waves and optimization algorithm. *Composite Structures*, 223:110969, 2019.

[15] Adrianus T. de Hoop. *Representation theorems for the displacement in an elastic solid and their application to elastodynamic diffraction theory.* PhD thesis, Technische Hogeschool, Delft, 1958.

[16] C. Ennaceur, P Mudge, B Bridge, Malik Kayous, and Tat Hean Gan. Application of the time reversal technique to the focusing of long-range ultrasound in pipelines. *Insight*, 49:217–223, 04 2007.

[17] A. G. Every and Wolfgang Sachse. Determination of the elastic constants of anisotropic solids from acoustic-wave group-velocity measurements. *Phys. Rev. B*, 42:8196–8205, Nov 1990.

[18] R. W. Fredricks. Scattering of elastic pulses by obstacles of infinite impedance and semi-infinite dimensions on the surface of a half space: Ph.d. thesis, university of california, los angeles. In *Scattering of elastic pulses by obstacles of infinite impedance and semi-infinite dimensions on the surface of a half space*, 1959.

[19] Ranjan Ganguli. A fuzzy logic system for ground based structural health monitoring of a helicopter rotor using modal data. *Journal of Intelligent Material Systems and Structures*, 12(6):397–407, 2001.

[20] U. Gauger, S. Turrin, M. Hanss, and L. Gaul. A new uncertainty analysis for the transformation method. *Fuzzy Sets and Systems*, 159(11):1273–1291, 2008.

[21] D Guo, A Mal, and K Ono. Wave theory of acoustic emission in composite laminates. *Journal of acoustic emission*, 14(3-4):S19–S46, 1996.

[22] T. Haag, S. Carvajal González, and M. Hanss. Model validation and selection based on inverse fuzzy arithmetic. *Mechanical Systems and Signal Processing*, 2011.

[23] T. Haag and M. Hanss. Model assessment using inverse fuzzy arithmetic. In *Information Processing and Management of Uncertainty in Knowledge-Based Systems*, volume 81 of *Communications in Computer and Information Science*, pages 461–470. Springer, 2010.

[24] Joe K. Hammond and Paul R. White. The analysis of non-stationary signals using time–frequency methods. *Journal of Sound and Vibration*, 190(3):419–447, 1996.

[25] M. Hanss. *Applied Fuzzy Arithmetic – An Introduction with Engineering Applications.* Springer, Berlin, 2005.

[26] M. Hanss, Stefan Hurlebaus, and Lothar Gaul. Fuzzy sensitivity analysis for the identification of material properties of orthotropic plates from natural frequencies. *Mechanical Systems and Signal Processing*, 16:769–784, 09 2002.

[27] Jon C. Helton, Jay D. Johnson, William L. Oberkampf, and Cedric J. Sallaberry. Representation of analysis results involving aleatory and epistemic uncertainty. *International Journal of General Systems*, 39:605–646, 2010.

[28] I. Herrera. On a method to obtain a Green's function for a multi-layered half space. *Bulletin of the Seismological Society of America*, 54(4):1087–1096, 08 1964.

[29] F. O. Hoffman and J. S. Hammonds. Propagation of uncertainty in risk assessments: The need to distinguish between uncertainty due to lack of knowledge and uncertainty due to variability. *Risk Analysis*, 14:707–712, 1994.

[30] Liping Huang, Liang Zeng, and Jing Lin. Baseline-free damage detection in composite plates based on the reciprocity principle. *Smart Materials and Structures*, 27, 11 2017.

[31] J. A. Hudson and L. Knopoff. Transmission and reflection of surface waves at a corner: 2. rayleigh waves (theoretical). *Journal of Geophysical Research (1896-1977)*, 69(2):281–289, 1964.

[32] Maya Jacob John and Rajesh D. Anandjiwala. Recent developments in chemical modification and characterization of natural fiber-reinforced composites. *Polymer Composites*, 29(2):187–207, 2008.

[33] Robert Jones. *Mechanics of Composite Materials.* Taylor & Francis, 2nd edition, 1999.

[34] M. R. Karim, A. K. Mal, and Y. Bar-Cohen. Inversion of leaky lamb wave data by simplex algorithm. *The Journal of the Acoustical Society of America*, 88(1):482–491, 1990.

[35] A. Khojasteh, M. Rahimian, M. Eskandari, and R.Y.S. Pak. Three-dimensional dynamic green's functions for a multilayered transversely isotropic half-space. *International Journal of Solids and Structures*, 48(9):1349–1361, 2011.

[36] L. Knopoff. Diffraction of elastic waves. *The Journal of the Acoustical Society of America*, 28(2):217–229, 1956.

[37] T. Kundu and A.K. Mal. Elastic waves in a multilayered solid due to a dislocation source. *Wave Motion*, 7(5):459–471, 1985.

[38] H. Kwun and K. A. Bartels. Experimental observation of wave dispersion in cylindrical shells via time-frequency analysis. *The Journal of the Acoustical Society of America*, 97(6):3905–3907, 1995.

[39] FP La Mantia and M Morreale. Green composites: A brief review. *Composites Part A: Applied Science and Manufacturing*, 42(6):579–588, 2011.

[40] Horace Lamb. On waves in an elastic plate. *Proceedings of the Royal Society of London. Series A, Containing Papers of a Mathematical and Physical Character*, 93(648):114–128, 1917.

[41] N. A. Levy and A. K. Mal. Calculation of ground motion in a three-dimensional model of the 1966 Parkfield earthquake. *Bulletin of the Seismological Society of America*, 66(2):405–423, 04 1976.

[42] J. Enrique Luco and Randy J. Apsel. On the Green's functions for a layered half-space. Part I. *Bulletin of the Seismological Society of America*, 73(4):909–929, 08 1983.

[43] A. Mal. Guided waves in layered solids with interface zones. *International Journal of Engineering Science*, 26:873–881, 1988.

[44] A. Mal and L. Knopoff. Transmission of rayleigh waves past a step change in elevation. *Bulletin of the Seismological Society of America*, 55:319–334, 1965.

[45] A. K. Mal. Rayleigh waves from a moving thrust fault. *Bulletin of the Seismological Society of America*, 62(3):751–762, 06 1972.

[46] A. K. Mal. Wave propagation in layered composite laminates under periodic surface loads. *Wave Motion*, 10(3):257–266, 1988.

[47] A. K. MAL and L. KNOPOFF. Elastic Wave Velocities in Two-component Systems†‡. *IMA Journal of Applied Mathematics*, 3(4):376–387, 12 1967.

[48] A.K. Mal. Wave propagation in layered composite laminates under periodic surface loads. *Wave Motion*, 10(3):257–266, 1988.

[49] Alessandro Marzani and Luca De Marchi. Characterization of the elastic moduli in composite plates via dispersive guided waves data and genetic algorithms. *Journal of Intelligent Material Systems and Structures*, 24(17):2135–2147, 2013.

[50] J.C. Maxwell. *A Treatise on Electricity and Magnetism*, volume 1, chapter 9, Art. 310–314. Clarendon Press, Oxford, 1st edition, (3rd edition, 1982), 1873. See also Art. 322, pp. 447-448, for a composite laminate analysis.

[51] L. Neil McCartney. Predicting properties of undamaged and damaged carbon fibre reinforced composites. In Peter W. R Beaumont, Constantinos Soutis, and Alma Hodzic, editors, *The Structural Integrity of Carbon Fiber Composites: Fifty Years of Progress and Achievement of the Science, Development, and Applications*, pages 425–467. Springer International Publishing, Cham, 2017.

[52] R D Mindlin and Jiashi Yang. *An Introduction to the Mathematical Theory of Vibrations of Elastic Plates*. WORLD SCIENTIFIC, 2006.

[53] D. Moens and M. Hanss. Non-probabilistic finite element analysis for parametric uncertainty treatment in applied mechanics: Recent advances. *Finite Elements in Analysis and Design*, 47(1):4–16, 2011.

[54] Christopher Z Mooney. *Monte carlo simulation*, volume 116. Sage, Thousand Oaks, 1997.

[55] R. Newton. Scattering theory of waves and particles. In *Scattering theory of waves and particles*, 1966.

[56] Shinji Ochi. Development of high strength biodegradable composites using manila hemp fiber and starch-based biodegradable resin. *Composites part A: Applied science and manufacturing*, 37(11):1879–1883, 2006.

[57] Ronald Y. S. Pak and Bojan B. Guzina. Three-dimensional green’s functions for a multilayered half-space in displacement potentials. *Journal of Engineering Mechanics*, 128(4):449–461, 2002.

[58] Hyun Woo Park, Kincho Law, and Charles Farrar. Time reversal active sensing for health monitoring of a composite plate. *Journal of Sound and Vibration*, 302:50–66, 04 2007.

[59] Banibrata Poddar, Christudas Bijudas, Mira Mitra, and Prasanna Mujumdar. Damage detection in a woven-fabric composite laminate using time-reversed lamb wave. *Structural Health Monitoring*, 11, 08 2012.

[60] Banibrata Poddar, A Kumar, Mira Mitra, and Prasanna Mujumdar. Time reversibility of a lamb wave for damage detection in a metallic plate. *Smart Mater. Struct. Smart Mater. Struct*, 20:25001–10, 02 2011.

[61] A.S. Purekar and D.J. Pines. Damage detection in thin composite laminates using piezoelectric phased sensor arrays and guided lamb wave interrogation. *Journal of Intelligent Material Systems and Structures*, 21(10):995–1010, 2010.

[62] Wang Qiang and Yuan Shenfang. Baseline-free imaging method based on new pzt sensor arrangements. *Journal of Intelligent Material Systems and Structures - J INTEL MAT SYST STRUCT*, 20:1663–1673, 09 2009.

[63] Md Zillur Rahman, Krishnan Jayaraman, and Brian Richard Mace. Impact energy absorption of flax fiber-reinforced polypropylene composites. *Polymer Composites*, 39(11):4165–4175, 2018.

[64] Singiresu S. Rao and Qing Liu. Fuzzy approach to the mechanics of fiber-reinforced composite materials. *AIAA Journal*, 42(1):159–167, 2004.

[65] Sang-Ho Rhee, Jeong-Ki Lee, and Jung-Ju Lee. The group velocity variation of lamb wave in fiber reinforced composite plate. *Ultrasonics*, 47(1):55–63, 2007.

[66] Fabrizio Ricci, E. Monaco, N.D. Boffa, L. Maio, and V. Memmolo. Guided waves for structural health monitoring in composites: A review and implementation strategies. *Progress in Aerospace Sciences*, 129:100790, 2022.

[67] W. P. Rogers. Elastic property measurement using rayleigh-lamb waves. *Research in Nondestructive Evaluation*, 6(4):185–208, 1995.

[68] S. I. Rokhlin and D. E. Chimenti. *Reconstruction of Elastic Constants from Ultrasonic Reflectivity Data in a Fluid Coupled Composite Plate*, pages 1411–1418. Springer US, Boston, MA, 1990.

[69] S. I. Rokhlin, C. Y. Wu, and L. Wang. Application of coupled ultrasonic plate modes for elastic constant reconstruction of anisotropic composites. In Donald O. Thompson and Dale E. Chimenti, editors, *Review of Progress in Quantitative Nondestructive Evaluation*, pages 1403–1410. Springer US, Boston, MA, 1990.

[70] J.L. Rose. Ultrasonic guided waves in solid media. *Ultrasonic Guided Waves in Solid Media*, pages 1–512, 01 2014.

[71] Christoph Schaal and Michael Hanss. Fuzzy arithmetical assessment of wave propagation models for multi-wire cables. In Randall Allemang, James De Clerck, Christopher Niezrecki, and Alfred Wicks, editors, *Special Topics in Structural Dynamics, Volume 6*, Conference Proceedings of the Society for Experimental Mechanics Series, pages 177–185. Springer New York, 2013.

[72] Christoph Schaal and Michael Hanss. Uncertainty analysis for crack detection in cylindrical waveguides. *PAMM*, 14(1):695–696, 2014.

[73] Christoph Schaal, Miriam Krautter, and Michael Hanss. Dispersion in cylindrical waveguides with uncertain parameters. *PAMM*, 12(1):537–538, 2012.

[74] Christoph Schaal and Ajit Mal. Lamb wave propagation in a plate with step discontinuities. *Wave Motion*, 66, 06 2016.

[75] Christoph Schaal and Ajit Mal. Core-skin disbond detection in a composite sandwich panel using guided ultrasonic waves. *Journal of Nondestructive Evaluation, Diagnostics and Prognostics of Engineering Systems*, 1:011006, 09 2017.

[76] Christoph Schaal, Suzhou Zhang, Himadri Samajder, and Ajit Mal. An analytical study of the scattering of ultrasonic guided waves at a delamination-like discontinuity in a plate. *Proceedings of the Institution of Mechanical Engineers, Part C: Journal of Mechanical Engineering Science*, pages 1–14, 2017.

[77] Z Sharif-Khodaei and M H Aliabadi. Assessment of delay-and-sum algorithms for damage detection in aluminium and composite plates. *Smart Materials and Structures*, 23(7):075007, may 2014.

[78] Zhongqing Su, Lin Ye, and Ye Lu. Guided lamb waves for identification of damage in composite structures: A review. *Journal of Sound and Vibration*, 295:753–780, 08 2006.

[79] Steffen Tai, Lifu Wang, Leonardo Araque, Ajit Mal, and Christoph Schaal. Effects of homogenization and quasi-isotropy assumptions on guided wave-based nondestructive testing methods. In *Proceedings of the 12th International Workshop on Structural Health Monitoring – IWSHM*, Palo Alto, CA, USA, 2019.

[80] William T. Thomson. Transmission of elastic waves through a stratified solid medium. *Journal of Applied Physics*, 21(2):89–93, 1950.

[81] Thomas Chi-tsai Ting and Thomas Chi-tsai Ting. *Anisotropic elasticity: theory and applications*. Oxford University Press on Demand, 1996.

[82] S. Tiwari and J. Bijwe. Surface treatment of carbon fibers - a review. *Procedia Technology*, 14:505–512, 2014. 2nd International Conference on Innovations in Automation and Mechatronics Engineering, ICIAME 2014.

[83] N. Vasudevan and A. K. Mal. Response of an Elastic Plate to Localized Transient Sources. *Journal of Applied Mechanics*, 52(2):356–362, 06 1985.

[84] Igor Aleksandrovich Viktorov. *Rayleigh and Lamb Waves: Physical Theory and Applications*. New York:Plenum Press, 1967.

[85] Chun-Hui Wang, James Rose, and fu-kuo Chang. A synthetic time-reversal imaging method for structural health monitoring. *Smart Materials and Structures*, 13, 04 2004.

[86] Lei Wang and F.G. Yuan. Group velocity and characteristic wave curves of Lamb waves in composites: modeling and experiments. *Composites Science and Technology*, 67(7-8):1370–1384, 2007.

[87] Lifu Wang. *On lamb waves propagating in honeycomb sandwich structures and thick plates*. PhD thesis, University of California, Los Angeles, Los Angeles, USA, 2022.

[88] Lifu Wang, Fei Gao, Yichi Zhang, Leonardo Araque, Bhav Patel, Steffen Tai, and Ajit Mal. An improved damage index for non-destructive evaluation of a disbond in honeycomb sandwich structure using guided waves. *Journal of Nondestructive Evaluation, Diagnostics and Prognostics of Engineering Systems*, 3:1–14, 03 2020.

[89] Ryan Watkins and Ratneshwar Jha. A modified time reversal method for lamb wave based diagnostics of composite structures. *Mechanical Systems and Signal Processing*, 31:345–354, 08 2012.

[90] R. L. Weaver and Yih-Hsing Pao. Axisymmetric Elastic Waves Excited by a Point Source in a Plate. *Journal of Applied Mechanics*, 49(4):821–836, 12 1982.

[91] P.-C. Xu and A. K. Mal. Calculation of the inplane Green's functions for a layered viscoelastic solid. *Bulletin of the Seismological Society of America*, 77(5):1823–1837, 10 1987.

[92] George Zhao, Tao Qian, Gang Mei, Chiman Kwan, Regan Zane, Christi Walsh, Thurein Paing, and Zoya Popovic. Active health monitoring of an aircraft wing with an embedded piezoelectric sensor/actuator network: Ii. wireless approaches. *Smart Mater. Struct*, 16:1218–1225, 08 2007.

[93] Feng Zhu, Bin Wang, and Zheng-hua Qian. A numerical algorithm to solve multivariate transcendental equation sets in complex domain and its application in wave dispersion curve characterization. *Acta Mechanica*, 230(4):1303–1321, 2019.

[94] J. E. Zimmer and James R. Cost. Determination of the elastic constants of a unidirectional fiber composite using ultrasonic velocity measurements. *The Journal of the Acoustical Society of America*, 47(3B):795–803, 1970.